

AD-A079 328

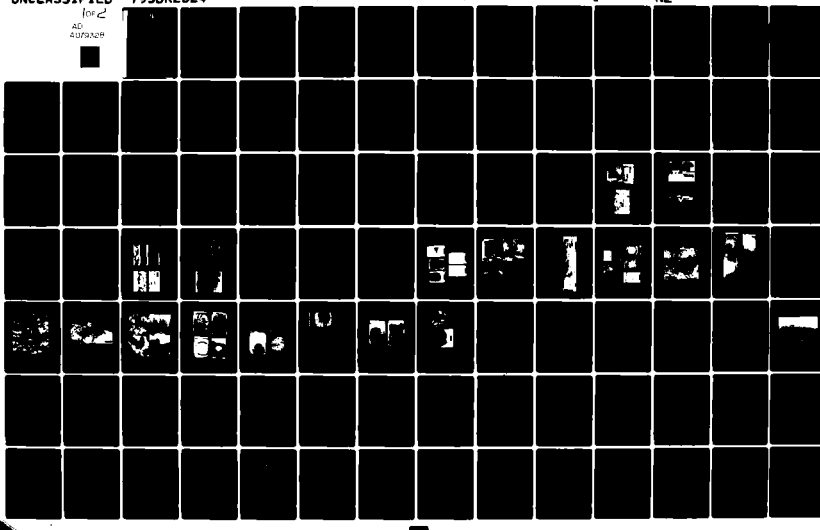
GENERAL ELECTRIC CO PHILADELPHIA PA RE-ENTRY AND ENV--ETC F/G 13/8
PROCESSING RESEARCH ON CHEMICALLY VAPOR DEPOSITED SILICON NITRI--ETC(U)
DEC 79 R A TANZILLI, J J GEBHARDT, J D'ANDREA N00014-78-C-0107

UNCLASSIFIED

for 2
AD
4093208

7950R2324

NL



ADA 079328

LEVEL 12

Document No. 79SDR2324

PROCESSING RESEARCH ON CHEMICALLY
VAPOR DEPOSITED SILICON NITRIDE—
PHASE 2

December 1979

Technical Report

1 February 1978 – 1 October 1979



Prepared under Contract No. N00014-78-C-0107

for the

OFFICE OF NAVAL RESEARCH
800 N. Quincy Street
Arlington, Va. 22217

GENERAL ELECTRIC COMPANY
Re-Entry Systems Division
P. O. Box 8555
Philadelphia, Pa. 19101

This document has been approved
for public release and sale; its
distribution is unlimited.

DDC FILE COPY

→ 404884

9 12 19 071

UNCLASSIFIED

SECURITY CLASSIFICATION OF THIS PAGE (When Data Entered)

REPORT DOCUMENTATION PAGE			READ INSTRUCTIONS BEFORE COMPLETING FORM
1. REPORT NUMBER	2. GOVT ACCESSION NO.	3. RECIPIENT'S CATALOG NUMBER	9
4. TITLE (and Subtitle) PROCESSING RESEARCH ON CHEMICALLY VAPOR DEPOSITED SILICON NITRIDE PHASES		5. TYPE OF REPORT & PERIOD COVERED Technical Report 1 Feb 78-1 Oct 79 ON Phase 2	
7. AUTHOR(s) R.A.Tanzilli, J.J.Gebhardt, J.D'Andrea, C.Dulka, J.Hanson, R.Kretz		14 8. CONTRACT OR GRANT NUMBER(s) N00014-78-C-0107	
9. PERFORMING ORGANIZATION NAME AND ADDRESS GENERAL ELECTRIC CO., RSD P.O. Box 8555 Philadelphia, Pa. 19101		10. PROGRAM ELEMENT, PROJECT, TASK AREA & WORK UNIT NUMBERS NR008-001/10-28-77(471)	
11. CONTROLLING OFFICE NAME AND ADDRESS Office of Naval Research 800 N. Quincy Street Arlington, Va. 22217		12. REPORT DATE 11 December 1979	
14. MONITORING AGENCY NAME & ADDRESS (if different from Controlling Office) Dr. R. C. Pohanka Office of Naval Research 800 N. Quincy Street Arlington, Va. 22217		15. SECURITY CLASS. (of this report) Unclassified	
16. DISTRIBUTION STATEMENT (of this Report) Approved for Public Release; Distribution Unlimited		15a. DECLASSIFICATION/DOWNGRADING SCHEDULE	
17. DISTRIBUTION STATEMENT (of the abstract entered in Block 20, if different from Report)			
18. SUPPLEMENTARY NOTES			
19. KEY WORDS (Continue on reverse side if necessary and identify by block number) Silicon nitride, chemical vapor deposition (CVD), electromagnetic properties, mechanical properties, chemical properties, electrical properties, microstructure and deposition morphology.			
20. ABSTRACT (Continue on reverse side if necessary and identify by block number) Processing research during this contract phase has explored the deposition kinetics of silicon nitride with a variety of furnace designs and silicon:nitrogen precursors including variations in the usual thermodynamic variables of pressure, temperature, flow rate and reactant concentrations. Two specific processes have been identified for forming flat plate and figured geometries in a "hot-wall" reactor. In addition, a set of process conditions have been identified for forming flat plate material of comparable			
			(continued)

DD FORM 1 JAN 73 1473 EDITION OF 1 NOV 68 IS OBSOLETE
S/N 0102-LF-014-6601

UNCLASSIFIED

SECURITY CLASSIFICATION OF THIS PAGE (When Data Entered)

4041 884

UNCLASSIFIED

SECURITY CLASSIFICATION OF THIS PAGE (When Data Entered)

20. ABSTRACT (continued)

physical properties in a "cold-wall" reactor at significantly higher deposition rates ($\sim 2\text{mm hr}^{-1}$).

Physical property characterizations on these deposits performed at various stages of process development continue to reinforce original expectations that the CVD form of silicon nitride possesses many unique properties which could alleviate potential material problems identified by DoD on advanced high-performance missile systems.

Accession For	
NTIS Serial	14
DDC TAB	
Unannounced	
Justification.....	
By _____	
Distribution _____	
Availability _____	
Dist.	Ava. F.
A	

UNCLASSIFIED

SECURITY CLASSIFICATION OF THIS PAGE (When Data Entered)

FOREWORD

This exploratory development program was sponsored by the Office of Naval Research (ONR) under Contract No. N00014-78-C-0107. The report was prepared by the Re-entry Systems Division (RSD) of the General Electric Company, Philadelphia, Pa., and covers research conducted from 1 February 1978 - 1 October 1979. The work was administered under the technical direction of Dr. Robert C. Pohanka of ONR.

The authors acknowledge the experimental support of the following individuals:

CVD Process Development

W. Mueller
R. Rodriguez
J. Yodsnukis

Specimen Preparation

W. Staley
H. Reiss

XRD Analysis

Dr. E. Feingold

Optical Properties

K. Bleiler

Mechanical Properties

F. Rouse

TABLE OF CONTENTS

Section		Page
1.0	INTRODUCTION AND SUMMARY	1-1
2.0	PROCESSING RESEARCH	2-1
2.1	Deposition Studies	2-1
2.2	Reactor Geometry	2-1
2.2.1	Hot Wall Reactors	2-1
2.2.2	Cold Wall Reactor	2-2
2.3	Experimental Data	2-2
2.3.1	HW-1 Runs	2-2
2.3.2	HW-4 Runs	2-4
2.3.3	CW Runs	2-4
2.4	Observations	2-9
2.5	Discussion	2-9
3.0	PHYSICAL PROPERTY CHARACTERIZATION	3-1
3.1	Chemical Properties	3-1
3.1.1	Phase Identification	3-1
3.1.2	Phase Purity	3-1
3.2	Electrical Properties	3-2
3.2.1	Resistivity	3-2
3.3	Electromagnetic Properties	3-2
3.3.1	Visible and Infrared Band Pass	3-2
3.3.2	Microwave Band Pass	3-3
3.4	Mechanical Properties	3-4
3.4.1	Summary	3-4
3.4.2	Mechanical Properties: Hot Wall Reactor (HW-4-200 and - 202)	3-4
3.4.3	Mechanical Properties: Hot Wall Reactor (HW-4-139) . .	3-7
3.4.4	Mechanical Properties: Cold Wall Reactor (CW)	3-7
3.5	Thermal Properties	3-8
3.5.1	Thermal Expansion	3-8
3.5.2	Thermal Diffusivity	3-8
4.0	CONCLUSIONS	4-1
5.0	RECOMMENDATIONS	5-1
6.0	REFERENCES	6-1

TABLE OF CONTENTS (Continued)

Appendix		Page
A	PRECISION LATTICE DETERMINATIONS ON BROWN AND WHITE $\alpha\text{-Si}_3\text{N}_4$	A-1
B	COMPILATION OF FRACTURE TOUGHNESS DATA ON FLEXURE SPECIMENS FROM DEPOSITIONS HW-4-200 AND -202	B-1
C	COMPILATION OF FLEXURE STRESS-STRAIN DATA ON FLEXURE SPECIMENS FROM DEPOSITION HW-4-139	C-1
D	TRIAL MICROETCHING RESULTS ON SELECTED Si_3N_4 SAMPLES	D-1

LIST OF ILLUSTRATIONS

Figure		Page
2-1	Hot Wall Reactors. HW-4 During Deposition at 1500 ⁰ C.	2-22
2-2	Cold Wall Reactor System	2-23
2-3(A)	Typical Flow Conditions in HW-4	2-24
2-3(B)	Flow Conditions in Cold Wall Reactor	2-24
2-4(A)	Deposition Profiles Showing Effect of Temperature on Deposition Rate	2-25
2-4(B)	Deposition Profiles Showing Effect of Pressure on Deposition Rate.	2-25
2-4(C)	Deposition Profiles Showing Effect of Carrier Gas on Deposition Rate	2-26
2-4(D)	Deposition Profiles Showing Effect N:Si Reactant Ratio on Deposition Rate	2-26
2-4(E)	Deposition Profiles Showing Effect of Type of Si-bearing Reactant on Deposition Rate	2-27
2-4(F)	Typical Cross-Sections of Deposits	2-28
2-4(G)	Photomicrographs Showing Transitions	2-29
2-5	Growth Rate vs. Si/N Ratio in HW-1 Runs	2-30
2-6	Schematics of Deposition Geometries	2-31
2-7	Growth Rate vs. Deposition Temperature in Cold Wall Deposition Runs	2-32
2-8	Last Deposited Surfaces of Si ₃ N ₄ Deposited at Various Temperatures	2-33
2-9	Last Deposited Surface of Flexure Bar Cut from Run CW-15	2-34
2-10	Fracture Surface of Flexure Bar 15-1 Cut from Run CW-15	2-35
2-11	Last Deposited Surfaces of Si ₃ N ₄ Deposited at Constant SiCl ₄ /NH ₃	2-36
2-12	Whiskers and Ribbons of Si ₃ N ₄ Deposited with no Diluent	2-37
2-13	Last Deposited Surfaces of Si ₃ N ₄ Deposited at Constant Total Flow	2-38
2-14	Mass Deposition Rate vs. Si/N Ratio	2-39
2-15	Montage of Si ₃ N ₄ Deposited at Si/N Ratio of 7.7	2-40
2-16	Detail Views of Regions Circled in Figure 15	2-41
2-17	Detailed Views of Fine Whiskers Deposited with Helium Dilution and Very Low Ammonia Content	2-42
2-18	Deposits Obtained Using Dichlorosilane - Ammonia Mixtures	2-43
2-19	Deposits Obtained from Trichlorosilane-Ammonia Mixture	2-44
2-20	Deposits Obtained at Constant Si/N Ratio (3.4) and Total Flow	2-45
2-21	Influence of Moving Feed Nozzle Closer to Deposition Substrate	2-46
2-22	Deposits of Intermediates on Substrate at Room Temperature	2-47
2-23	Infrared Spectrum of Intermediates Obtained at Si/N = 0.5 in Nujol.	2-48
2-24	Infrared Spectrum of Intermediates Obtained at Si/N = 0.5 in KCl	2-48
2-25	Infrared Spectrum of Intermediates Obtained at Si/N = 1.0 Nujol	2-49
2-26	Infrared Spectrum of Intermediates Obtained at Si/N = 1.0 in KCl	2-49
2-27	Infrared Spectrum of Intermediates Obtained at Si/N = 2.5 in Nujol.	2-50
2-28	Infrared Spectrum of Intermediates Obtained at Si/N = 2.5 in KCl	2-50

LIST OF ILLUSTRATIONS (Continued)

Figure		Page
2-29	Infrared Spectrum of Intermediate Obtained at Si/N = 1.0 After 48 hours Exposure to Air In Nujol	2-51
2-30	Infrared Spectrum of Residue of DTA/TGA analysis of Si/N = 1 Intermediate. In KC1	2-51
2-31	Typical DTA/TGA Curve of Intermediate Compound	2-52
2-32	Edge Effect on Cold Wall Reactor Substrate	2-53
2-33	Deposition Domains as Function of Initial Pressure for T= 1400K, P = 1 atm	2-54
2-34	Schematic Representation of Effect of Oxygen Impurities on Formation of Amorphous and Crystalline Deposits at Various Temperatures	2-54
3-1	Resistivity of White Silicon Nitride	3-23
3-2	Resistivity of Green Silicon Nitride	3-24
3-3	Resistivity of Brown Silicon Nitride	3-25
3-4	Comparison of Total Spectral Transmittance Function	3-26
3-5	Plot of Experimental and Extrapolated $(\alpha h\nu)^{1/2}$ Values Against $h\nu$ for Determining Eg	3-27
3-6	Infrared Transmittance of Amorphous Si_3N_4	3-28
3-7	Infrared Transmittance of Crystalline $\alpha\text{-Si}_3\text{N}_4$	3-29
3-8	Infrared Transmittance of Crystalline $\alpha\text{-Si}_3\text{N}_4$ as a Function of Temperature	3-30
3-9	Dielectric Properties of CVD $\alpha\text{-Si}_3\text{N}_4$ as a Function of Temperature and Frequency	3-31
3-10	Flexure Stress-Strain Behavior of Several Specimens from Deposition HW-4-200	3-32
3-11	Flexure Stress-Strain Behavior of Several Specimens from Deposition HW-4-202	3-33
3-12	Weibull Plot of Flexure Data from Deposit HW-4-200	3-34
3-13	Weibull Plot of Flexure Data from Deposit HW-4-202	3-35
3-14	Typical Microstructure of CVD $\alpha\text{-Di}_3\text{N}_4$	3-36
3-15	Tension Side and Compression Side of Flexure Specimen HW-4-200-4	3-37
3-16	Tension Side and Compression Side of Flexure Specimen HW-4-200-10	3-38
3-17	Fracture Stress: Grain Size Correlation	3-39
3-18	SEM Fractographs of Flexure Specimen HW-4-202-2	3-40
3-19	Optical-Fractographs of Flexure Specimen HW-4-202-11	3-41
3-20	Optical Fractographs of Flexure Specimen HW-4-202-10	3-42
3-21	SEM Fractographs of Flexure Specimen HW-4-200-4	3-43
3-22	SEM Fractographs of Compression Side of Flexure Specimen HW-4-202-10	3-44
3-23	Flexure Strength as a Function of Color and Temperature	3-45
3-24	Microstructure of Polished and Etched Cross-Sections of Brown Flexure Specimen HW-4-139-B5.	3-46

LIST OF ILLUSTRATIONS (Continued)

Figure		Page
3-25	Microstructure of Polished and Etched Cross-Sections of Green Flexure Specimen HW-4-139-G3	3-47
3-26	Fracture Surface of Brown α - Si_3N_4	3-48
3-27	Fracture Surface of Green α - Si_3N_4	3-49
3-28	Photomicrograph Showing Tensile Stressed Surface of Flexure Specimen CW-19-2	3-50
3-29	Optical Fractograph of Flexure Specimen CW-19-1.	3-51
3-30	Photomicrograph Showing Tensile Stressed Surface of Flexure Specimen CW-30-2	3-52
3-31	Optical Fractograph of Flexure Specimen CW-30-1	3-53
3-32	Optical Fractograph of Flexure Specimen CW-32-2	3-54
3-33	Photomicrograph Showing Tensile Stressed Surface of Flexure Specimen CW-32-1	3-55
3-34	Optical Fractograph of Flexure Specimen CW-44-1.	3-56

LIST OF TABLES

Table		Page
2-1	One-Inch Hot Wall Data	2-15
2-2	Four Inch Hot Wall Deposition Runs	2-16
2-3	Cold Wall Experiments - Temperature Variation	2-17
2-4	Cold Wall Experiments - Gas Flow Rate	2-18
2-5	Cold Wall Experiments - Si/N Variation, Constant Flow	2-19
2-6	Cold Wall Experiments - Precursor Variation	2-20
2-7	Cold Wall Experiments - Mixing Dilution, Location	2-21
3-1	Summary of Crystal Lattice Parameters for α -Si ₃ N ₄ as a Function of Color and Oxygen Content	3-9
3-2	Correlation of Phase Purity of α -Si ₃ N ₄ with Trace Metallic Impurities, Oxygen Content and Degree and Color of Fluorescence	3-10
3-3	Intrinsic Band Gap and Activation Energy as a Function of Deposit Color (and Oxygen Content)	3-11
3-4	Comparison of Band Gap Data Deduced from Optical and Resistivity Measurements as a Function of Color and Oxygen Content	3-12
3-5	Summary of Room Temperature Flexure Strength Data on α -Si ₃ N ₄ Prepared in the Hot-Wall Reactor	3-13
3-6	Summary of Room-Temperature Flexure Strength Data on α -Si ₃ N ₄ Prepared in the Cold-Wall Reactor	3-14
3-7	Flexure Properties of Deposit HW-4-200	3-15
3-8	Flexure Properties of Deposit HW-4-202	3-15
3-9	Fracture Toughness by Indentation for Hot Pressed Si ₃ N ₄ (NC-132)	3-16
3-10	Fracture Toughness by Indentation for CVD α -Si ₃ N ₄ (Spec. No. HW-4-200-4)	3-17
3-11	Correlation of Fracture Toughness with Strength and Grain-Size	3-18
3-12	Flexure Properties of CVD α -Si ₃ N ₄ as a Function of Temperature and Deposit Color (Run No. HW-4-139)	3-19
3-13	Flexure Strength of Selected Monolithic Cold-Wall Reactor Deposits	3-20
3-14	Comparison of Dilatometric Thermal Expansion Behavior of CVD α -Si ₃ N ₄ (This Work) and that Deduced from Temperature-Dependent Lattice Parameter Data (Ref 3-15)	3-21
3-15	Comparison of Thermal Diffusivity (CM ² /SEC) of Reaction Bonded, Hot-Pressed and CVD α -Si ₃ N ₄	3-22

SECTION 1.0
INTRODUCTION AND SUMMARY

SECTION 1.0

INTRODUCTION AND SUMMARY

A need exists for electromagnetic windows which have the following attributes:

- (i) Multiple transmittance band passes and minimal temperature sensitivity of associated properties.
- (ii) Increased thresholds for impact damage and erosion.
- (iii) Improved resistance to the development of thermal stress.
- (iv) Increased refractoriness and strength retention at high temperature.

A material which appears intrinsically to satisfy these property requirements is silicon nitride. During the first and current phase of a planned three-phase ONR program, the feasibility of synthesizing free-standing plate and figured geometries of phase-pure silicon nitride by the chemical vapor deposition (CVD) method has been demonstrated. Physical property measurements on these deposits performed at various stages of process development have continued to reinforce original expectations that the CVD form of Si_3N_4 possesses many unique properties which could alleviate potential material problems on advanced missile systems.

Two processes have been identified which produce near theoretically dense ($> 99\%$) α - Si_3N_4 deposits in a hot wall reactor. Conditions for each of these processes are described in Section 2.0. Similar deposits have also been formed in a cold wall reactor, however, of considerably smaller surface area, but with significantly higher deposition rates ($\sim 2\text{mm/hr}$). Processing studies conducted in the cold wall reactor during the latter phase of the current program indicated that further research focussing upon the role of additives to control the nucleation step could be the key to microstructural control during deposition. The rather surprising result to date is the similarity in microstructures between most depositions in either the hot wall or cold wall reactors, suggesting that the required intervention in the deposition process (to control and vary microstructure) must take place at the nucleation step through the use of selected additives. This will be elaborated upon in Section 2.0.

Property characterizations during this contract period have been broadened in scope including some high temperature measurements of critical mechanical, thermal and electromagnetic properties. Flexure strength data on both hot- and cold-wall reactor deposits yielded three-point moduli of ruptures in the 200 to 300 MPa range. These strength levels are comparable to those currently obtained on reaction-sintered Si_3N_4 . Elevated temperature measurements on CVD α - Si_3N_4 show only a slight decrease with temperature up to 1400°C in contrast to the rapid decrease in strength of hot-pressed modifications which utilize densification additives to achieve consolidation. For example, at 1400°C , CVD α - Si_3N_4 deposits retain 76 percent of their room temperature strength compared to only 33 percent for hot-pressed Si_3N_4 .

Microstructural investigations of flexure specimens uncovered a grain size:strength correlation following the classical Hall-Petch relationship over a grain size range of 16 to 34 microns. Extrapolation of this data to smaller grain sizes typical of hot pressed modifications (1-2 microns) indicated that a strength potential of 1110 MPa may be achievable if grain size reduction can be achieved through control of the nucleation and grain growth kinetics during deposition. Fracture toughness measurements fall between reaction-sintered and hot pressed Si_3N_4 ; however, the Vickers hardness levels of CVD α - Si_3N_4 are significantly greater than either commercial modification. Fracture mechanics analyses of mechanical property data identified a critical flaw size responsible for failure of about 39 microns which was found to correlate with observed microcrack networks in the deposit volume. Elimination or reduction in the size of these defects would lead to significant strength improvements. Fractographic examination of flexure specimens indicate cleavage as the dominant fracture mode with a minor fraction possibly attributable to grain boundary decohesion. The dominant fracture path is transgranular with additional areas showing features attributable to imperfections (microcracks) and changes in crystal orientation.

Electromagnetic property data continue to reinforce expectations for a high performance multimode window. Invariancy with temperature of electromagnetic energy transmittance in the infrared and microwave band passes, is a major attribute of CVD α - Si_3N_4 . The issue of imaging potential in the visible-infrared band pass remains and will be addressed more comprehensively during the next contract phase. Window applications, however, have been identified where the diffuse nature of its current transmittance function is not a disadvantage.

Electrical property measurements indicate that CVD α - Si_3N_4 is an excellent high-temperature insulator. Electronic band gap measurements range from 4 to 5 electron volts and appear to correlate with color of deposit. It has also been discovered that CVD α - Si_3N_4 exhibits fluorescence whose intensity and spectrum correlates with color of the deposit. Neutron activation analyses of such deposits show a correlation of color with oxygen content: being least with dark brown deposits and greatest with water clear. Conversely, amorphous deposits do not fluoresce and contain the highest oxygen impurity level. X-ray diffraction analyses of brown and water clear deposits indicate lattice shrinking with increased oxygen impurity level suggesting a finite solubility of atomic oxygen in the α - Si_3N_4 lattice by a substitution or interstitial mechanism.

The remaining sections of this report will describe in detail the status of processing research and physical property characterizations at the conclusion of this reporting period.

**SECTION 2.0
PROCESSING RESEARCH**

SECTION 2.0

PROCESSING RESEARCH

2.1 DEPOSITION STUDIES

The formation of silicon nitride from the vapor phase was studied under a variety of conditions, using different silicon-containing precursors and reactor geometries, to determine the influence of deposition parameters on crystallite size, morphology and deposition rate. Geometries include a cold-wall, flat plate reactor (CW) and 4-inch and 1-inch diameter hot wall furnaces (HW-4) and HW-1), respectively. Parametric variations included:

Temperature: 1425-1500°C (HW-1 and CW),
RT (CW), 1400-1480°C (HW-4)

Pressure: 1-15 torr (HW-1 and HW-4)
40 torr (CW)

Flow Rate: 1100-3600 cc/min (HW-4)
178-1830 cc/min (CW)
1100-1200 cc/min (HW-1)

Silicon/Nitrogen Feed Ratio: 0.65-1.9 (HW-1)
0.23-1.9 (HW-4)
0.66-13.6 (CW)

Precursors: SiCl₄, HSiCl₃, H₂SiCl₂ (CW)
SiCl₄, SiF₄ (HW-1, HW-4)

Other: With, without H₂ (HW-1, HW-4)
Helium Diluent (CW)

2.2 REACTOR GEOMETRY

2.2.1 Hot Wall Reactors (HW-1, HW-4)

These consist of vertical, tubular, resistant-heated graphite furnaces in which the feed gases are mixed in the bottom of the deposition zone and pumped past the heated graphite surfaces on which deposition occurs. In HW-1 a 1.27 cm² x 20 cm long graphite channel comprised the deposition surface, while in HW-4, because of its larger diameter, both square and hexagonal boxes, containing one and two flat, vertical, or flat horizontal plates could be

used. A dome shaped internal mandrel was also used. The reactor systems are equipped with mass- and volume flowmeters for metering the reaction gases and appropriate traps and pumping equipment.

The substrates were made of ATJ graphite which could be burned away to obtain free deposits. In HW-1, a Grafoil[®] liner was used on the 1.27 cm x 1.27 cm channel which enabled it to be reused in some cases.

Figure 2-1 shows the HW-1 and HW-4 reactors.

2.2.2 Cold Wall Reactor (CW)

The cold wall reactor was designed after that of Niihara and Hirai (Ref. 2-1) with certain modifications. An additional viewport was added to permit visual observation of the flow patterns at the deposition surface during formation of the deposit. A retractor assembly was also constructed which permitted the graphite deposition surface to be stretched flat again after it had bowed because of thermal expansion on heating. Figure 2-2 shows the cold wall reactor as well as the electrode assembly.

Residence time of the gas mixture in the hot zone as well as its velocity are determined by the internal geometry of the deposition furnace, as well as by the experimental temperature and pressure. Figure 2-3 illustrates this for HW-4 and CW under a typical set of conditions, assuming no volume change as a result of the reaction, which will be discussed separately.

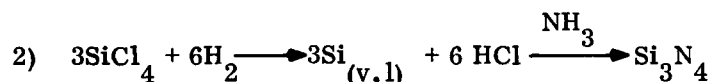
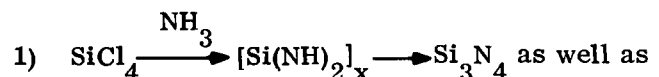
2.3 EXPERIMENTAL DATA

In most of the experiments, the Si/NH₃ ratio was kept on the high side for two reasons — to minimize formation of Si-N polymeric species which form through gas phase collision and to reduce corrosion of the graphite components by ammonia. In the former, it was expected that grain size might thereby be kept smaller. Corrosion of the graphite was noticeably reduced in the CW experiments, although it is believed that ratios of Si/N somewhat less than 1 could be tolerated.

2.3.1 HW-1 Runs

Table 2-1 summarizes the data regarding experiments in HW-1. Most of these deposits appeared to be mixed, i. e., consisting of both amorphous and crystalline material, except

where the Si/N ratio and or pressure was low (~ 1.1 - 1.2). The deposits showed a typical CVD deposition pattern, reflecting a short period of heating and initiation of deposition species at the inlet of the deposition zone, prior to development of maximum thickness. Figures 2-4(A) thru 2-4(E) summarize deposition profiles obtained in this series of runs. Figures 2-4(F) and 2-4(G) show typical crosssections of banded deposits and deposits which showed transitions from amorphous to crystalline morphologies, respectively. Figure 2-5 relates maximum deposit thickness (mm/hr) to the Si/NH₃ ratio and shows that at high Si/NH₃ ratios, growth rates are high (and densities low since these were largely amorphous deposits), with the exception of run HW-1-74 in which no hydrogen was included beyond what was generated by the dissociation of ammonia. Here, deposition rate of a crystalline deposit was substantially the same as for low ratios of Si/NH₃ (HW-1-63, 65) where hydrogen was added. This will be discussed again later, but it opens the question of the existence of more than one deposition sequence, i.e.,



Pressure may play a part in shifting the deposition sequence from reaction (1) to reaction (2) since residence times become longer, and the number of collisions greater. Thus, at the high H₂/SiCl₄ ratios used, more of the Si₃N₄ produced could result from nitriding of Si in the gas phase rather than formation from ammoniated silicon intermediates. At 15 torr (Run HW-1-69) for example, the deposit was powdery, indicating a high degree of gas phase nucleation. However, there does not appear to be elemental silicon present to a significant extent in the deposit, since the growth rate appeared to be limited by the amount of nitrogen available and since conversion of both silicon and nitrogen was always in the anticipated 4/3 ratio, even at high Si/NH₃ ratios.

As has been experienced in studies on this program, and others the use of SiF₄ in the place of SiCl₄ led to a significantly reduced growth rate and deposit weight. This is not unexpected in view of the much greater stability of the fluorinated silicon compounds SiF₄ and SiF₂.

2.3.2 HW-4 Runs

Depositions in HW-4 were carried out over a longer period of time, primarily to obtain material for characterization. Deposition rates can be expected to be lower since the ratio of total material fed to available deposition area is also much lower. Table 2-2 lists the data as well as the geometries used. The latter are illustrated in Figure 2-6.

It is again clear in these runs that the deposition rate in the fluoride system is far lower than in the chloride. It is also observable that total feed rates similar to those used in HW-1 runs, led to crystalline rather than amorphous deposits, even at relatively high Si/NH₃ ratios, (e.g., 1.37). At high ratios, banding and mixed deposits were obtained. In Run HW-4-81, (from the earlier study, Ref. 3-1) in which a dome was fabricated, the low Si/NH₃ ratio (0.23) led to large grained crystals which built up to leave a very knobby surface on which it was difficult to measure a thickness. However, the deposit was dark and entirely crystalline as has come to be expected under these circumstances.

An oxygen containing additive, nitrous oxide (N₂O), was used in Run HW-4-149 in an effort to modify grain size. The result was a mixed amorphous/crystalline deposit, with the former predominating in the lower or entry region of the deposition zone.

Properties and characteristics of these deposits are discussed in Section 3.0 of this report.

2.3.3 CW Runs

Experiments were planned in the cold wall reactor to examine certain features of the deposition process which are not readily approached in hot wall reactors. These include:

a) Si/NH₃ ratio; b) Si/NH₃ concentrations at equivalent total feed rates; c) temperature under otherwise identical conditions; d) total gas velocity variation; and e) the use of less than fully chlorinated silanes as precursors. Other experiments included deposition of reactive intermediate species at room temperature for subsequent characterization and the effects of mixing and distance of the gas inlet from the deposition plate. Specimens were taken from various deposits for strength measurement and characterization.

2.3.3.1 Temperature Variation

Table 2-3 lists the conditions used and data obtained on material deposited at various temperatures; Figure 2-7 shows the variation in growth rate with temperature. The data

are too few to correlate with reciprocal temperature for computing an accurate activation energy — however an estimate in the vicinity 50 Kcal/mole up to 1450°C, is in general agreement with results obtained by Niihara and Hirai (Ref. 2-2).

As shown in Table 2-3 and described in Section 3.0, modulus of rupture values were low for banded deposits made at lower temperatures, while deposits prepared at higher temperatures had near theoretical densities and MOR values equivalent to materials made in hot wall reactors.

Figure 2-8 shows surfaces of the deposits prepared in this series of experiments. Note the disappearance of vitreous material as temperature is increased above 1450°C. Cross sections of Runs CW 14-16 showed considerable banding.

Figures 2-9 and 2-10 are SEM views of the last deposited surface and fracture surface of a flexure bar cut from Run CW-15 ($T_{DEP} = 1425^{\circ}\text{C}$). Figure 2-9 shows the fracture edge (tensile side) and the break traversing some of the major conical features, while in Figure 2-10, several bands can be seen, within which are numerous vertical cracks.

2.3.3.2 Flow Variation

Experiments were conducted in which the Si/NH₃ ratio was kept constant and the total flow varied by using helium as an additional carrier. Table 2-4 lists the experimental conditions and observations, while Figure 2-11 shows the deposit surfaces. From the appearance of the deposits, it is clear that as the reagents became more dilute, and the time of transit through the hot zone shorter, the deposition process became increasingly dominated by the nucleation step. The appearance of whiskers as shown in Figure 2-12 and very fine grain material in the first deposited layer predominated in all cases except where the gas flow was so slow that buoyancy forces dominated and very little of the gas reached the substrate. The use of a lower flow rate (Run 43), with no dilution produced the finest grain deposit — all runs which were more highly diluted, or fed at higher velocity led to whisker growth. Run CW-43 does suggest that a more precise balance of flow rate, stoichiometry and dilution could produce a fine grained deposit in the current reactor. Since this balance depends to a great extent on the reactor geometry and balancing of buoyancy and gravitational forces, it does not seem likely that it could be translated directly to another geometry. It does

indicate however, that grain size alteration can be achieved in this manner, and that a proper balance for a given reactor could lead to a stronger, finer grain deposit.

2.3.3.3 Si/NH₃ Ratio Variation

Table 2-5 and Figure 2-13 show respectively, the experimental conditions and deposits obtained in a series of runs in which the Si/NH₃ ratio was increased to reduce the number of polymerization conditions occurring prior to deposition. Runs CW-35 and CW-36 yielded high density crystalline material while increases in the Si/NH₃ ratio above 2.64 led to formation of an increasing number of granular and whisker containing deposits, reflecting control of the deposition process through nucleation.

As could be anticipated, the mass deposited was inversely proportional to the Si/NH₃ ratio as shown in Figure 2-14. The significant effect of reactor geometry is clear in comparing these results to those obtained in both HW-1 and HW-4, where Si/NH₃ ratios above about 1.5 led to amorphous or banded deposits.

Figure 2-15 is a SEM montage showing a variety of growth habits, varying from large nodules containing crystalline relatively fine grain material as well as amorphous appearing structures to large hexagonal pillars which appear to be single crystals. The spherical appearance of most of the nodules suggests a liquid or semiliquid phase which may result from rapid reduction of SiCl₄ in the hydrogen-rich gas medium and rapid nitridation because of high diffusion rates in the fluid phase. Other areas show large crystals that may have nucleated at the surface and continued to grow largely from the vapor phase on specific growth planes.

Figure 2-16 shows details of regions circled in Figure 2-15 at a higher magnification. In particular, the left view contains web-like structures at intersections of various crystal faces, suggestive of an intermediate that lost considerable volume through decomposition after striking its final resting place. The right view also shows features which suggest a soft or liquid period prior to solidification.

At very low ammonia content and with helium dilution, formation of very fine whiskers ("sea urchins") predominated, suggesting that formation was primarily from the vapor phase with little of the nodular growths seen at only slightly greater ammonia content (Run 38 vs. Run 37). Figure 2-17 shows detail views of these whisker growths.

2.3.3.4 Precursor Variation

Table 2-6 and Figures 2-18 and 2-19 show the results of experiments performed using less fully chlorinated silane precursors, i. e., HSiCl_3 and H_2SiCl_2 instead of SiCl_4 . Dichlorosilane led to considerable gas phase nucleation at 1475°C and 1400°C , as shown in Figure 2-18, reflecting the low thermal stability of that species. At 1100°C , the deposit was smooth and fine grained, but consisted mostly of elemental silicon. Trichlorosilane yielded a striated laminar deposit of slightly less than theoretical density and about half the strength of the better deposits obtained with tetrachlorosilane (i. e. SiCl_4). The smoother, finer structure shown in Figure 2-19 (CW-44) suggests that a lesser degree of polymerization may have occurred, and that after identification of more appropriate stoichiometric ratios, temperature and concentration, better control of grain structure could be achieved.

2.3.3.5 Dilution — Traverse Time

Figures 2-20 and 2-21 and Table 2-7 show the results of experiments designed to evaluate the effect of reducing gas phase reactions, i. e., polymerization of imide intermediates. As in the experiments with increasing gas velocity, reduction of concentration led to increased whisker formation as shown in Runs CW-32-34 (Figure 2-20), under the same conditions of temperature, pressure and flow rate.

With movement of the gas inlet nozzle from 3 cm to 5 cm above the deposition surface (see Figure 2-3) the nature of the deposit changed considerably (as is seen in Figure 2-21). At 5 cm the deposit was considerably more crystalline than at 3 cm (Runs CW-30, CW-31). As can be seen from Figure 2-3, such a move increases slightly the traverse time from inlet nozzle to deposition plate, and owing to the wider area included in the deposition zone, reduces gas velocity slightly. Although movement of the nozzle by only two centimeters appears to be a very small change, its effect on concentration, gas velocity and residence time in the hot boundary layer is evidently significant. In both runs, the gases were mixed by placing a small piece of platinum foil inside the inner nozzle to force the ammonia into the silicon tetrachloride stream at the nozzle.

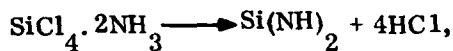
2.3.3.6 Room Temperature Deposits

In order to obtain specimens of the intermediate compounds that form on mixing silicon tetrachloride and ammonia vapors, the cold wall reactor was operated briefly with no power

to the deposition substrate. The white powdery deposits that formed at three Si/N ratios (0.5, 1 and 2.5) were collected, still attached to the substrates and protected from hydrolysis by storage in a sealed container containing anhydrous calcium sulfate (Drierite). Figure 2-22 shows deposits typical of Si/N ratios of 2.5 and 1. Note the similarity to vitreous Si_3N_4 deposits in the appearance of rounded protuberances on the surface, and in the case of the higher ammonia content, an almost glassy appearance. After exposure to laboratory air for two days, there appeared to be a cracked, glassy layer over the deposit made at the higher ammonia level.

Specimens of the deposits were used to obtain infrared spectra, using both the Nujol (mineral oil) mull and potassium chloride pellet techniques. These are shown in Figures 2-23 through 2-30. Specimens were also used to obtain DTA/TGA curves up to $1000\text{-}1100^\circ\text{C}$, a typical one of which is shown in Figure 2-31. All three Si/N ratios gave identical results with respect to appearance of the endotherm and the percent weight loss. Interpretation of the spectra is rendered somewhat difficult owing to the extreme reactivity of the intermediates toward moisture and the probability that they all contain absorbed ammonium chloride and ammonia. A strong ammoniacal odor indicates that hydrolysis was probably occurring during handling, and more rigorous techniques will have to be developed for future studies.

The TGA/DTA curves (Fig. 2-31) for all of the Si/NH₃ ratios used were identical with respect to the location of the endotherm ($\sim 350^\circ\text{C}$) and percent weight loss (73-73.5%). While it may be coincidental, it is interesting to note that in the reaction:



evolution of HCl accounts for a weight loss of 71.6%.

The spectra of the intermediates in Nujol (Fig. 2-23, 25, 27) and KCl (Fig. 2-24, 26, 28) are similar since they are qualitative it is difficult to compare peak heights. However, most of the peaks relate to NH₄ (1400 cm^{-1}) and NH₃ (3400 cm^{-1}) groups, with a small peak in one case at (869.6 cm^{-1}) that has been related to the Si-N stretching frequency (Ref. 2-4). This is not present in all the specimens, probably due to hydrolysis on handling. It was also missing from the spectrum of a specimen allowed to stand in air for two days before examination (Fig. 2-29). Similarly, the residue from the TGA/DTA experiment (Fig. 2-31)

shows a broad band in Figure 2-30 between 1050 and 1150 cm^{-1} which is probably the Si-O band, although a minor absorption peak remains at 800 cm^{-1} indicating that some amorphous Si_3N_4 may have been produced.

Heat treatment of the intermediate immediately after its deposition on the cold substrate was not successful. The large volume of gas released caused the deposit to flake and curl, losing contact with the substrate.

2.4 OBSERVATIONS

Installation of the additional viewing port at a 45-degree angle to the deposition surface enabled direct observations to be made of the cloud of particles present at the plate. In certain instances it appeared that periodic pulsation was taking place while in other runs there was random motion within the particle cloud. This turbulence could be responsible for the banded appearance of some deposits although no correlations have been possible as yet.

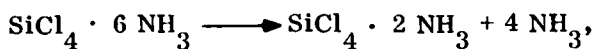
A second observation, which is also related to gas flow concerns material deposited on the edge of the plate, as shown in Figure 2-32. In nearly all cases where a dense, crystalline, coherent deposit formed on the upper surface of the plate, a dividing line occurred on the edge, indicative of a flow separation phenomenon. The deposit formed below the dividing line was usually black, nodular and crystalline. As yet grain sizes for this type of material have not been measured.

On the back side of the plate the deposits have usually been very thin and whisker-like, as would be expected from the low mass flow rate there as well as a low ammonia level. The whiskers, needles, etc. were often dark red and white. In a few instances, elemental silicon was found. This resulted probably from decomposition of the imide complex molecule in the absence of nitrogen or ammonia. This had been found to occur in earlier studies when recovered white intermediate material was heated to convert it to the stable nitride. In the cold wall reactor, ammonium chloride, formed in the gas phase on decomposition of the intermediates, settles out, in contrast to the situation in the hot wall furnace where it can dissociate and remain available for further reaction.

2.5 DISCUSSION

The basic chemical reactions proposed to account for formation of silicon nitride from silicon tetrachloride and ammonia have been elucidated by Billy (Ref. 2-5) as well as Gelmers

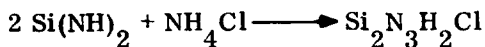
and Naumann (Ref. 2-6). The over all pattern is one of complex formation at low temperature:



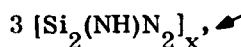
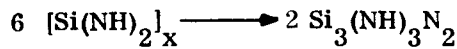
followed by deammination chlorine elimination and establishment of silicon nitrogen bonds:



This is followed by reaction of the intermediate to form chlorine containing intermediates:



according to Billy, or formation of polymeric species:



according to Glemser and Naumann. In both reaction sequences, higher polymeric species have been postulated, with establishment of a three dimensional network of SiN tetrahedra. Presumably, deposition of $\alpha - \text{Si}_3\text{N}_4$ can result from any of these species, and it seems logical that the larger the polymers, the larger the deposited grains.

A number of reaction mechanisms can be proposed, which reduce to deammination on striking the substrate. The possibility of the polymeric species dissociating to Si + NH₃ followed by nitriding has not been suggested, but the great instability and great variety of potential species suggests that some may undergo such a reaction.

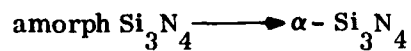
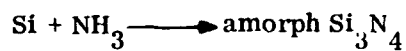
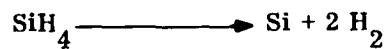
The variety of growth habits occurring in a single deposit (Figure 2-15) suggests that competing processes occur. One, for example, may generate intermediate species of a sufficiently low molecular weight and order to constitute a liquid or semi-liquid phase that results in a globular deposit that can be crystalline or amorphous depending on such factors as temperature, ammonia, partial pressure, particle size and time for crystallization before being trapped by succeeding material. At very low ammonia levels or with inert gas dilution, on the other hand, growth from the vapor phase can predominate with

formation of whiskers. This may depend on attachment of species of less than unit cell size, containing both nitrogen and silicon, or deposition of silicon and immediate ammoniation. These processes would be sensitive to stoichiometry concentration and time, with vapor-liquid-solid (V-L-S) processes favored by high ammonia/silicon ratios, high concentrations and long times. Whisker formation would be favored by the opposite conditions.

Most of the studies carried out have not discussed possible, high temperature competing reactions, particularly in the presence of excess hydrogen, for example,



Both of these can occur during deposition and are probably responsible for the higher deposition rates observed when hydrogen is used as the carrier. Neither strength nor grain size of the material produced with and without hydrogen appears to be different, although crystalline deposits are less difficult to obtain in the absence of hydrogen. Thermodynamic studies by Mellottee and Cochet (Ref 2-7) indicate that the use of argon and hydrogen as a carrier gas in the system Si-N-H leads to deposition domains in which Si_3N_4 and Si are codeposited. Use of nitrogen as the carrier requires considerably higher silane pressures for this to occur, as shown in Figure 2-33. Earlier studies in this program have shown that, with extreme care to prevent premature gas phase decomposition, silane-ammonia mixtures lead to fine-grained crystalline Si_3N_4 . No intermediate complex formation appears to be involved, and indeed, it has been shown that most of the silane is decomposed prior to striking the deposition surface (Ref. 2-8). Formation of vitreous Si_3N_4 from silane-ammonia may thus be the result of an imbalance between the rate of nitride formation and the rate of crystal growth or crystallization.



This sequence can be contrasted with that of the complex intermediate sequence in which some tetrahedral bonding has already occurred prior to deposition.

Further studies should be done on the influence of hydrogen content or partial pressure on both deposition rate and grain size, since it is by no means certain that hydrogen is simply a carrier in this reaction.

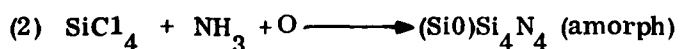
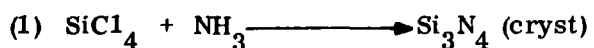
In addition to the influence of hydrogen as reagent/carrier, there is a definite indication that another possible competing reaction is occurring, which results in formation of Si-O bonds.

In most of the CVD Si_3N_4 work reported on this program and elsewhere (Refs. 2-1, 2), it is clear that the color of the deposit and its oxygen content are related. It is not clear why the addition of oxygen results in deposition of amorphous Si_3N_4 instead of crystalline, other parameters being the same. In related work in this laboratory, it has been found possible to add a limited amount of oxygen in the ppm range and thereby achieve a white, crystalline, relatively fine grain deposit, which appears to fall close to the amorphous/crystalline line drawn by Niihara and Hirai (Ref. 2-9). It is quite possible that the amorphous/crystalline boundary is located with respect to a given temperature and pressure only because the deposition system has a constant residual oxygen or water background. An increase in the background would result in deposition of amorphous material at a somewhat higher temperature.

Since the required oxygen level is low, variations can be anticipated until control is re-established which may not be simple because of the ubiquitous nature of oxygen sources.

Kijima (Ref. 2-10), Lin (Ref. 2-11), Lindley et al (Ref. 2-12) and Messier et al (Ref. 2-13) associated the presence of small quantities of O impurities with significant effects in formation of single crystals of Si_3N_4 from the vapor phase, and the rate of nitriding silicon powder. Mitomo and co-workers (Ref. 2-14) go further and postulate that thermodynamically, the incorporation of O in Si_3N_4 is inevitable. The conclusion has also been reached that the presence of O enhances $\alpha\text{-Si}_3\text{N}_4$ formation, while metallic impurities (e.g. Fe) favor $\beta\text{-Si}_3\text{N}_4$.

Since the use of high NH_3/Si ratios has been found to yield crystalline material more reliably, the importance of stray oxygen in the deposition system may be related to the kinetics, and therefore mass action of two competing reactions:



This can be represented schematically as shown in Figure 2-34.

Since both additives can be incorporated into the gas feed, it seems that the role of such impurities must be clarified if a reliable understanding of the CVD process is to be gained. For example, in a recent Si_3N_4 deposition run on a related program in this laboratory, a positive identification of $\beta\text{-Si}_3\text{N}_4$ was obtained, for the first time in a CVD process.

Some of the results presented earlier can be interpreted in the light of the foregoing discussion, although lack of resolution of the roles of hydrogen and oxygen in the process renders the interpretation speculative.

Formation of amorphous versus crystalline materials: a) as temperature is reduced or b) as the gas inlet is moved closer to the substrate, can be interpreted to mean that the influence of O impurities is felt more at low rather than high deposition temperatures and at short rather than long residence times. The latter point is more debatable, and comparisons of runs in HW-1, HW-4 and CW are not possible in the absence of information regarding the O background of these reactors. However, the former point is somewhat better established since, with deliberate additions of O, amorphous material has been deposited at temperatures as high as 1500°C in related work in this laboratory.

Reduction of concentration of intermediate species by limiting NH_3 by diluting the gas or by increasing velocity led to whisker formation rather than finer grain material, suggesting that a change in nucleation mechanism rather than gas phase composition is necessary. This may be able to be approached by the use of additives known to influence nitridation of silicon, such as iron.

Experiments involving both the fluoride system and the chloride system with low hydrogen content led to low deposition rates, without significant change in crystallite habit. Similarly the widely different geometric and flow conditions of HW-1, HW-4 and CW produced similar deposits, again suggesting that the required intervention in the deposition process must take place at the nucleation step through the use of selected additives.

Results of experiments involving precursors other than tetrachlorosilane showed that the trichloro compound may have some merit in that the early phases of the interaction (i.e., producing $\text{SiCl}_4 \cdot 2\text{NH}_3$) may not occur. However, if most of the action results from reactions involving SiCl_2 , there may be little difference. The only significantly different microstructure observed in this work resulted from a run using HSiCl_3 and this alone would merit

further study. The dichlorosilane reacted more like silane in that gas phase decomposition resulted in sooting reactions. Both reagents however may be useful as additives to tetrachlorosilane to generate a mixture of species.

TABLE 2-1. ONE-INCH HOT WALL DATA

RUN NO.	FLOW RATE (ccm)			T °C	P (torr)	DEP. WT. (gms)	Si/NH ₃	MORPH.
	SiCl ₄	NH ₃	H ₂					
HW-1-63	92.4	77	950	1115	1450	1-4	10.8	.215
HW-1-64	108	"	"	1131	"	2-2.5	8.1	.165
HW-1-65	87.7	"	"	1110	"	1-2.5	12.1	.17
HW-1-66	131.2	"	"	1154	"	1.3	17.4	.24
HW-1-67	133.2	"	"	1156	"	1.9	21.6	.31
HW-1-68	146	"	"	1169	"	5	26.2	.43
HW-1-69	140	"	"	1163	1460	15	25.4	.61
HW-1-70	124	"	"	1152	1475	5	27.3	.52
HW-1-71	124	"	"	1152	1425	"	24.7	.38
HW-1-72	113	"	"	1140	1450-	"	19.0	.30
					1500			
HW-1-73	147.5	"	"	1175	1500	"	33.8	.62
*HW-1-74	144	"	900	1121	1450	"	13.2	.25
HW-1-75	158	150	900	1208	"	"	39.8	.68
HW-1-76	98 _F	150	950	1198	"	"	6.7	.09

*N₂ instead of H₂

TABLE 2-2. FOUR INCH HOT WALL DEPOSITION RUNS

Run No.	*Geom. (Halide)	(Additive)			Flow Rate (ccm)			Si:NH ₃ Ratio	T (°C)	P (torr)	Dep. Rate (mm hr ⁻¹)	Morphology
		SiX ₄	NH ₃	H ₂	Total							
HW-4-81	C1	678	2914	-	3592	0.23	1475	8-10	0.53	Cryst., Brown (B)		
HW-4-128	C1	317	450	2650	3437	0.67	1480	5	0.32	Cryst., Brown (B)		
HW-4-129	F	480	350	500	1330	1.37	1400	10	0.07	Cryst., White (W)		
HW-4-139	C1	480	350	"	1330	1.37	1400	10-14	0.05	Cryst., B,G,W		
HW-4-149	C1	598	350	"	1453	1.71	1420	5	0.41	Cryst., B,G,W		
HW-4-165	C1	657	350	"	1507	1.88	1440	4	0.19	Banded, (B,G,W)		
HW-4-166		588	350	"	1438	1.68	1430	4.5	0.38	Banded, (B,G,W)		
HW-4-200	F	204	480	"	1184	0.43	1425-	10-16	0.12	Cryst., Brown (B)		
HW-4-202	F	347	480	"	1327	0.72	1425-	12-14	0.12	Cryst., Brown (B)		

*See Figure 2-6

TABLE 2-3. COLD WALL EXPERIMENTS - TEMPERATURE VARIATION

CONDITIONS:

SiCl ₄	=	230 cc/min
NH ₃	=	68 cc/min
H ₂	=	700 cc/min
Total	=	998 cc/min
P	=	40 torr
Si/NH ₃	=	3.4

RUN NO.	T (°C)	DEPOST. RATE (mm/hr)	DEPOST. RATE (gm/hr)	FLEX. STRENGTH MPa	FLEX. STRENGTH (kpsi)	DENSITY (g/cm ³)	MORPH
CW-14	1400	1.07	2.32	21.10 10.07	(3.08) (1.46)	-	Banded
CW-15	1425	1.32	1.94	18.62 28.27	(2.70) (4.10)	-	Banded
CW-16	1450	1.67	2.25	219.74	(31.87)	3.08	Columnar, Brown
CW-18	1475	n.m.	2.21	-	-	-	-
CW-19	1500	1.98	2.54	238.97 229.11	(34.66) (33.23)	3.21 3.120	Columnar, Brown

TABLE 2-4. COLD WALL EXPERIMENTS - GAS FLOW RATE

T = 1475°C
 P = 40 torr
 Ratio = Si/NH₃ = 3.42
 SiCl₄ = 82 cc/min
 NH₃ = 24 cc/min
 He = Variable
 H₂ = 350 cc/min

RUN	FLOW RATE (ccm)		DEP. RATE gm/hr	MORPH.
	He	TOTAL		
CW-39	-	356	-	Fine red needles (Si° back)
CW-43	500	856	-	Very fine cryst.
CW-40	1000	1356	.501	Needles, single crystals.
CW-41	1500	1856	.101	Fine whisk., fuzz
CW-42*	125	178	0	No Deposit

TABLE 2-5. COLD WALL EXPERIMENTS - Si/N VARIATION, CONSTANT FLOW

Temp. = 1475°C
 Press. = 40 Torr
 Tot. Flow = 984 cc/min

RUN	FLOW RATE (cc/m)			Si/NH ₃	DEP. RATE (gm/hr)	FLEX. STRENGTH MPa (kpsi)	DENSITY (g/cc)
	SiCl ₄	NH ₃	H ₂				
CW-35	177	267	540	-	0.66	2.741 230.42 296.20	(33.42) (42.90)
CW-36	177	67	540	200	2.64	1.965 193.88 254.00	(3.12) (3.15)
CW-37	177	23	540	234	7.70	1.150	-
CW-38	177	13	540	254	13.6	0.521	-

TABLE 2-6. COLD WALL EXPERIMENTS - PRECURSOR VARIATION

Precursors: SiCl_4 vs HSiCl_3 , H_2SiCl_2

T = 1475°C (Run CW-49, T = 1100°C, Run CW-48, T = 1400°C)
 $P = 40$ Torr

Precursor	Run No.	Flow Rate (ccm)			Si	Dep. Rate	Flex. STR.	Density	Morph.
		SiH ₃	NH ₃	H ₂	Total	Si/N	gm/hr	MPa (Kpsi)	(g/cc)
SiCl ₄	CW-32	230	68	700	-	998	3.38	2.380 (4.25) 29.30 (5.35)	- Bands
HSiCl ₃	CW-44	260	68	303	400	1031	3.85	2.141 (16.14) 107.49 (15.59)	3.12 Straited Laminar
SiCl ₄	CW-36	177	68	540	200	984	2.64	1.965 (28.12) 254.00 (36.84)	3.14 Dark Cryst.
HSiCl ₃	CW-45	260	34	303	442	1038	7.65	3.208 -	- Nod. whisk.
H ₂ SiCl ₂	CW-46	333	68	700	-	994	4.9	8.072 -	- Soot whisk.
H ₂ SiCl ₂	CW-47	215	230	534	-	994	0.99	8.44 -	- Sooty
H ₂ SiCl ₂	CW-48	277	267	550	-	1094	1.04	7.54 -	- Sooty
H ₂ SiCl ₂	CW-49	326	230	534	-	1040	1.4	-	- Fine gr. SiO

TABLE 2-7. COLD WALL EXPERIMENTS -MIXING DILUTION, LOCATION

A. FEED LOCATION, MIXING

SiCl_4	= 230 cc/min	Si/N	= 3.38
NH_3	= 68 cc/min	T	= 1475°C
H_2	= 700 cc/min	P	= 40 Torr

1. 5 cm Nozzle - Plate + Mixing

	<u>DEP. RATE</u> g/hr	<u>FLEX. STR.</u> MPa	(kpsi)	<u>DENSITY</u> (g/cc)	<u>THICK.</u> (mm)	<u>MORPH</u>
CW-30	1.891	267.24	(38.76)	3.16	1.04	Cryst.
		254.49	(36.91)	3.19	1.09	Dark, con.

2. 3 cm Nozzle - Plate + Mixing

CW-31	2.645	27.03	(3.92)	1.17	Banded, vitr.
-------	-------	-------	--------	------	---------------

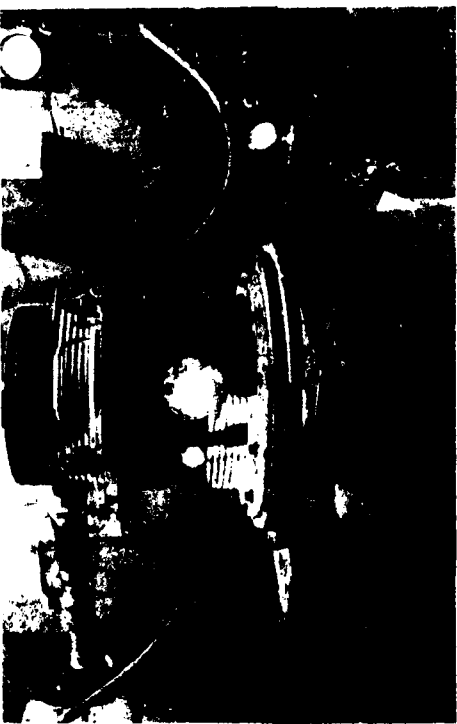
3. 3 cm Nozzle - Plate - No Mixing

CW-32	2.390	29.30	(4.25)	.84	Banded
		36.89	(5.35)		

B. DILUTION:

RUN NO.	<u>SiCl₄</u>	<u>NH₃</u>	<u>FLOW RATE (ccm)</u>	He	<u>TOTAL</u>	<u>DEP. RATE</u> g/hr
CW-32	230	68	700	-	998	2.390
CW-33	115	34	350	470	969	0.440
CW-34	82	24	250	605	961	0.482

Figure 2-1. Hot Wall Reactors. HW-4 During Deposition at 1500°C (Left). HW-1 Assembly and Power Supply (Right).



HW-4



HW-1

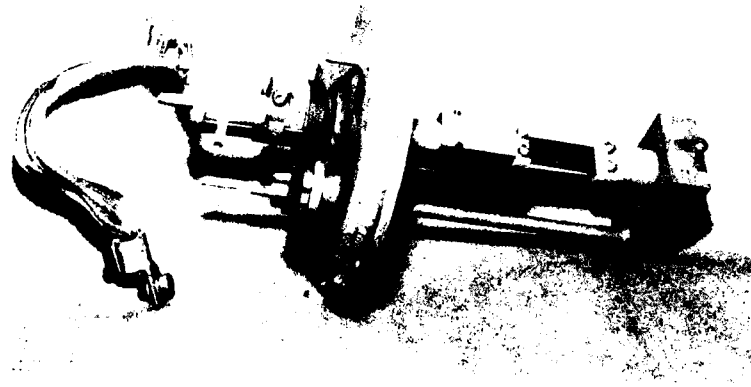
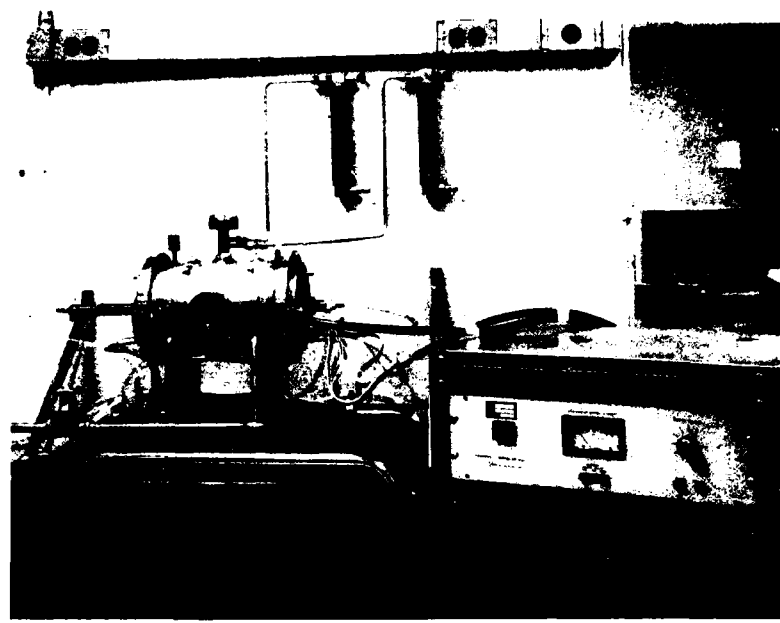


Figure 2-2. Cold Wall Reactor System (Top). Deposition Substrate Mount with Retracting Attachment to Maintain Flatness (Bottom).

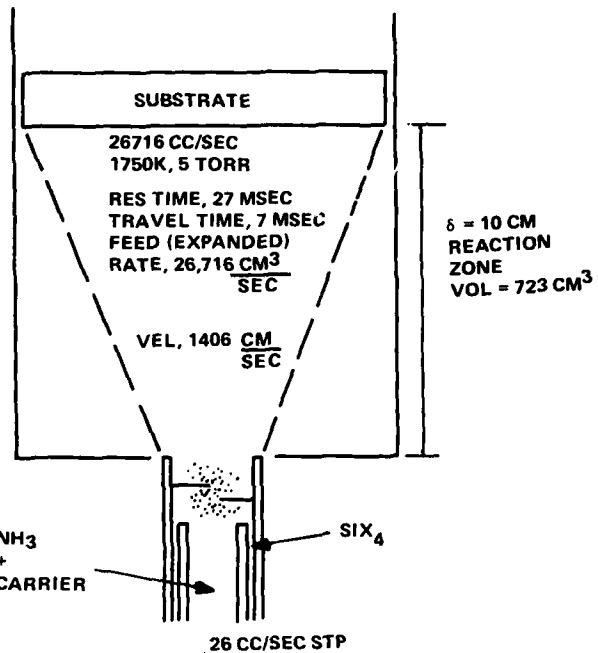


Figure 2-3(A). Typical Flow Conditions in HW-4 Using Deposition Surface Perpendicular to Flow.

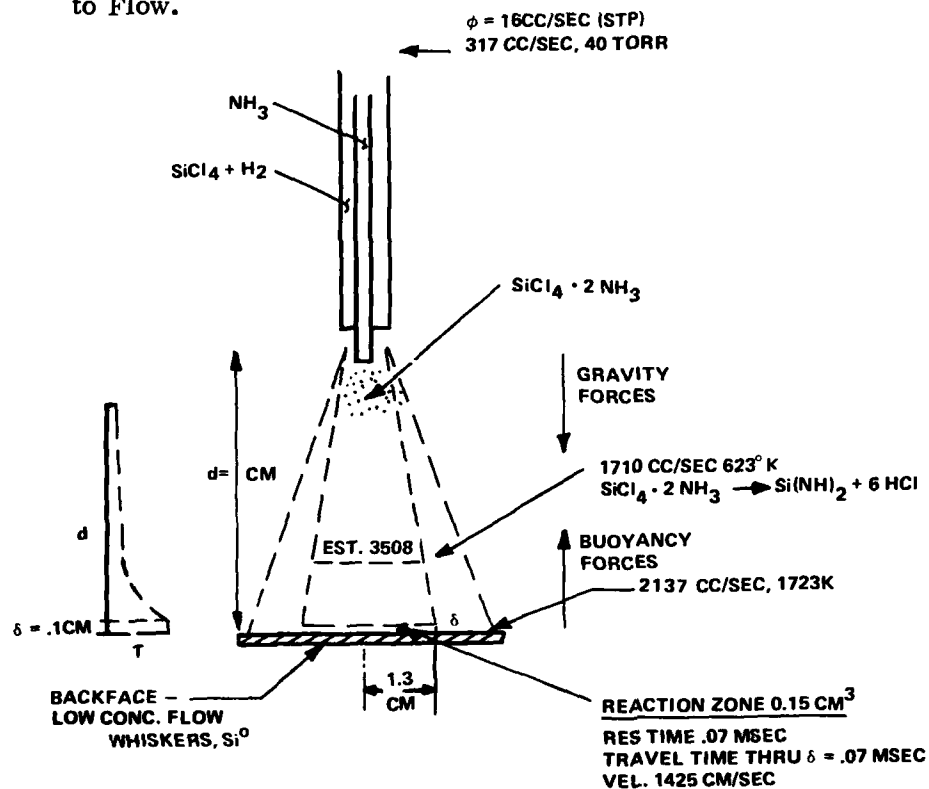


Figure 2-3(B). Flow Conditions in Cold Wall Reactor.

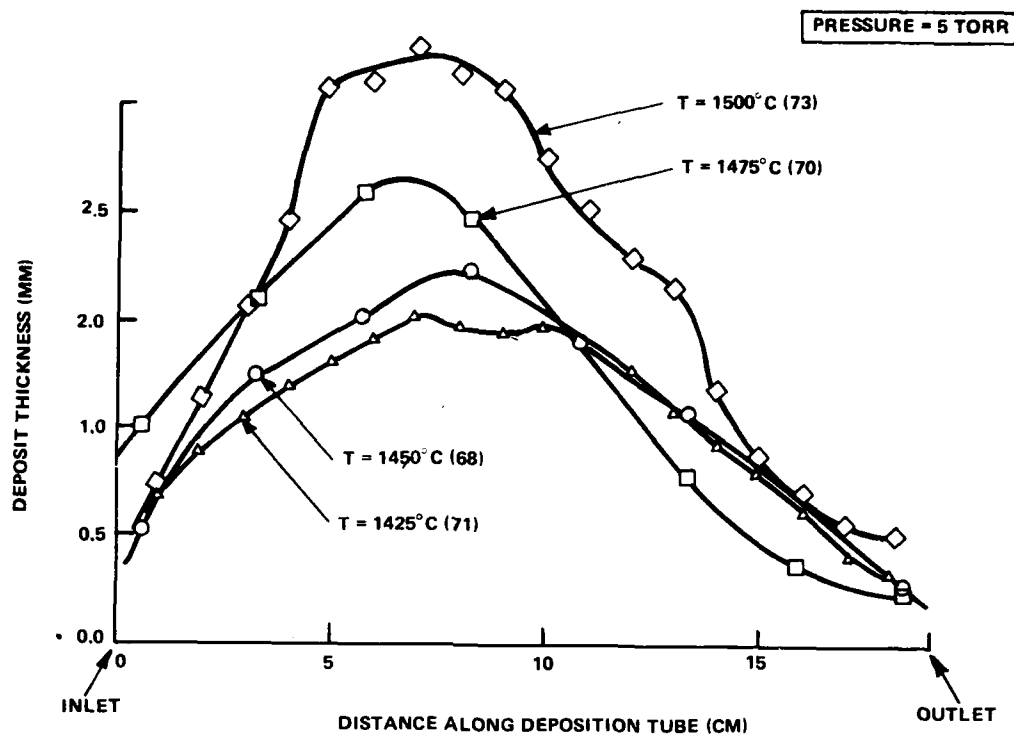


Figure 2-4(A). Deposition Profiles Showing Effect of Temperature on Deposition Rate. Pressure/Flow Conditions Constant.

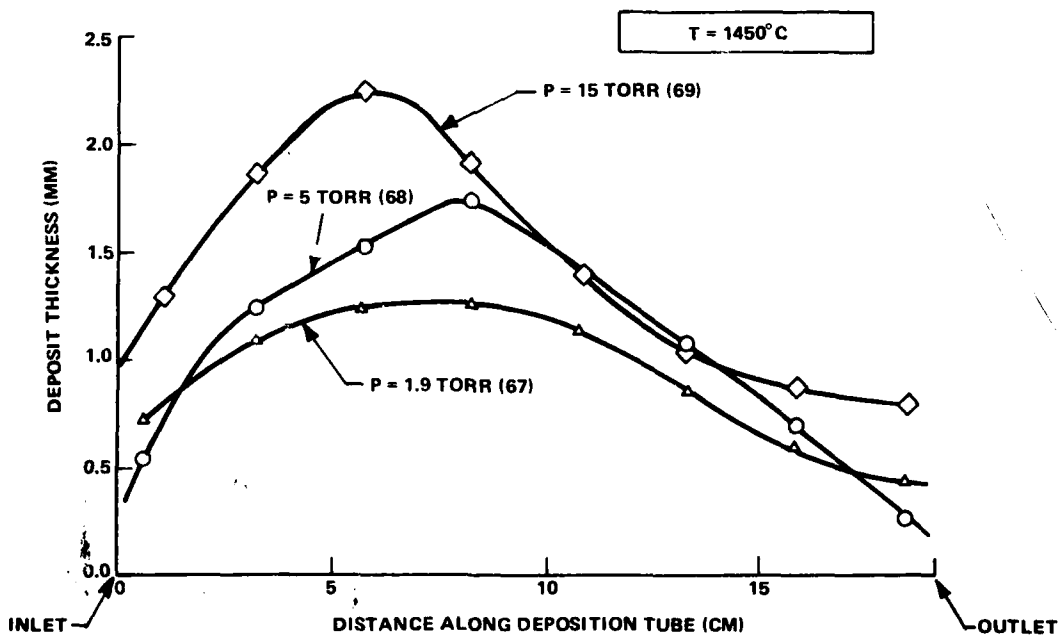


Figure 2-4(B). Deposition Profiles Showing Effect of Pressure on Deposition Rate. Temperature/Flow Conditions Constant.

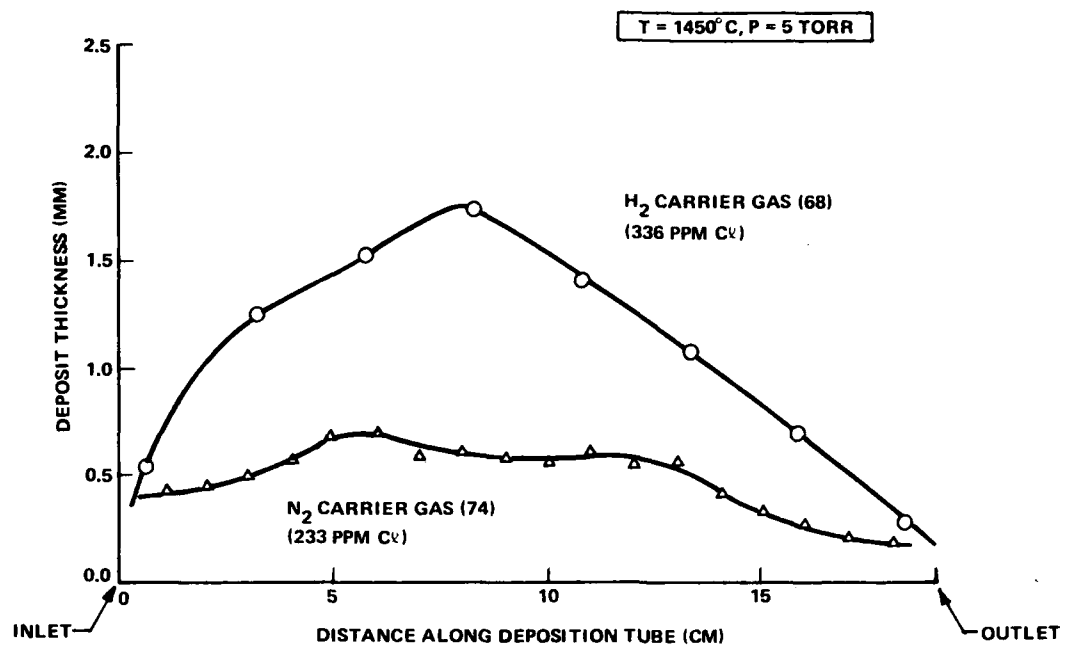


Figure 2-4(C). Deposition Profiles Showing Effect of Carrier Gas on Deposition Rate, Temp./Pressure/Total Feed Rate Constant.

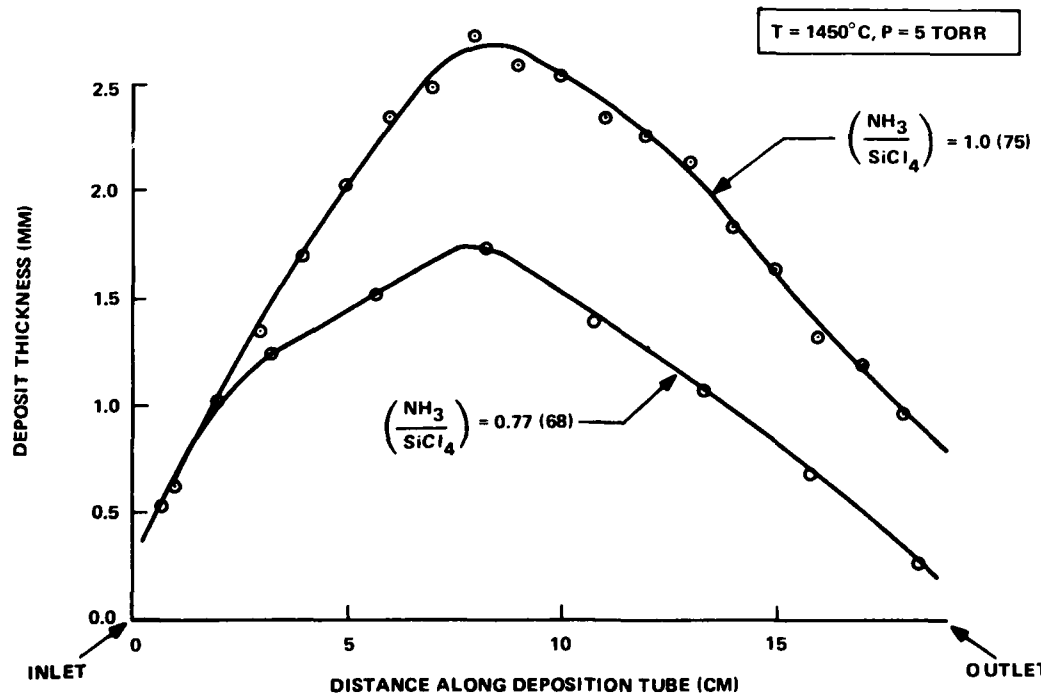


Figure 2-4(D). Deposition Profiles Showing Effect N:Si Reactant Ratio on Deposition Rate. Temperature/Pressure Constant.

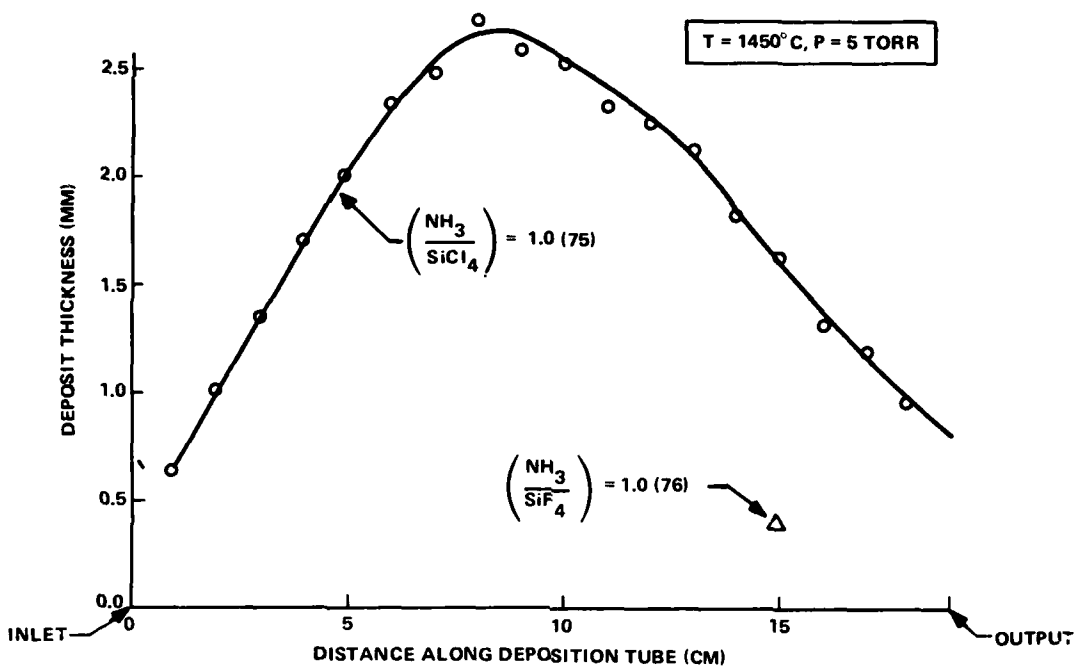


Figure 2-4(E). Deposition Profiles Showing Effect of Type of Si-bearing Reactant on Deposition Rate.

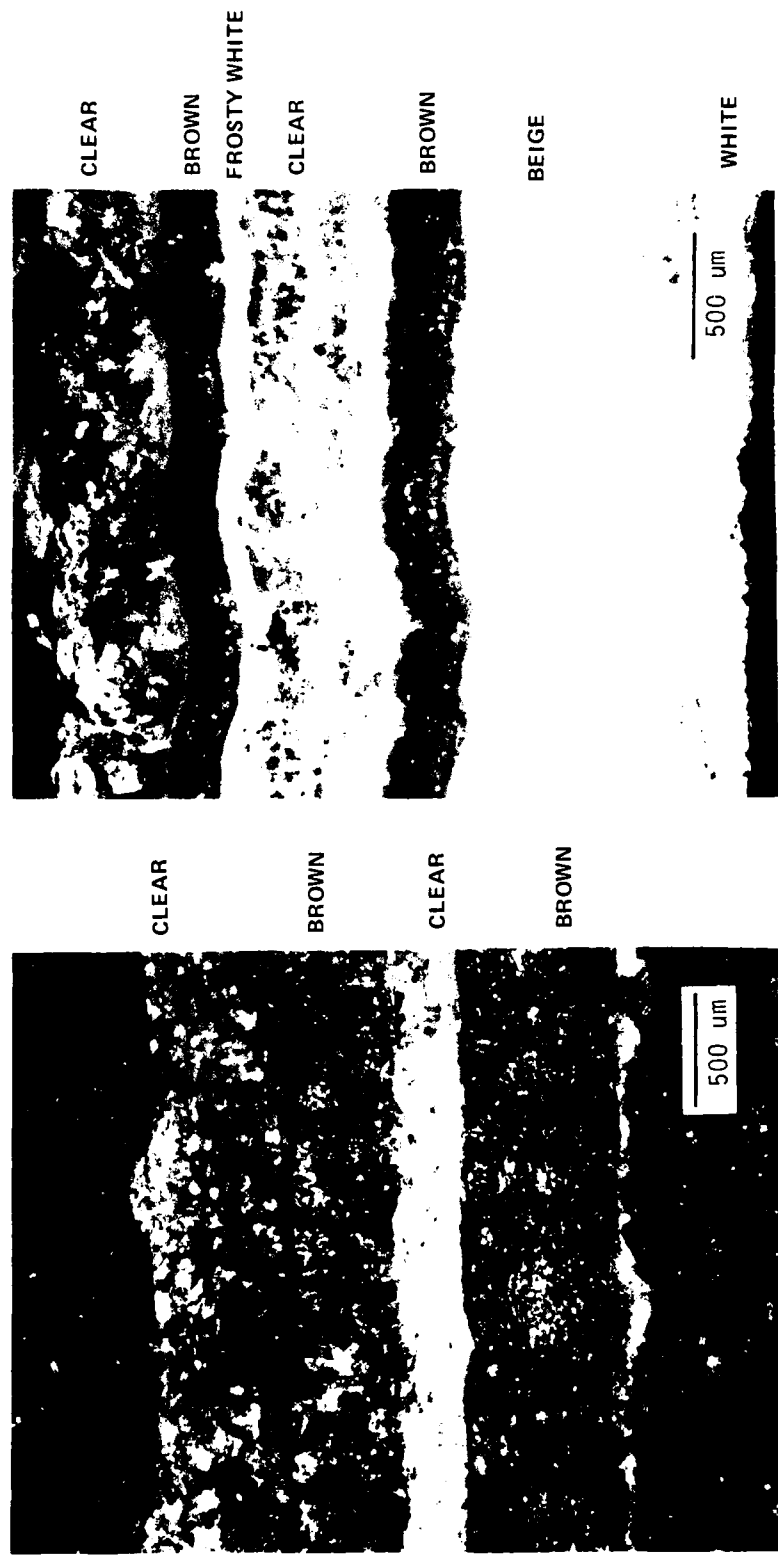


Figure 2-4(F). Typical Cross-Sections of Deposits Showing a Multilayer Morphology (Banding).

HW-1-68		KNOOP (KG/MM ²)		
		100g	500g	1000g
Amorph.	2065	1887	1767	
Cryst.	2331	2059	1947	

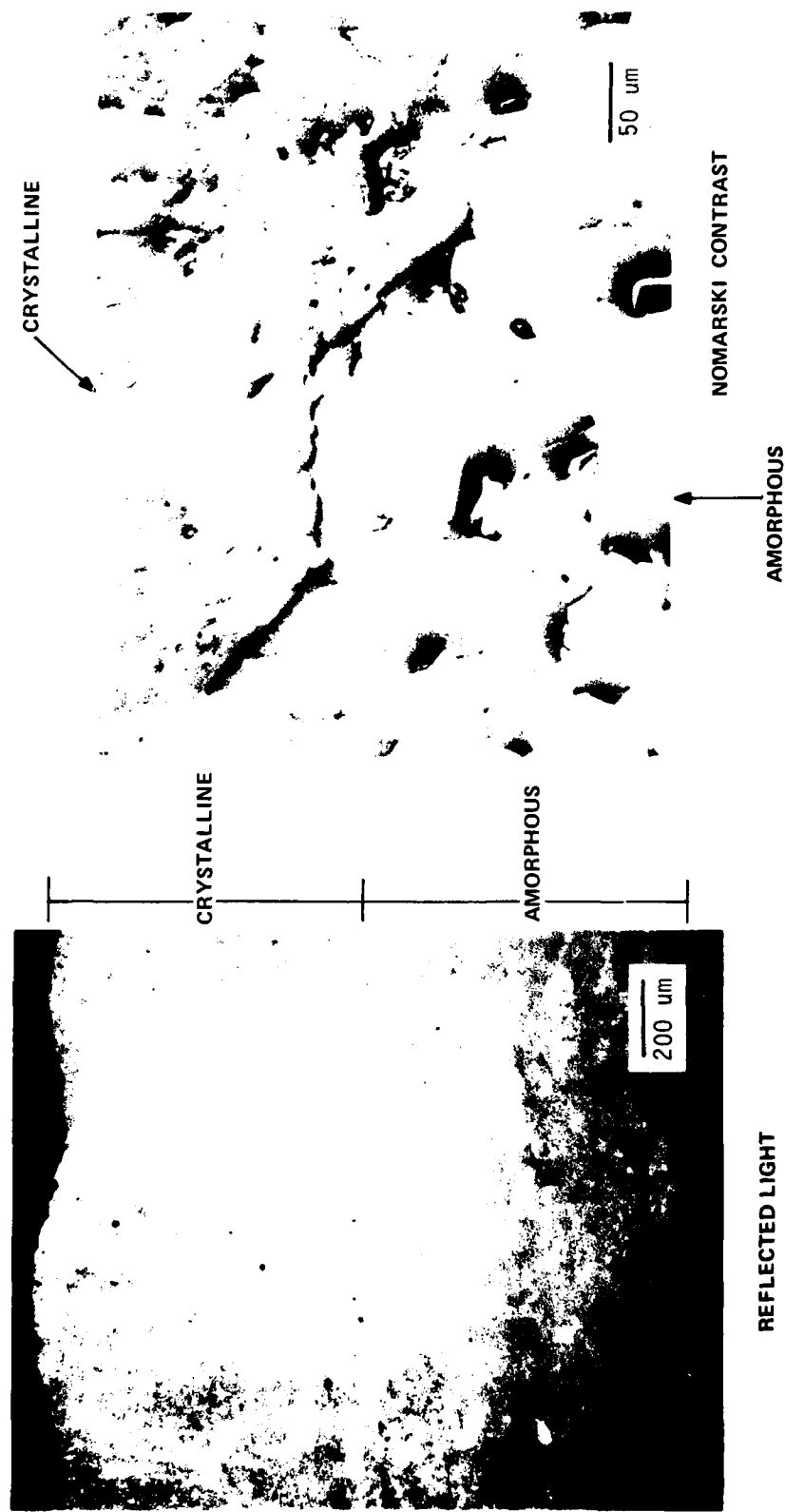


Figure 2-4(G). Photomicrographs Showing Transition from Amorphous to Crystalline Morphology (Run No. HW-1-68).

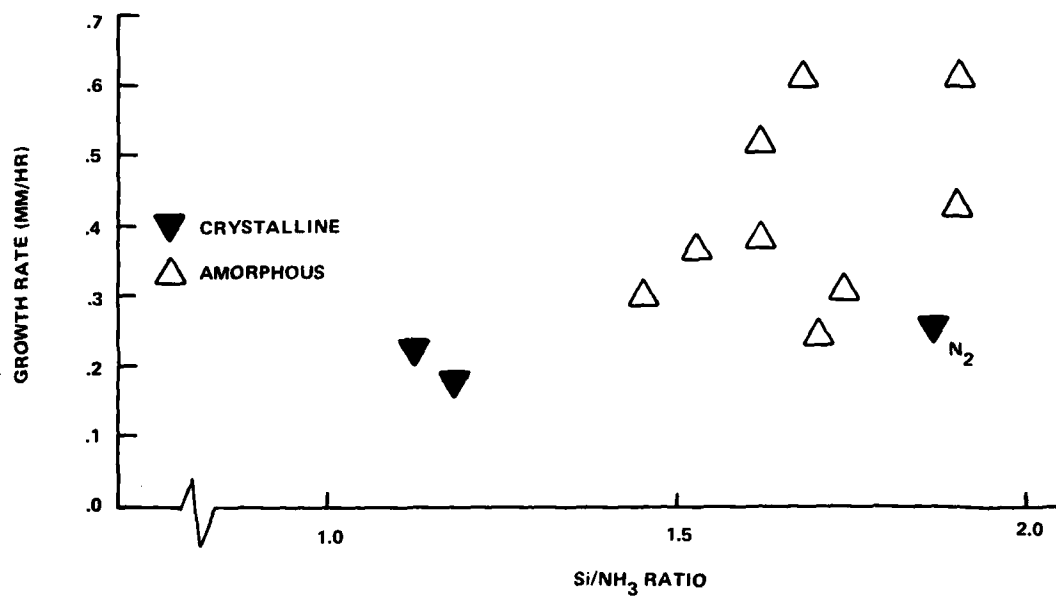
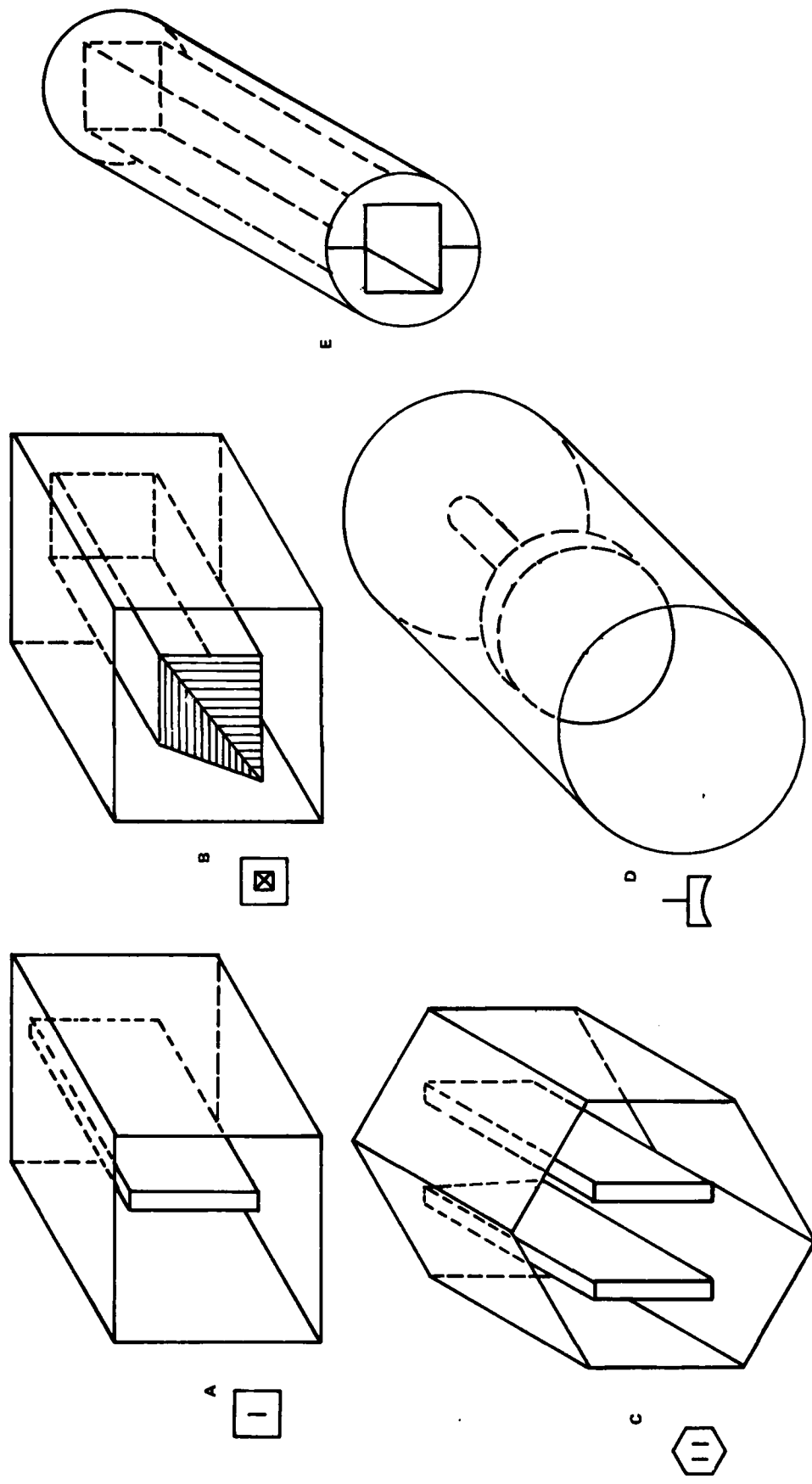


Figure 2-5. Growth Rate (mm/hr) vs. Si/N Ratio in HW-1 Runs.



A. SQUARE BOX – PLATE INSERT
 B. SQUARE BOX – SQUARE PLUG INSERT
 C. HEXAGONAL BOX – TWO PLATES INSERTED
 D. PLATE OR DOME, PERPENDICULAR TO FLOW
 CHANNEL, HW-1 GEOMETRY, GRAFOIL LINER.
 E.

Figure 2-6. Schematics of Deposition Geometries Used in Hot Wall Deposition Runs,
View from GAC Inlet

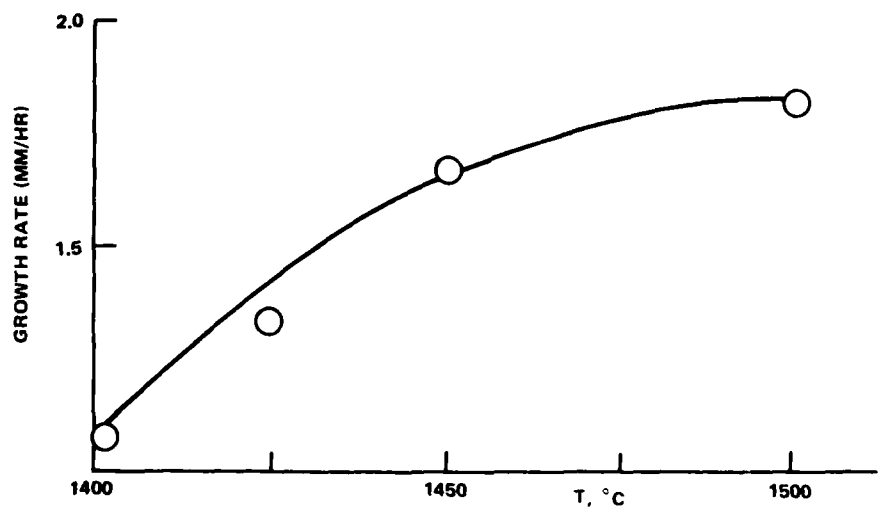


Figure 2-7. Growth Rate (mm/hr) vs. Deposition Temperature in Cold Wall Deposition Runs CW 14-19.

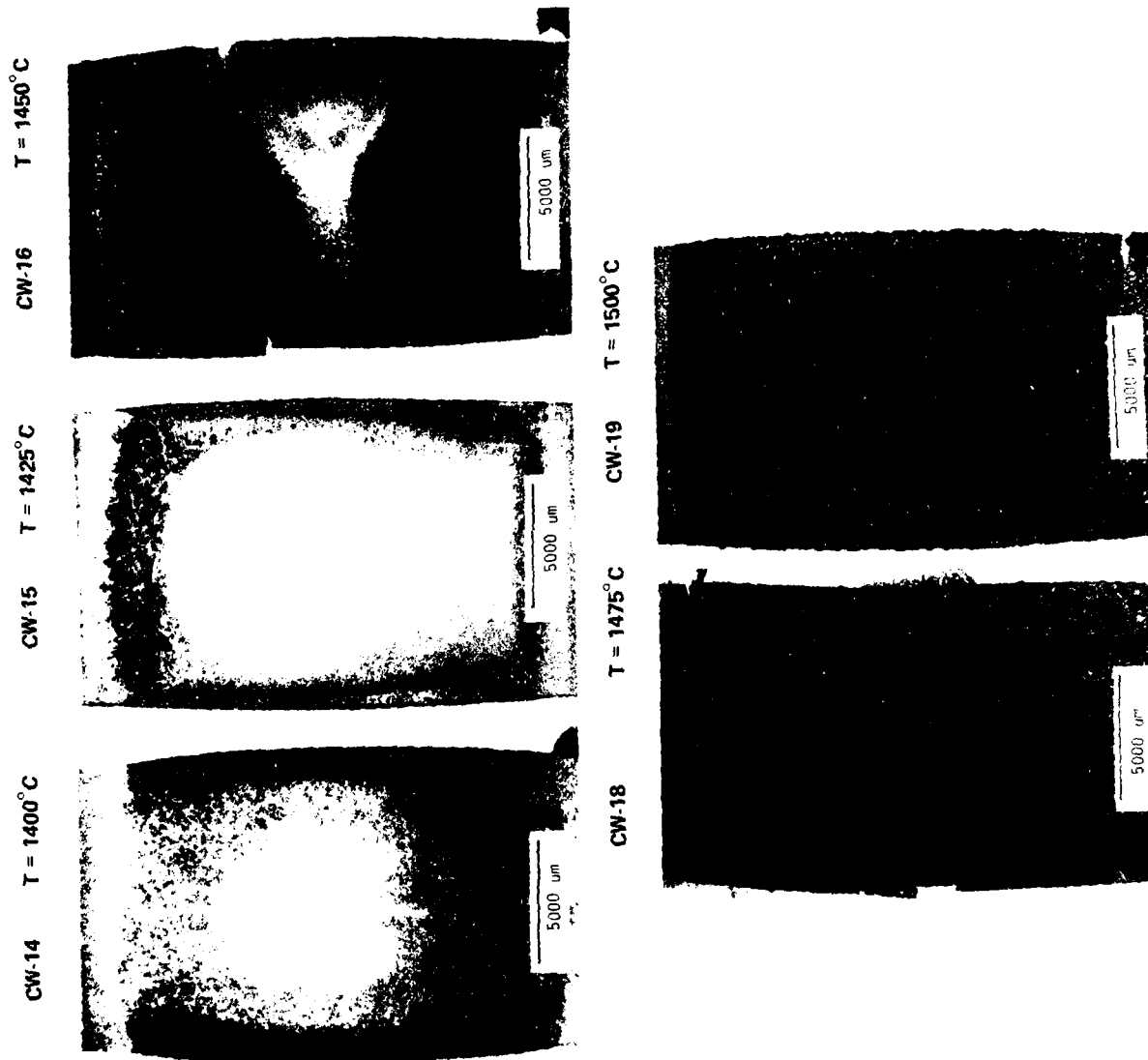


Figure 2-8. Last Deposited Surfaces of Si_3N_4 Deposited at Various Temperatures.

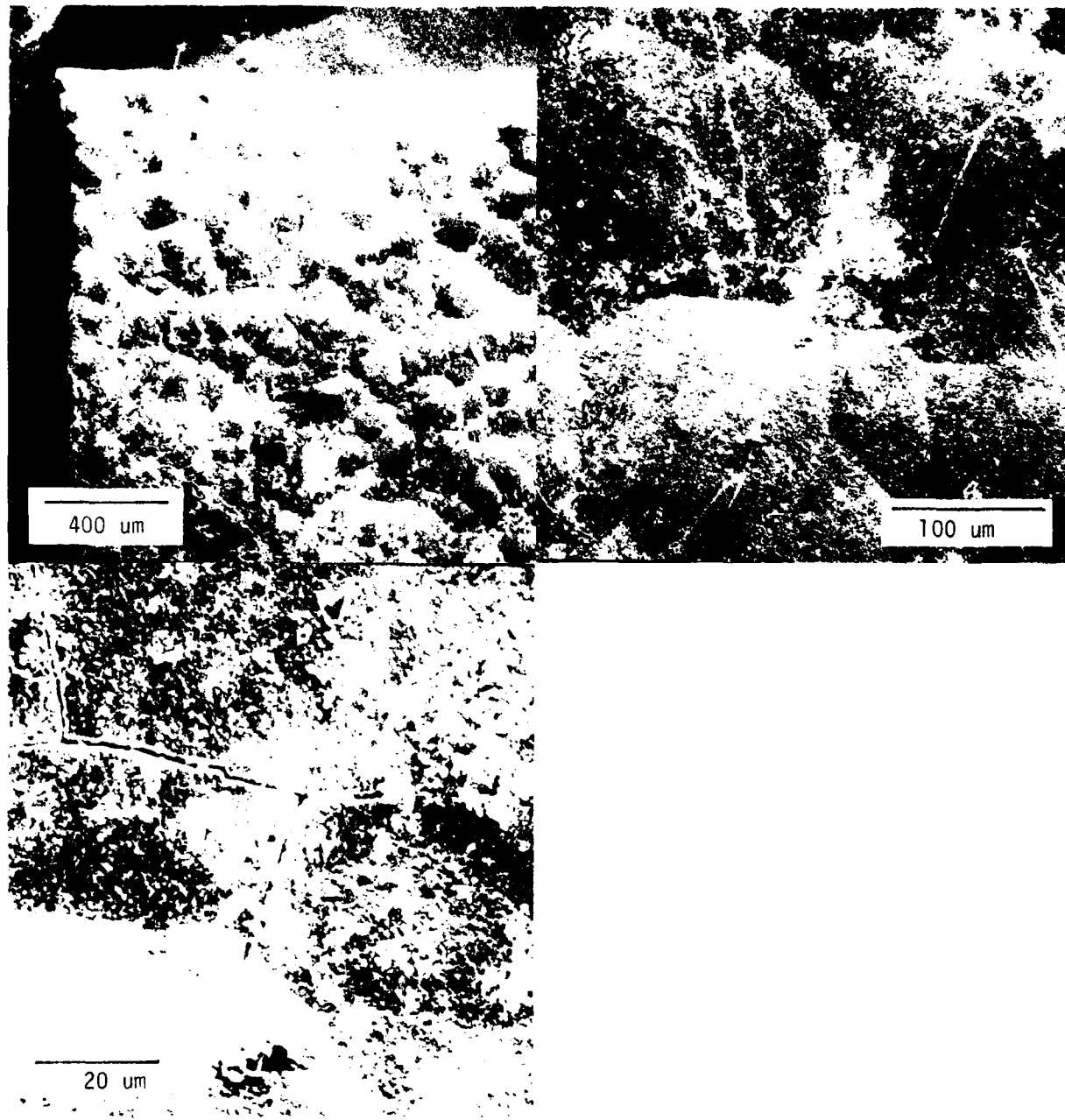


Figure 2-9. Last Deposited Surface of Flexure Bar Cut from Run CW-15, MOR = 18.62 MPa, Showing Surface Cracks in Amorphous Region.



Figure 2-10. Fracture Surface of Flexure Bar 15-1 Cut from Run CW-15, T_{DEP} = 1425°C
MOR = 18.62 MPa (2.7 Kpsi). Note Banded Structure and Vertical Cracks
within Bands.

CW-39 FLOW RATE = 356 CCM CW-43 FLOW RATE = 856 CCM



CW-40 FLOW RATE = 1356 CCM CW-41 FLOW RATE = 1856 CCM CW-42 FLOW RATE = 178 CCM

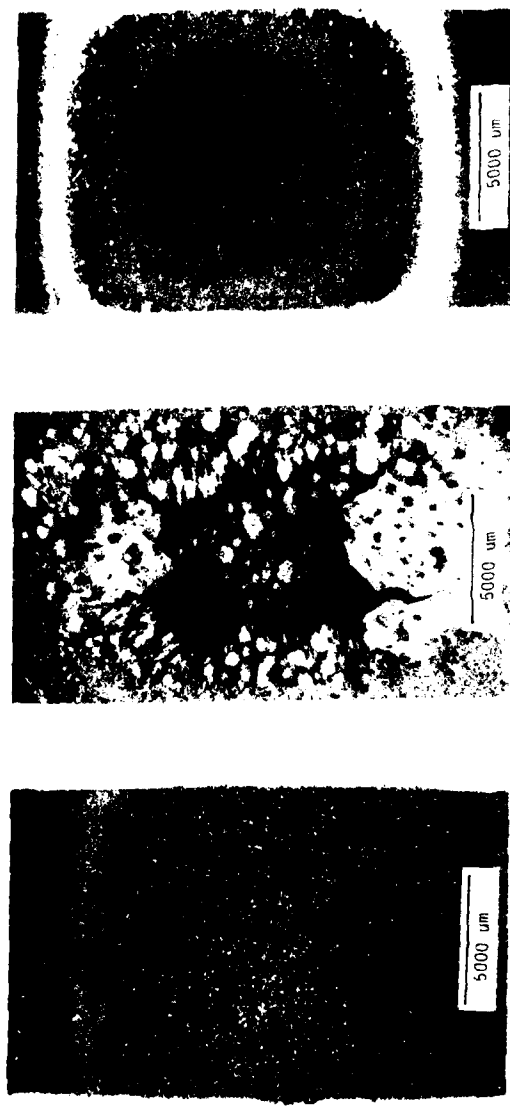


Figure 2-11. Last Deposited Surfaces of Si_3N_4 Deposited at Constant $\text{SiCl}_4/\text{NH}_3$ Ratio (3.42) and Various Total Feed Rates and Dilutions.



Figure 2-12. Whiskers and Ribbons of Si₃N₄ Deposited with no Diluent and at Low Total Flow Rate (Run 39 - 356 cc/min).

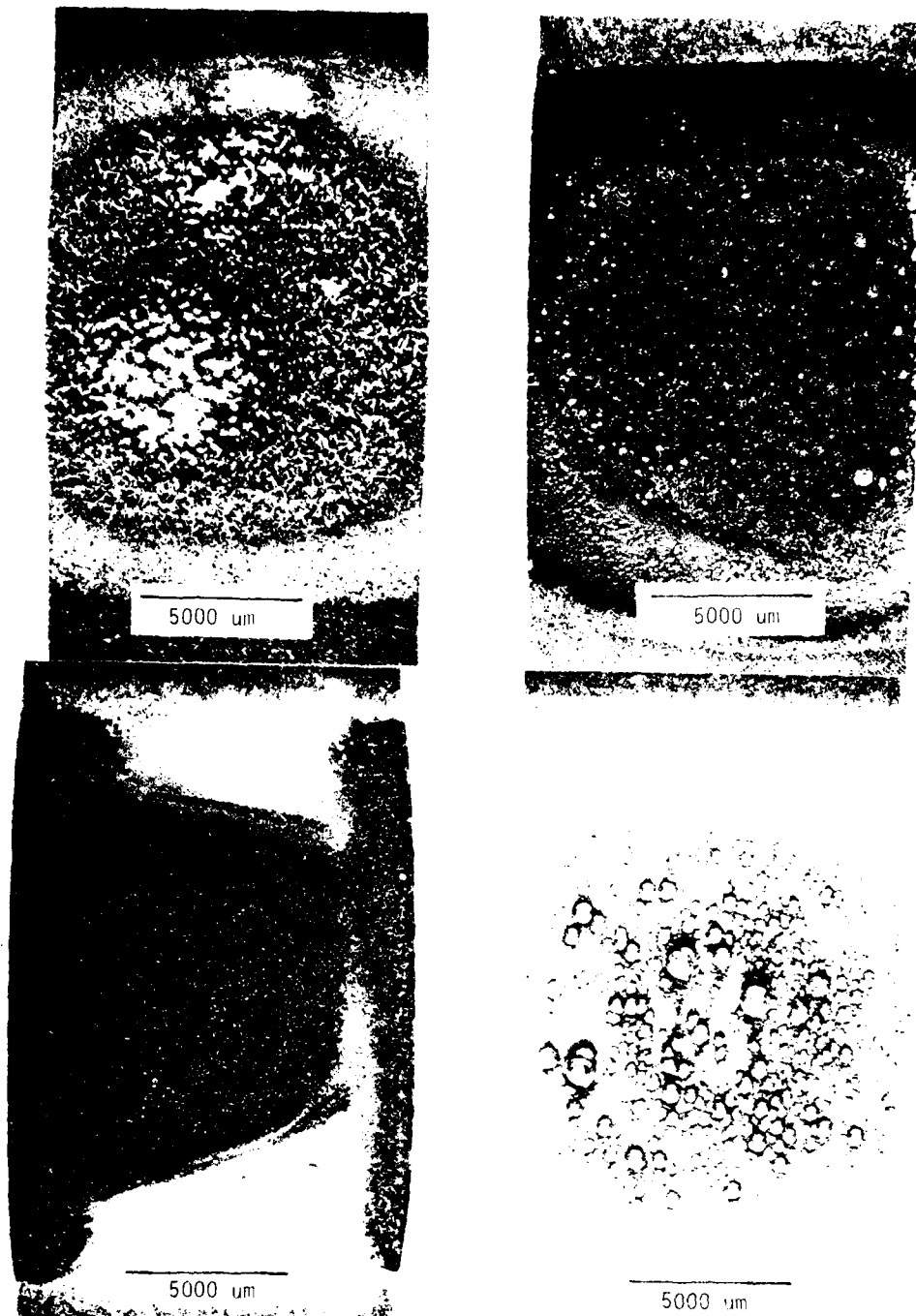


Figure 2-13. Last Deposited Surfaces of Si_3N_4 Deposited at Constant Total Flow and Varying $\text{SiCl}_4/\text{NH}_3$ Ratio.

Top Left: Run 38 $\text{Si}/\text{N} = 14.3$

Top Right: Run 37 $\text{Si}/\text{N} = 7.7$

Bottom Left: Run 36 $\text{Si}/\text{N} = 2.6$

Bottom Right: Run 35 $\text{Si}/\text{N} = 0.67$

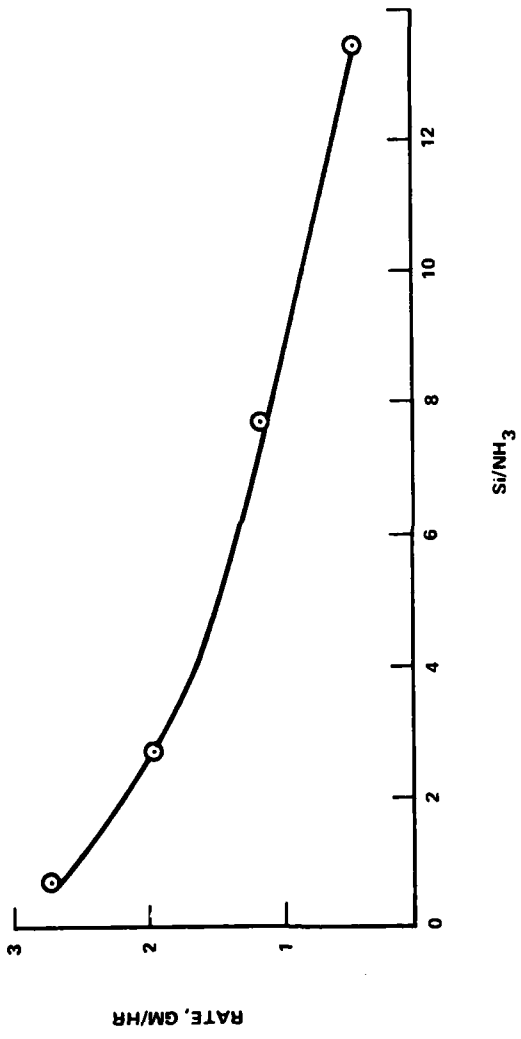


Figure 2-14. Mass Deposition Rate vs. Si/N Ratio (Constant Temperature, Pressure, Flow Rate).

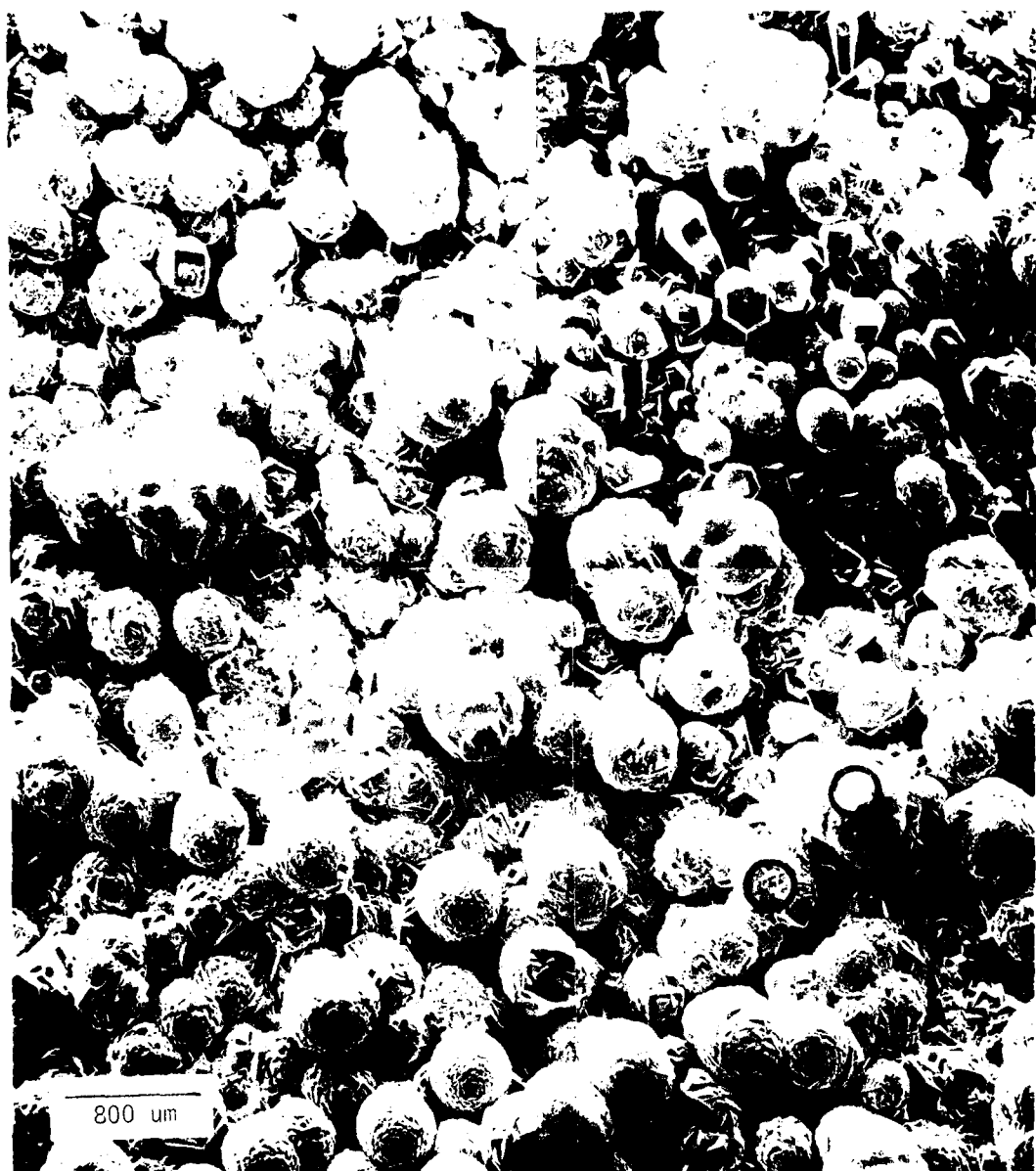


Figure 2-15. Montage of Si₃N₄ Deposited at Si/N Ratio of 7.7 (Run CW-37), Showing Various Growth Habits.

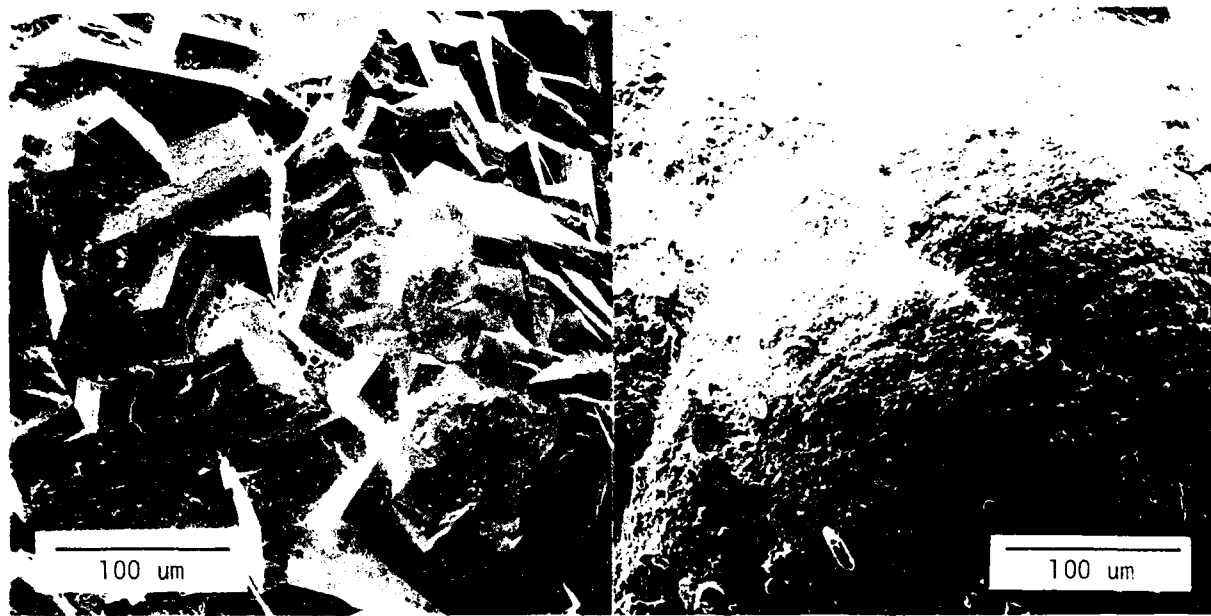


Figure 2-16. Detail Views of Regions Circled in Figure 15. Left View Shows Faceted Nodule with Web-like Structures at Crystallite Boundaries While Right View also Shows Regions with Less Definite Boundaries

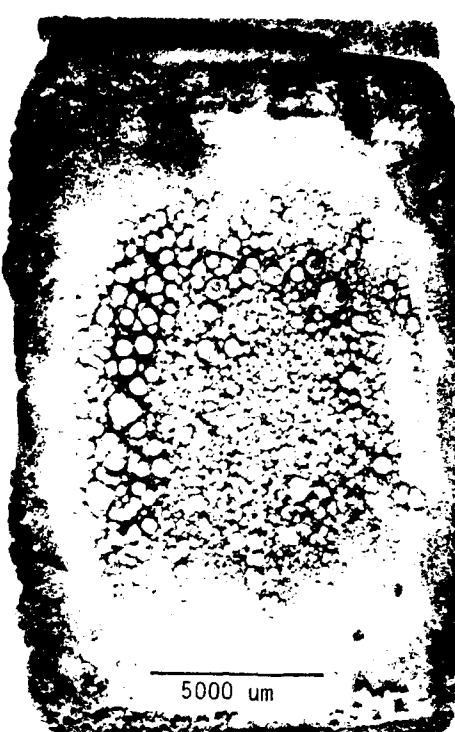


Figure 2-17. Detailed Views of Fine Whiskers Deposited with Helium Dilution and Very Low Ammonia Content ($\text{Si}/\text{N} = 13.6$). Run No. CW-38.

RUN NO. CW-46



RUN NO. CW-47



RUN NO. CW-48

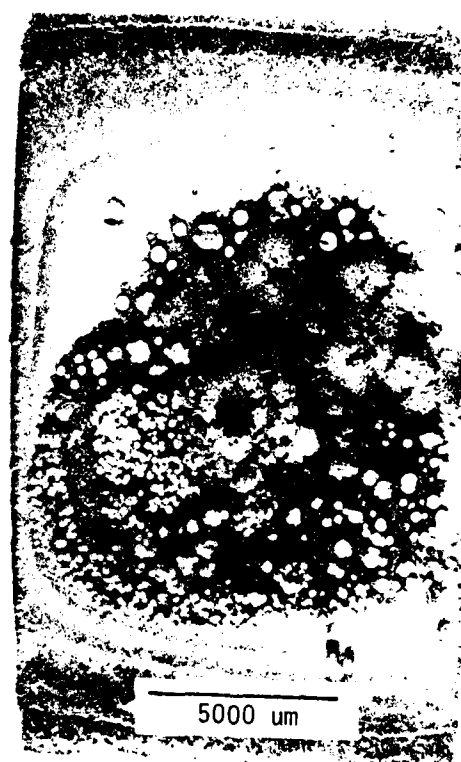


RUN NO. CW-49

Figure 2-18. Deposits Obtained Using Dichlorosilane (H_2SiCl_2) - Ammonia Mixtures.
Top: Temperature = $1475^{\circ}C$; Bottom: Temperature = $1400^{\circ}C$ (left) and
 $1100^{\circ}C$ (right).



RUN NO. CW-44



RUN NO. CW-45

Figure 2-19. Deposits obtained from Trichlorosilane-Ammonia Mixture at 1475°C.
Left: Si/N = 3.8; Right: Si/N = 7.7.

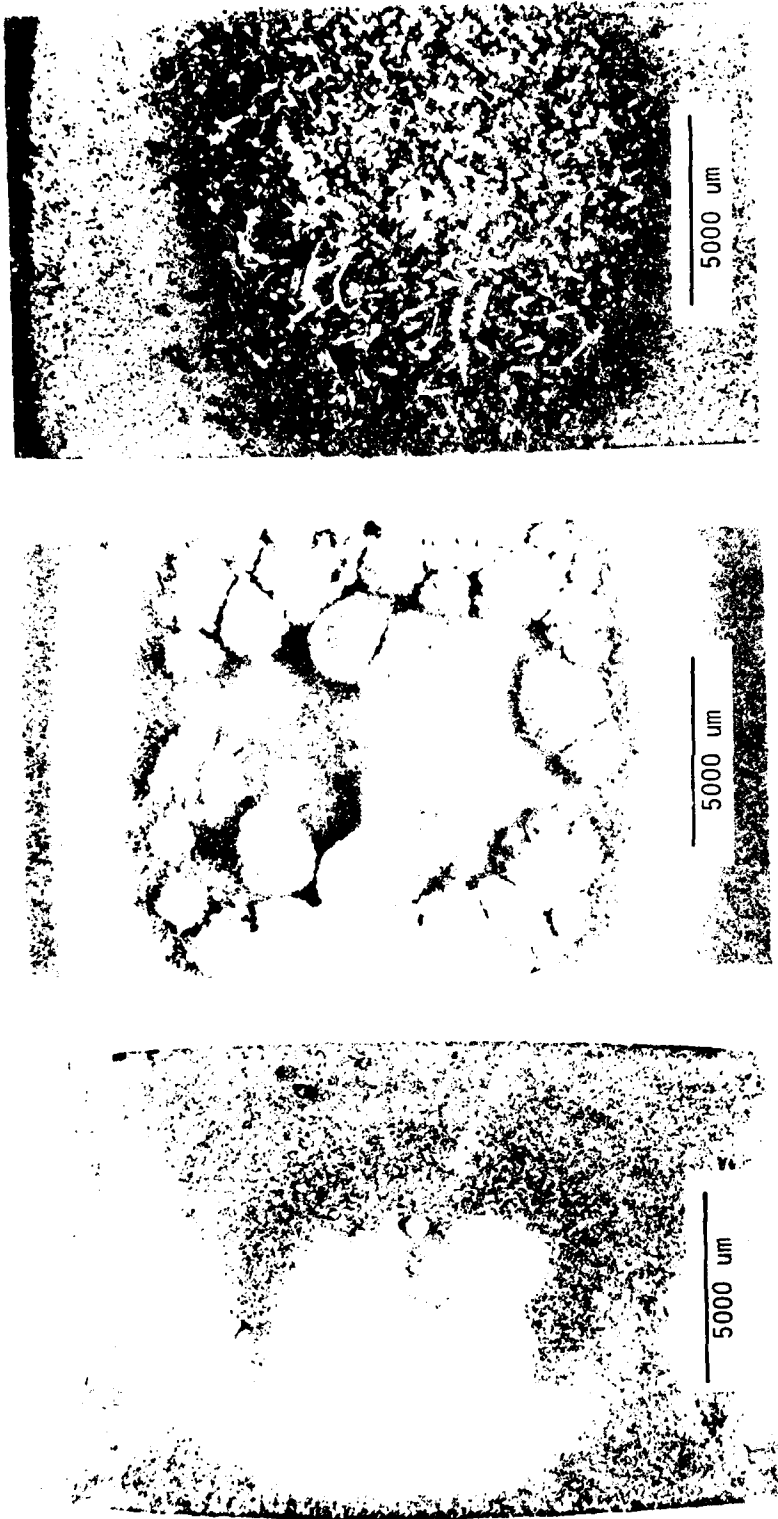
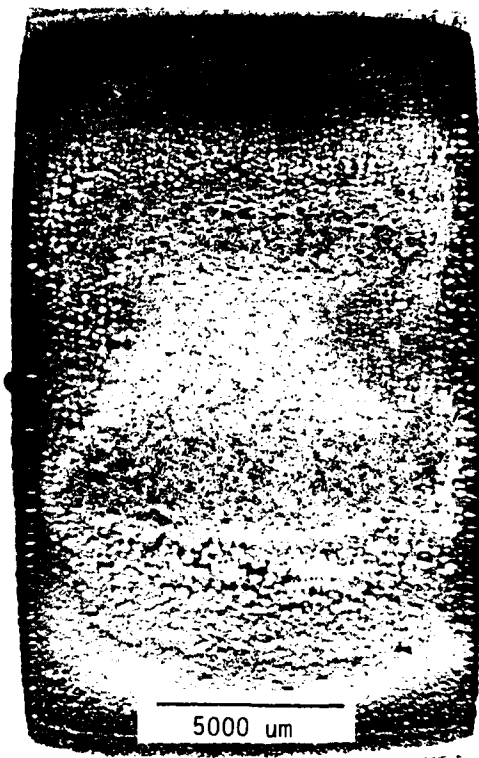


Figure 2-20. Deposits Obtained at Constant Si/N Ratio (3.4) and Total Flow, but with Increasing Helium Dilution. Left: No Helium Added, Center-Diluted by 50%; Right - Diluted by 67%.



RUN NO. CW-31



RUN NO. CW-30

Figure 2-21. Influence of Moving Feed Nozzle Closer to Deposition Substrate. Left: 3 cm distance; Right: 5 cm distance.

RUN NO. CW-23 (2 DAYS EXPOSURE)

2000 um

RUN NO. CW-23

2000 um

RUN NO. CW-22

2000 um



Figure 2-22. Deposits of Intermediates on Substrate at Room Temperature. Left:
 $\text{Si}/\text{N} = 2.5$; Center, $\text{Si}/\text{N} = 1$. Right: $\text{Si}/\text{N} = 1$ After Two Days Air
Exposure.

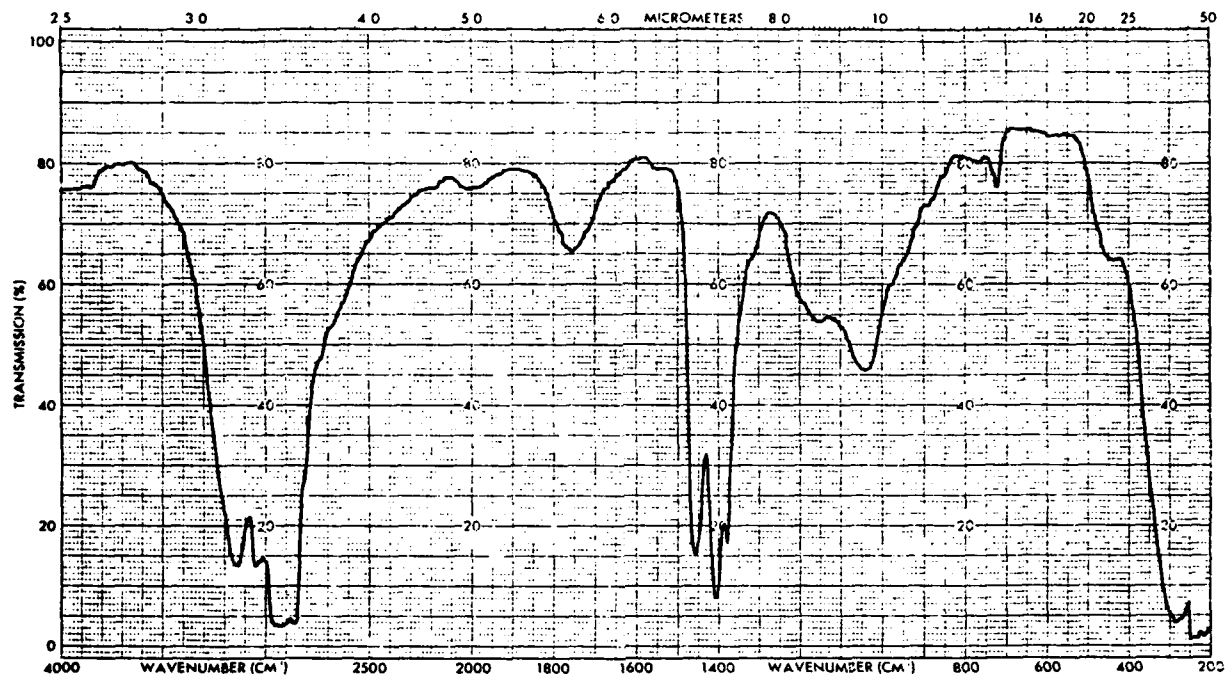


Figure 2-23. Infrared Spectrum of Intermediates Obtained at $\text{Si}/\text{N} = 0.5$ in Nujol.

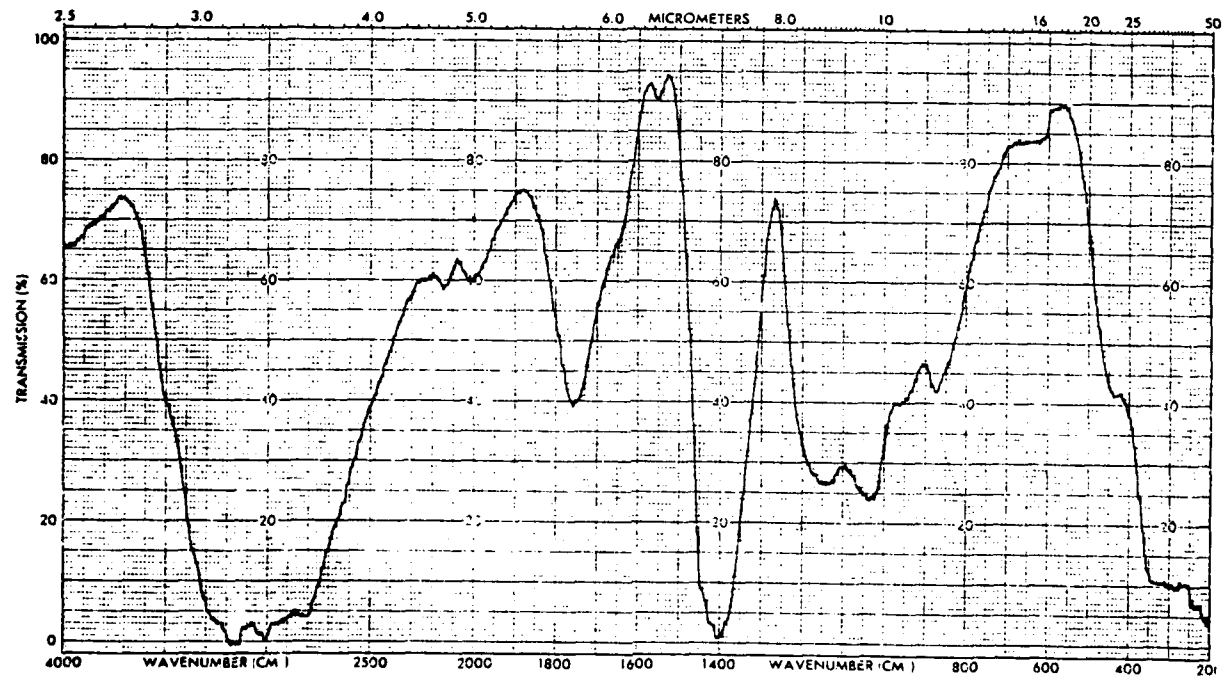


Figure 2-24. Infrared Spectrum of Intermediates Obtained at $\text{Si}/\text{N} = 0.5$ in KCl.

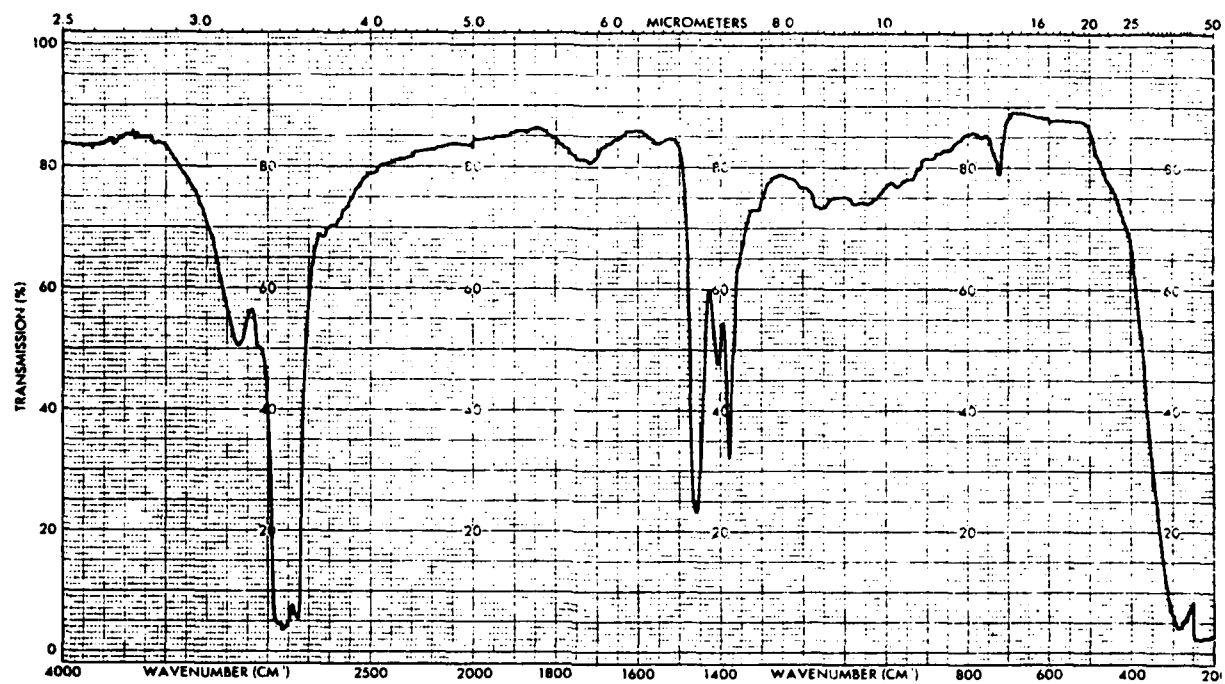


Figure 2-25. Infrared Spectrum of Intermediates Obtained at Si/N = 1.0 in Nujol.

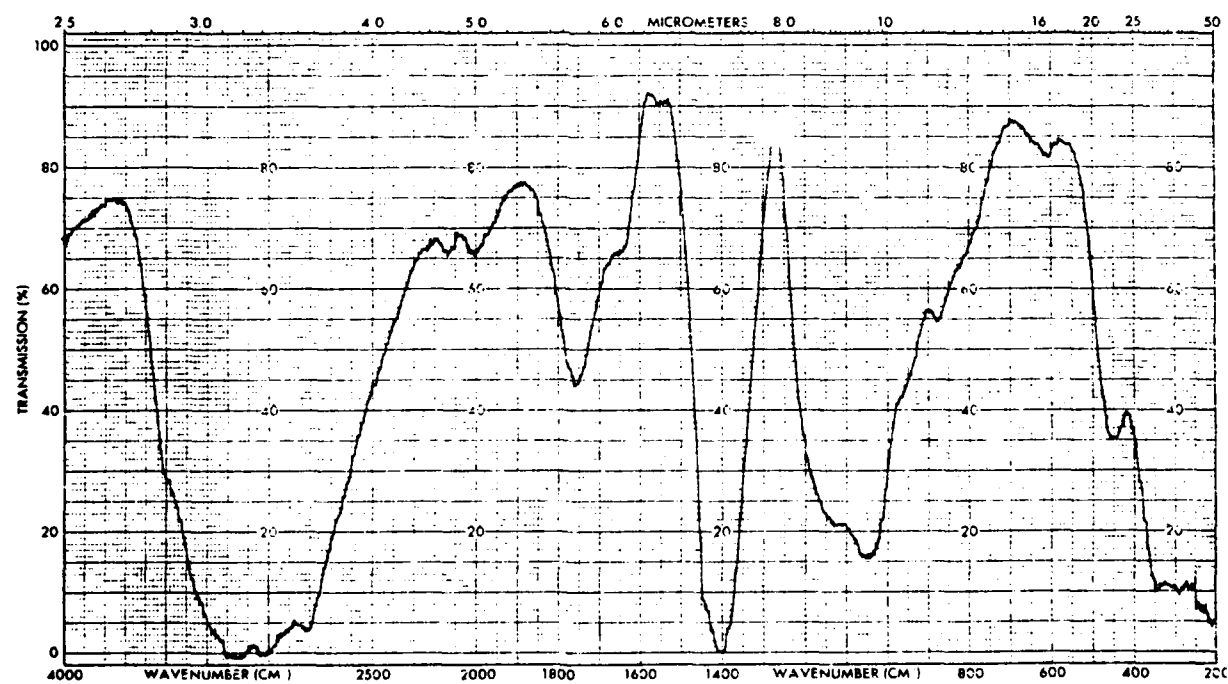


Figure 2-26. Infrared Spectrum of Intermediates Obtained at Si/N = 1.0 in KC1.

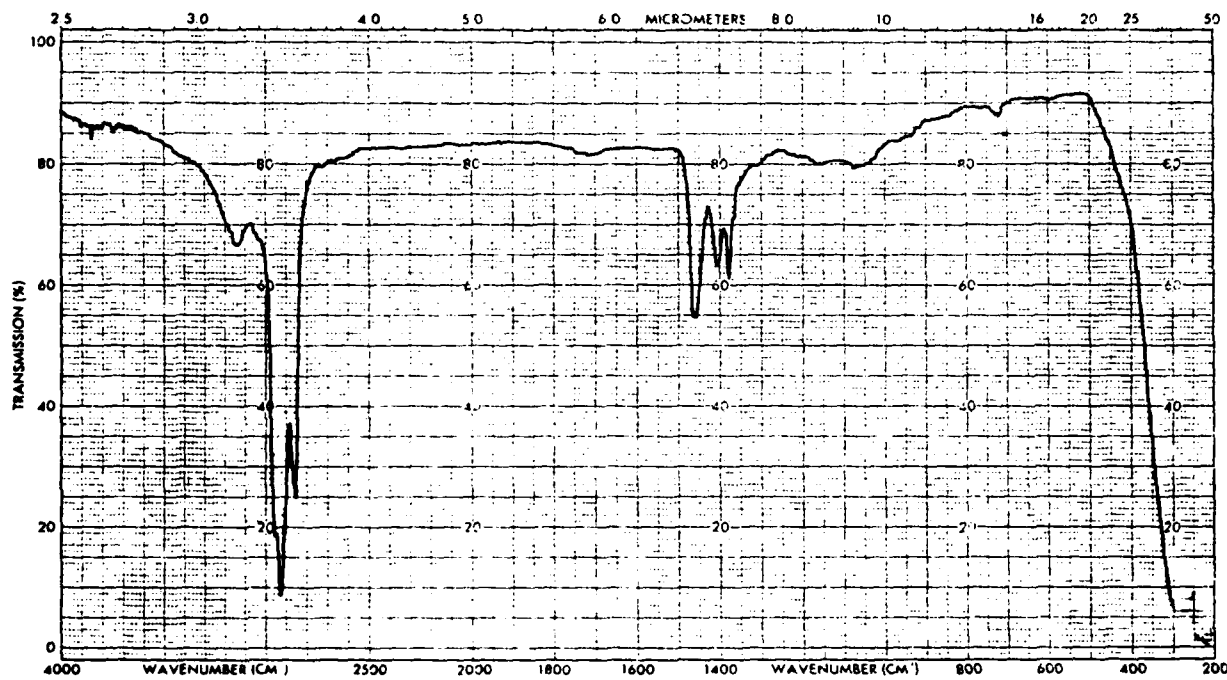


Figure 2-27. Infrared Spectrum of Intermediates Obtained at $\text{Si}/\text{N} = 2.5$ in Nujol.

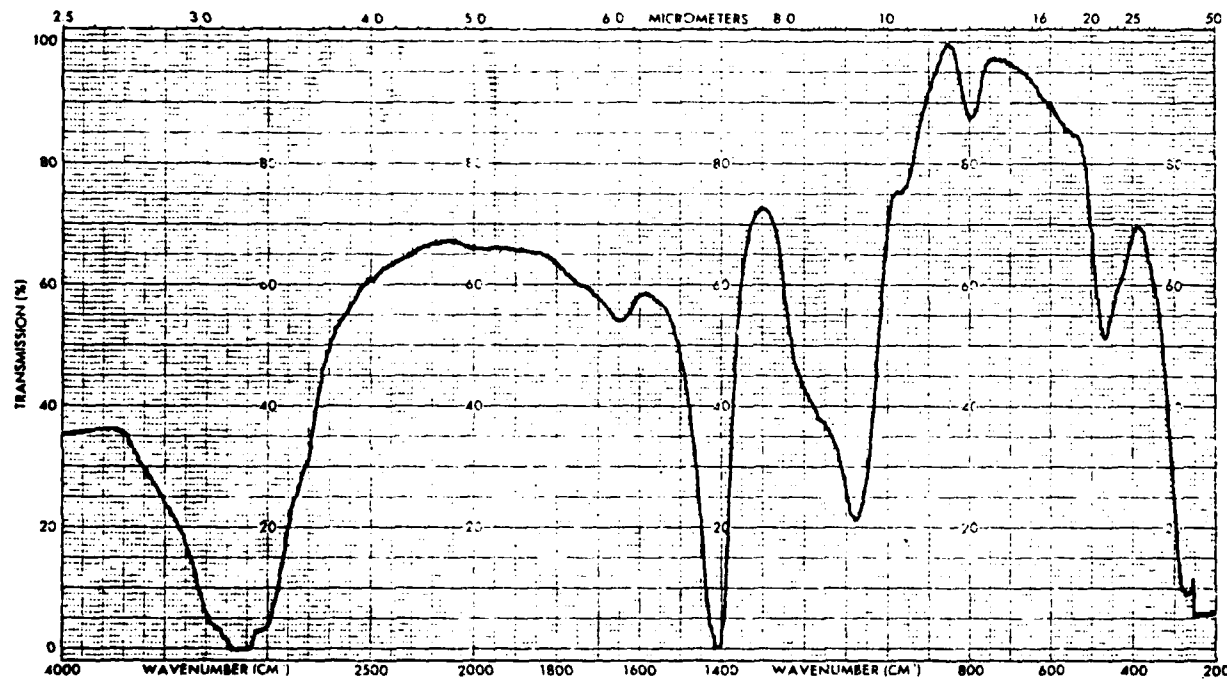


Figure 2-28. Infrared Spectrum of Intermediates Obtained at $\text{Si}/\text{N} = 2.5$ in KCl.

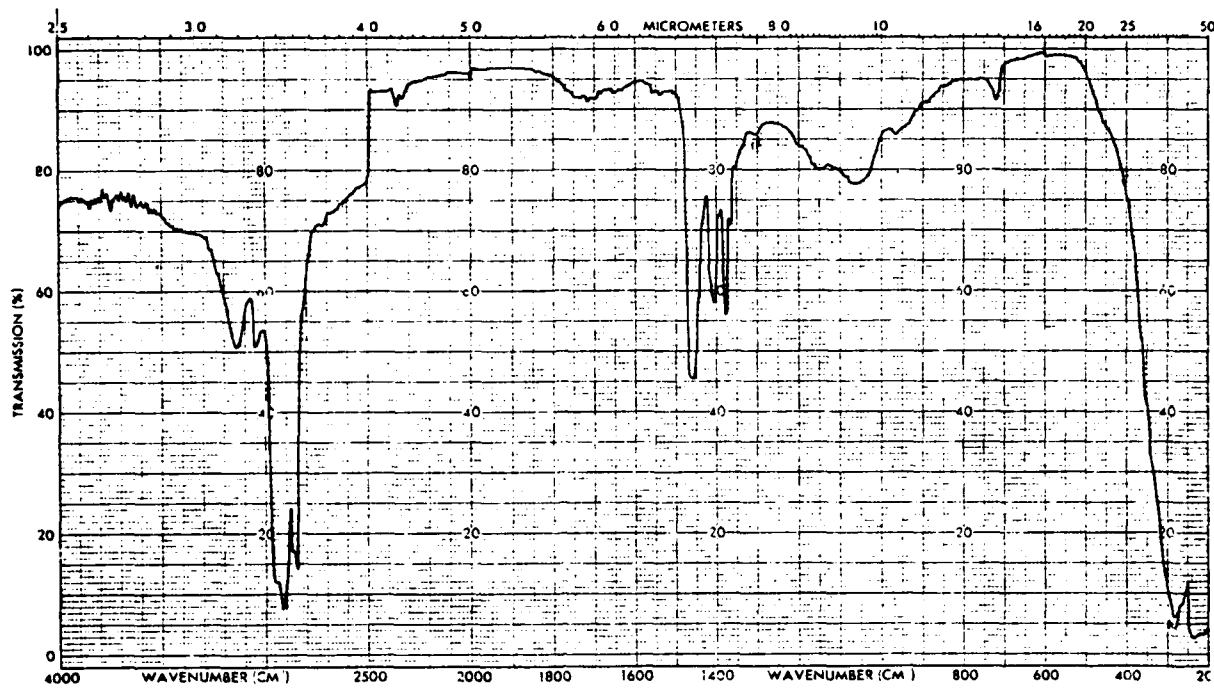


Figure 2-29. Infrared Spectrum of Intermediate Obtained at $\text{Si}/\text{N} = 1.0$ After 48 hours Exposure to Air In Nujol.

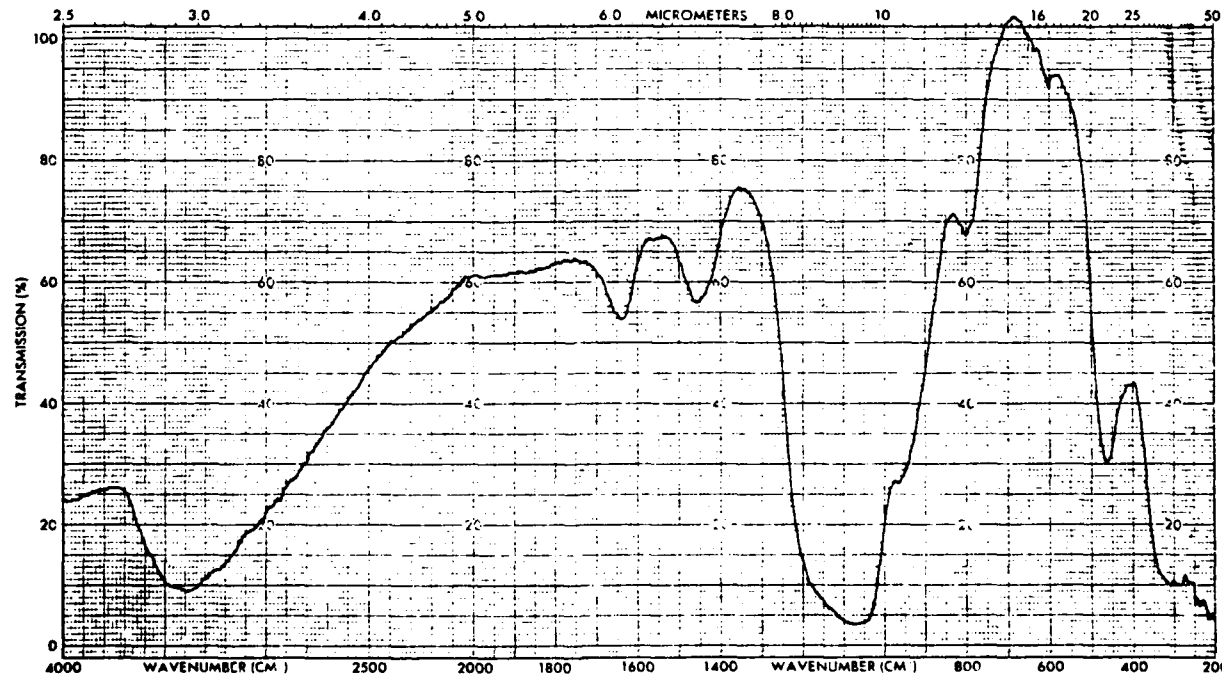


Figure 2-30. Infrared Spectrum of Residue of DTA/TGA analysis of $\text{Si}/\text{N} = 1$ Intermediate In KC1.

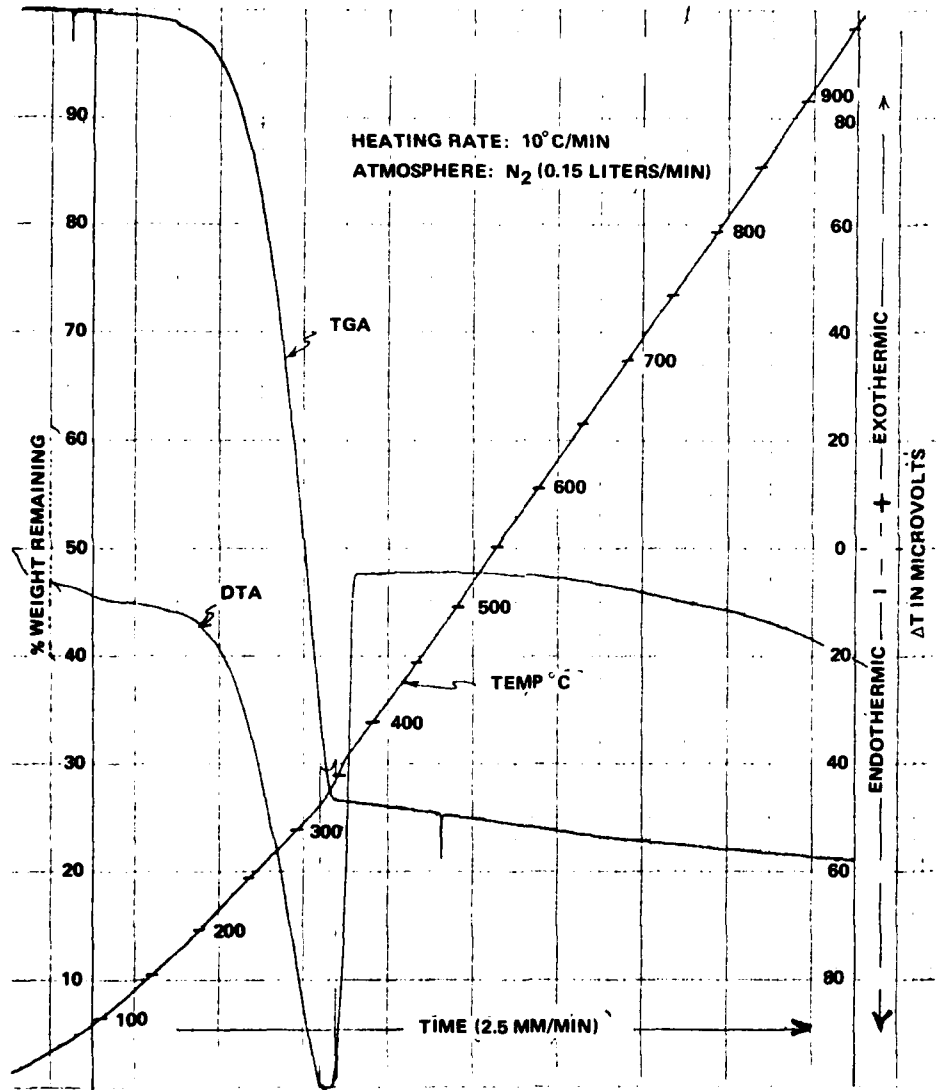


Figure 2-31. Typical DTA/TGA Curve of Intermediate Compound.



Figure 2-32. Edge Effect on Cold Wall Reactor Substrate Showing Crystalline Faceted Deposit (Top) on Upper Surface Edge Becoming Finer Grained on Lower Edge.

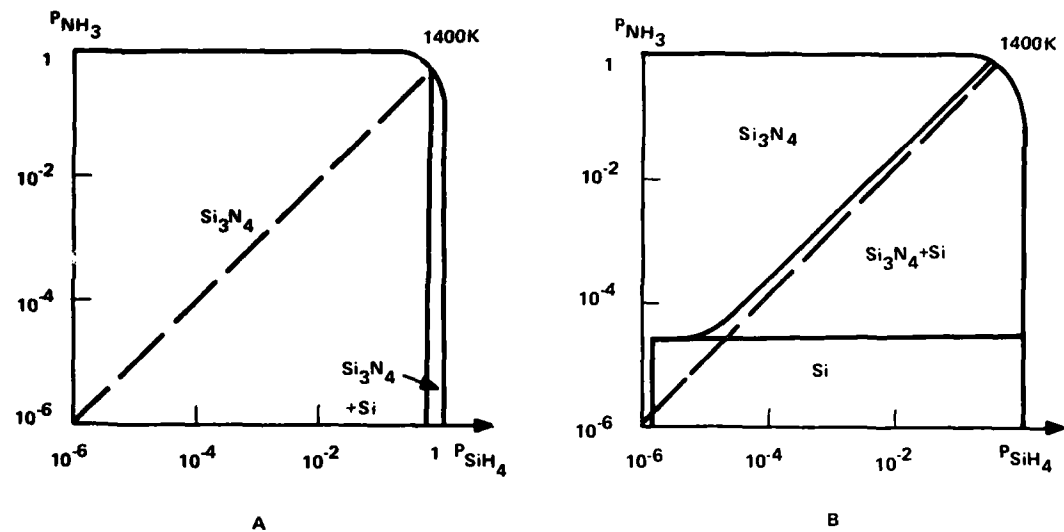


Figure 2-33. Deposition Domains as Function of Initial Pressure for $T = 1400\text{K}$, $P = 1 \text{ atm}$.
 A. Dilution with N_2
 B. Dilution with H_2 (Ref. 2-7)

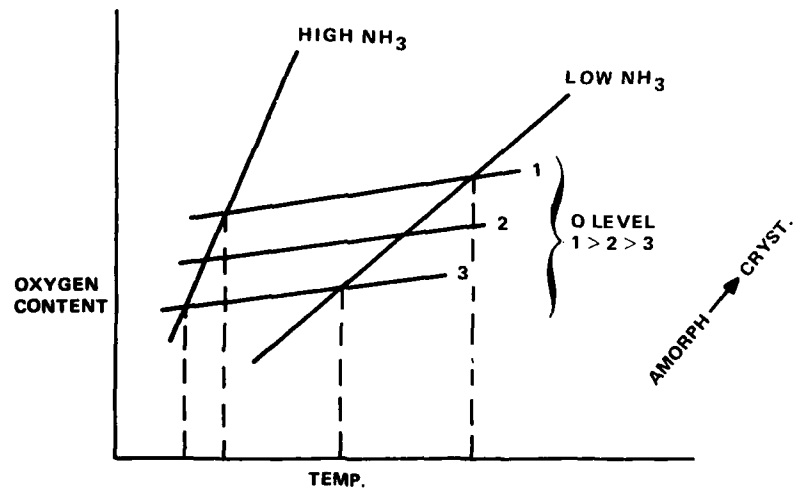


Figure 2-34. Schematic Representation of Effect of Oxygen Impurities on Formation of Amorphous and Crystalline Deposits at Various Temperatures.

SECTION 3.0
PHYSICAL PROPERTY CHARACTERIZATION

SECTION 3.0

PHYSICAL PROPERTY CHARACTERIZATION

3.1 CHEMICAL PROPERTIES

3.1.1 Phase Identification

X-ray diffraction analyses (Ref. 3-1) show that crystalline deposits are alpha silicon nitride with varying degrees of preferred orientation both within (i.e., first versus last deposited surface) and between deposits (deposition conditions alter growth morphology). Quantification of the degree of preferred orientation has not been attempted as yet; this will be done during the next contract period as data is gathered regarding the effects of texture on optical, microwave and thermomechanical properties.

During this contract period precision lattice parameters were measured on material from two deposition runs in which extreme color variations were observed: translucent dark brown and translucent frosty white. Previous work by Niihara and Hirai (Ref. 3-2) indicated that white $\alpha\text{-Si}_3\text{N}_4$ deposits had higher oxygen contents than darker deposits and that lattice shrinking (and an associated reduced c - spacing) occurred with increasing oxygen contents. The results of precision lattice parameter determinations on this program (described in Appendix A) are summarized in Table 3-1. The data, which is in qualitative agreement with Niihara and Hirai (Ref. 3-2), suggest that a solubility range exists for oxygen in the $\alpha\text{-Si}_3\text{N}_4$ lattice. As originally suggested by Wild et. al. (Ref. 3-3), $\alpha\text{-Si}_3\text{N}_4$ may in fact be an oxynitride (substitutional solid solution) with an appropriate number of nitrogen and silicon vacancies present to maintain electrical neutrality. It could thus be postulated, on the basis of data in Table 3-1 that the observed color variations in $\alpha\text{-Si}_3\text{N}_4$ originate from lattice defects rather than from impurity absorption. It is noteworthy that color variations in AlN have also been attributed to lattice defects originating from variations in oxygen content. Similar to current observations on $\alpha\text{-Si}_3\text{N}_4$, the c-spacing of the AlN lattice decreases with increasing oxygen content up to a solubility limit of approximately 1.7 w/o oxygen (Ref. 3-4).

3.1.2 Phase Purity

Phase purity of a typical deposit was determined by emission spectroscopy, neutron activation analysis and visible observation of ultraviolet light stimulated fluorescence. This data is

summarized in Table 3-2 for a deposit which exhibited a color gradient along its length. Color variations could be interpreted as originating from an oxygen, aluminum or copper gradient. Research in progress strongly suggests that the oxygen impurity content directly contributes to the observed color variations. Thus, the brown form of α -Si₃N₄ represents the purest version synthesized on this program. It is interesting to note that it is precisely this form of α -Si₃N₄ which does not exhibit visible fluorescence when irradiated with monochromatic ultraviolet light ($\lambda = 3360\text{\AA}$).

3.2 ELECTRICAL PROPERTIES

3.2.1 Resistivity

The resistivity of a deposit which exhibited a color gradient along its length (same deposit evaluated in Table 3-2) was determined using the direct current technique from near room temperature to 1400°K. The resistivity data are plotted as a function of temperature and color in Figures 3-1, 3-2 and 3-3. The data show that the room temperature resistivity of α -Si₃N₄ is greater than 10^{14} ohm-cm regardless of color. Analyses of the data in terms of a deduced intrinsic band gap and associated low temperature activation energy indicate that a possible correlation exists with color (and oxygen content) of a deposit, as summarized in Table 3-3. Correlations of this type have been found for amorphous silicon nitride films (Ref. 3-5) where continuous changes in excess silicon and oxygen content were found to result in continuous changes in color and band gap of a deposit.

3.3 ELECTROMAGNETIC PROPERTIES

3.3.1 Visible and Infrared Band Pass

As mentioned previously, at least three colors of α -Si₃N₄ have been observed both within (color gradient along a deposition plate) and between deposits. Figure 3-4 compares the total transmittance (diffuse plus specular) of three α -Si₃N₄ deposits exhibiting distinct color differences. The observed colors agree with expected absorption regions for incident white light (e.g., green appearing material preferentially absorbs the red portion of incident white light).

Analyses of the ultraviolet absorption edges for each specimen, similar to the procedures used by Buaer (Ref. 3-5), provided data for computation of their respective band gaps, as shown in Figure 3-5. A comparison of band gaps calculated from optical data with that determined from temperature - dependent resistivity data are summarized in Table 3-4 as a function of color (and oxygen content).

Figures 3-6 and 3-7 show the specular (in-line) transmittance of amorphous and crystalline silicon nitride. Also, shown in Figure 3-7 (as discrete points) are corresponding total transmittance measurements which indicate the presence of scattering defects in the deposit. Both amorphous and crystallizing Si_3N_4 exhibit similar infrared cut-offs, however, amorphous deposits show an absorption band near 3 microns which is attributed to N-H bonding in the deposit.

Figure 3-8 shows the infrared specular transmittance of $\alpha\text{-Si}_3\text{N}_4$ as a function of temperature up to 607°C. Only a slight shift in the infrared transmittance was found over the temperature range typical for infrared homing tactical missiles. An assessment of the potential for $\alpha\text{-Si}_3\text{N}_4$ as an imaging infrared window will be made on a subsequent planned program utilizing experimental birefringence data in an optical texture model for non-cubic crystals which is being developed on a concurrent DARPA/ONR sponsored study (Ref. 3-6).

3.3.2 Microwave Band Pass

Under an earlier ONR-sponsored program (Ref. 3-1), it was discovered that the CVD form of $\alpha\text{-Si}_3\text{N}_4$ had an order of magnitude lower loss tangent than published hot pressed Si_3N_4 data (room temperature, 10 GHz). Microwave data has been extended to elevated temperature and a range of frequencies under a recently completed AMMRC-sponsored program (Ref. 3-7). Figure 3-9(A) shows this radar property data as a function of temperature and frequency. The dielectric constant shows a slight temperature dependence up to 800°C but no frequency dependence. Conversely, over this same temperature range, the loss tangents exhibit no temperature dependence but a definite frequency dependence (loss tangent increases with increasing frequency). It should be noted (as shown in Figure 3-9(B)) that the CVD form of Si_3N_4 has a slightly lower dielectric constant but a significantly lower loss tangent than hot-pressed Si_3N_4 at a given frequency (24 GHz). It is planned to extend this data up to the vaporization point of Si_3N_4 on subsequent programs.

3.4 MECHANICAL PROPERTIES

3.4.1 Summary

On the current and earlier program (Ref. 3-1) flexure properties of five different depositions were determined on a total of forty-one specimens using both three- and four-point loading. Flexure data was analyzed using Weibull statistics when warranted (specimen quantities of 10 or more). Four-point bend data was translated to a three-point basis using the method of Davies (Ref. 3-8), as given by Equation (1) below:

$$\frac{\sigma_{\text{3-point}}}{\sigma_{\text{4-point}}} = \left(\frac{m+2}{2} \right)^{\frac{1}{m}} \quad (1)$$

where m is the Weibull modulus (indicator of degree of dispersion, the higher the value of " m ", the more consistent is the material)

Equation (1) confirms experimental observations that generally higher strengths are observed in three-point bending since the volume of material subjected to the maximum tensile stress is very much less than that in a four bend specimen.

Tables 3-5 and 3-6 list room temperature flexure strength data on the stronger deposits made both in the hot-wall (HW) and cold-wall (CW) reactors, respectively. As anticipated from microstructural examinations of both types of deposits, similar flexure strengths were obtained ($\bar{\sigma}_{\text{3-HW}} = 229 \text{ MPa}$ vs. $\bar{\sigma}_{\text{3-HW}} = 240 \text{ MPa}$). In comparison, the mean three-point bend strengths for reaction-sintered Si_3N_4 ($\rho = 2.55 \text{ g/cc}$), reported by Evans (Ref. 3-9), was approximately 275 MPa. Thus, it may be concluded that CVD α - Si_3N_4 , at its current stage of development, has mean strength levels comparable to reaction-sintered Si_3N_4 .

Expanded descriptions of mechanical property data (including fracture toughness, hardness, and fractography) on deposits synthesized in both the hot- and cold-wall reactors are given in the following paragraphs.

3.4.2 Mechanical Properties: Hot Wall Reactor (HW-4-200 and - 202)

Figures 3-10 and 3-11 show the flexure stress-strain behavior for ten specimens from two hot-wall reactor experiments (HW-4-200 and - 202) in which statistical data regarding the consistency of CVD α - Si_3N_4 deposits was sought. Tables 3-7 and 3-8 list associated moduli of rupture and elasticity and failure strain for each specimen tested. Figures 3-12

and 3-13 are Weibull plots of the data showing a least-squares fit and corresponding Weibull moduli for each group of specimens. These moduli ($m_{202} = 8.14$, $m_{202} = 13.31$) are not unlike those reported in the literature for reaction-sintered and hot pressed Si_3N_4 (Ref. 3-10).

Figure 3-14 is a three-dimensional picture of a typical microstructure observed in flexure specimens in this hot-wall reactor series. The columnar growth pattern can be seen with an angular offset of about 5° from normal. The surface showing a finer grain size is probably associated with an earlier deposited plane (first deposited surface), however, this orientation relationship was not recorded systematically during this series of flexure measurements.

Figures 3-15 and 3-16 show more extended areas of the top and bottom surfaces of two flexure specimens which exhibited widely different flexure strengths. A comparison of the grain structure of the tension side of each specimen clearly suggested the existence of a strength: grain size correlation. Figure 3-17 is a plot of fracture strength versus the square root of grain size showing the existence of a possible Hall-Petch correlation. Extrapolation of this data to smaller gain sizes typical of hot pressed modifications (1-2 microns) indicates that a strength potential of 1110 MPa (~161 ksi) may be achieved through grain refinement during deposition. Figure 3-18 shows a typical fracture surface in this series being basically a transgranular brittle fracture mechanism. A more extensive discussion on the fractography of CVD α - Si_3N_4 is given below.

Fracture toughness measurements using the Evans/Charles indentation method (Ref. 3-11) were performed on selected flexure specimens representative of the mean and extreme values of each deposition in this series. The indentation method was calibrated in our laboratory using hot-pressed Si_3N_4 (NC-132) as a standard. Tables 3-9 and 3-10 are computerized displays of typical identification data taken on hot-pressed and CVD prepared Si_3N_4 . Vickers diamond pyramid data is displayed at the bottom of each table and serves to identify the load-independent hardness regime within which valid data is obtained. Four sets of crack extension data are obtained for each ident. This data together with respective averages and standard deviations are displayed in appropriately designated columns in each table. The fracture toughness obtained on hot-pressed silicon nitride (NC-132) is typical of that reported in the literature (Ref. 3-12). Additional fracture toughness data on four additional specimens in this series are compiled in Appendix B. Analyses of fracture toughness data from deposit HW-4-202 indicated a possible correlation between strength and toughness as summarized

in Table 3-11. Also, an estimate of the critical flaw size responsible for failure was made using the method of Bansal (Ref. 3-13) as shown by Equation (2) below:

$$\sigma_f = K_{IC}/s \quad (2)$$

where $s = Y \sqrt{a/z}$

$Y = 2.0$ for crack extension from a surface

$Z = \pi/2$ for a semicircular crack

The critical flaw size estimated for Specimen HW-4-200-4 was 39 microns which correlates with observed microcrack networks typical of hot-wall depositions. (See microstructures in Figures 3-14, 3-15 and 3-16). Elimination or reduction in the size of these defects would lead to significant strength improvements.

Characterization of the fracture surfaces of the CVD $\alpha\text{-Si}_3\text{N}_4$ flexure bars in this series was attempted using both optical and scanning electron microscopy (SEM).

The initial evaluation resulted in the optical fractographs shown in Figures 3-19 and 3-20. Evidence of cleavage steps and cleavage step propagation is presented in Figure 3-19 for the situations of the fracture path propagating across a twist boundary and across a tilt boundary. A boundary is defined as a grain boundary or sub-grain boundary. Figure 3-20(A) illustrates a group of intersecting parallel line features identified as Wallner lines; river patterns are noted in Figure 3-20(B). All of these cleavage features indicate the presence of an operative slip system at room temperature as suggested by recent hardness anisotropy evaluations. (Ref. 3-14)

Examples of SEM fractographs are presented in Figures 3-18, 3-21 and 3-22. Cleavage is the dominant fracture mode with a minor fraction possibly attributable to grain boundary decohesion. The dominant fracture path is transgranular and the mixed fracture appearance is due to imperfections (microcracks) and changes in crystal orientation. Crack initiation sites were not identified due to the multiplicity of surface microcracks and the single crystal nature of the ceramic body. The presence of critical-sized microcracks at the surface (and internally) with the grain structure of single crystal columnar grains resulted in the lack of definition of a singular crack origin for these specimens.

3.4.3 Mechanical Properties: Hot Wall Reactor (HW-4-139)

The effects of color and temperature on the strength of CVD α - Si_3N_4 was explored on a single deposit which exhibited a color gradient along its length. Two distinctly colored regions were identified (green, brown) from which sufficient material was available for fabricating flexure specimens. Table 3-12 summarizes the (4-point) flexure properties obtained at three temperatures. Actual flexure stress-strain data in this series are given in Appendix C. Figure 3-23 graphically illustrates the flexure strength as a function of temperature and color. In general brown colored material was found to be stronger than green colored material. Figures 3-24 and 3-25 show polished (A) and etched (B)* cross-sections of respective flexure specimens. A finer columnar grain structure was found for the brown material. Also, as previously, the oxygen content varies as a function of deposit color being least for brown deposits. Additional evidence which correlates with strength variations are the fracture surfaces for brown and green material shown in Figures 3-26 and 3-27. The brown deposits consistently exhibit a transgranular cleavage mode (compare Figure 3-26 with Figures 3-18 and 3-21). In contrast, green deposits (and also white deposits) exhibit intergranular cleavage fracture characteristics, as shown in Figure 3-27. Similar to reaction sintered Si_3N_4 (Ref. 3-10), CVD α - Si_3N_4 exhibits slight decreases in strength at elevated temperatures in contrast to the rapid decrease in strength of hot-pressed modifications which utilize densification additives to achieve near theoretical densities. For example, at 1400°C, CVD α - Si_3N_4 deposits retain 76 percent of their room temperature strength compared to only 33 percent for hot-pressed Si_3N_4 (Ref. 3-10). This strength retention characteristic of CVD α - Si_3N_4 is important both in weapon system as well as commercial structural ceramic applications where supplemental mechanical or dynamic loading may be imposed in addition to thermal stress loading.

3.4.4 Mechanical Properties: Cold Wall Reactor (CW)

A total of eighteen three point flexure specimens from ten cold wall reactor experiments were tested to determine if the current series of experiments developed microstructures leading to improved mechanical properties. Table 3-13 summarizes the flexure strength data

*Appendix D details the results of study to develop suitable etchants for CVD α - Si_3N_4 .

including some visual observations regarding morphology and associated deposition rates. Deposits which exhibited a layered structure were considerably weaker than the more typical homogeneous deposits. Both homogeneous brown and green colored deposits exhibited strength levels comparable to hot wall reactor deposits. However the cold-wall reactor deposition rates are significantly higher than those obtained in the hot wall reactor (factor of four).

Figures 3-28, 3-29, 3-30 and 3-31 are photomicrographs of CW 19 and CW 30 flexure bars showing fracture surfaces and last deposited surfaces. The fracture morphology is not unlike hot wall fracture surface details. Figures 3-32 and 3-33 show the fracture surface and last deposited surface for a cold-wall deposition exhibiting the banding phenomenon. (Run No. CW-32). Banded deposits exhibited an order of magnitude lower strength level than the more typical homogeneous deposits. Although the strength levels of Run No. CW-44 were low (but greater than banded deposits in this series) its non-columnar deposition morphology (shown in Figure 3-34) indicated radically different growth kinetics of the type being sought for developing a more equiaxed grain structure. It may be significant that a different silicon precursor (HSiCl_3) was used in this experiment.

3.5 THERMAL PROPERTIES

3.5.1 Thermal Expansion

Table 3-14 compares dilatometric thermal expansion of CVD α - Si_3N_4 with that determined from temperature-dependent lattice parameter data. Good agreement between both test methods was observed.

3.5.2 Thermal Diffusivity

Table 3-15 compares the thermal diffusivity of CVD α - Si_3N_4 with that of other modifications. The brown form of CVD α - Si_3N_4 (least oxygen impurity) exhibits the highest thermal diffusivity of the various deposits evaluated including commercially available reaction sintered and hot pressed Si_3N_4 . The CVD data shown in Table 3-15 is in general agreement with the recent findings of Hirai (Ref. 3-16).

TABLE 3-1. SUMMARY OF CRYSTAL LATTICE PARAMETERS FOR α -Si₃N₄
AS A FUNCTION OF COLOR AND OXYGEN CONTENT

Sample	Color	Oxygen Content*	$\frac{a}{\text{\AA}}$	$\frac{c}{\text{\AA}}$	$\frac{V}{\text{\AA}^3}$
HW-4-128	Dark Brown	0.37	7.7646	5.6219	293.53
HW-4-129	Frosty White	1.07	7.7562	5.6179	292.69

*Neutron Activation Analysis

**Cell Volume, $V = a^2 c \sin 120^\circ$

TABLE 3-2. CORRELATION OF PHASE PURITY OF $\alpha\text{-Si}_3\text{N}_4$ WITH TRACE METALLIC IMPURITIES,
OXYGEN CONTENT AND DEGREE AND COLOR OF FLUORESCENCE

SPECIMEN DESIGNATION	HW-4-139-W1	HW-4-139-G1	HW-4-139-B5
VISUAL COLOR	White	Green	Brown
O ₂ Content*, w/o	1.40	0.92	0.40
Trace Impurities (Emission Spec.)			
ppm Mg	60	20	80
ppm Fe	300	180	380
ppm Al	60	40	30
ppm Cu	20	10	ND
Fluorescence to 3360 Å			
Visually Observed	Yes	Yes	No
Color of Fluorescence	Pink	Yellow-green	Not observed
*Neutron Activation Analysis			

TABLE 3-3. INTRINSIC BAND GAP AND ACTIVATION ENERGY AS A FUNCTION
OF DEPOSIT COLOR (AND OXYGEN CONTENT)

SPECIMEN DESIGNATION	HW-4-139W1	HW-4-139G1	HW-4-139B5
Visual Color	White	Green	Brown
Oxygen Content (w/o)	1.40	0.92	0.40
Band Gap (Eg)	4.9 eV (> 1250°K)	4.7 eV (> 1050°K)	4.3 eV (> 1250°K)
Activation Energy (E _a)	0.83 eV (588-1053°K)	0.96 eV (650-950°K)	1.12 eV (688-870°K)

TABLE 3-4. COMPARISON OF BAND GAP DATA DEDUCED FROM OPTICAL AND RESISTIVITY MEASUREMENTS AS A FUNCTION OF COLOR AND OXYGEN CONTENT

SPEC.	DESIGNATION	OXYGEN CONTENT (w/o)	OPTICAL ABSORPTION	BAND GAP (eV)	RESISTIVITY
HW-4-139	W1	1.40		5.0	4.9
HW-4-139	G1	0.92		4.4	4.7
HW-4-139	B5	0.40		4.0	4.3

TABLE 3-5. SUMMARY OF ROOM TEMPERATURE FLEXURE STRENGTH DATA ON α -Si₃N₄
PREPARED IN THE HOT-WALL REACTOR

RUN NO.	NO. OF SPEC.	LOADING	MEAN STRENGTH MPa (kpsi)	WEIBULL "m"	3-POINT (Eq. 1) MPa (kpsi)	COLOR OF DEPOSIT
HW-4-128 (B)	4	4 pt.	218.16 (31.64)	10.73*	259.17 (37.59)	Brown **
HW-4-129 (W)	5	4 pt.	60.23 (8.74)	"	71.55 (10.38)	White
HW-4-139 (B)	2	4 pt.	159.41 (23.12)	"	189.38 (27.47)	Brown **
HW-4-139 (G)	1	4 pt.	120.52 (17.48)	"	143.18 (20.77)	Green
HW-4-200 (B)	10	3 pt.	242.76 (35.21)	8.14	-	Brown **
HW-4-202 (B)	10	3 pt.	223.11 (32.36)	13.31	-	Brown **

*Av. of m_{200} and $m_{202} = 10.73$

$\bar{C}_{3-HN} = \frac{\text{** Av. 3 pt. Strength}}{\text{of Brown Material}}$ = 228.63 MPa (33.16 kpsi)

TABLE 3-6. SUMMARY OF ROOM-TEMPERATURE FLEXURE STRENGTH DATA ON α - Si_3N_4
PREPARED IN THE COLD-WALL REACTOR

RUN NO.	NO. OF SPEC.	LOADING	MEAN STRENGTH MPa (kpsi)	NETBULL "m"	3-POINT (EQ. 1) MPa (kpsi)	COLOR OF DEPOSIT
CW-16	1	3 pt	219.74	-	-	Brown
CW-19	2	3 pt	234.08	-	-	Brown
CW-30	2	3 pt	260.90	-	-	Brown
CW-35	2	3 pt	263.31	-	-	Green
CW-36	2	3 pt	223.94	-	-	Green

$$\overline{\sigma}_{3-\text{HW}} = \text{AV. 3 pt STRENGTH} = 240.39 \text{ (34.87 kpsi)}$$

TABLE 3-7. FLEXURE PROPERTIES OF DEPOSIT HW-4-200.

Specimen No.	Flex. Strength		Failure Strain		Modulus	
	MPa	(kpsi)	(%)		GPa	(Mpsi)
HW-4-200-	239.73	(34.77)	0.06		394.52	(57.22)
	297.09	(43.09)	0.08		384.38	(55.75)
	275.38	(39.94)	0.07		389.48	(56.49)
	259.17	(37.59)	0.07		367.97	(53.37)
	263.38	(38.28)	0.07		377.28	(54.72)
	266.07	(38.59)	0.07		362.53	(52.58)
	211.81	(30.72)	0.06		339.43	(49.23)
	194.64	(28.23)	0.05		466.17	(58.91)
	206.43	(29.94)	0.05		468.91	(60.01)
	214.22	(31.07)	0.06		356.67	(51.73)
	Mean	242.76	(35.21)*	0.07	379.21	(55.00)
	Standard Deviation	34.40	(4.99)	0.01	23.10	(3.35)
*Weibull Modulus = 8.14						

TABLE 3-8. FLEXURE PROPERTIES OF DEPOSIT HW-4-202

Specimen No.	Flex. Strength		Failure Strain		Modulus	
	MPa	(kpsi)	(%)		GPa	(Mpsi)
HW-4-202-	188.78	(27.38)	0.05		394.45	(57.21)
	256.42	(37.19)	0.06		406.17	(58.91)
	220.36	(31.96)	0.06		365.90	(53.07)
	232.28	(33.69)	0.06		368.32	(53.42)
	219.25	(31.80)	0.05		406.86	(59.01)
	218.49	(31.69)	0.05		479.32	(69.52)
	211.19	(30.63)	0.06		364.73	(52.90)
	249.73	(36.22)	0.07		365.35	(52.99)
	213.94	(31.03)	0.06		358.80	(52.04)
	220.42	(31.97)	0.06		384.66	(55.79)
Mean	223.11 (32.36)*		0.06		389.48	(56.49)
	Standard Deviation		19.31 (2.80)		36.27	(5.26)
*Weibull Modulus = 13.31						

TABLE 3-9. FRACTURE TOUGHNESS BY INDENTATION FOR HOT PRESSED
 Si_3N_4 (NC-132).

Indent	Indentation Load (kg)	Hardness		$K_c (\text{MN/m}^{1.5})$					
		kg/mm^2	GN/m^2	1	2	3	4	Avg	Std
1	0.20	1739.	17.06	0.00	0.00	0.00	0.00	0.00	0.00
2	0.50	1674.	15.43	0.00	0.00	0.00	0.00	0.00	0.00
3	1.00	1619.	15.00	0.00	0.00	0.00	0.00	0.00	0.00
4	1.50	1782.	16.70	5.04	4.59	0.00	5.40	5.01	0.41
5	1.50	1699.	15.76	0.00	0.00	4.66	5.02	4.95	0.10
6	1.50	1587.	15.56	5.02	4.62	4.72	5.31	4.92	0.31
7	2.00	1683.	16.00	0.00	0.00	0.00	0.00	0.00	0.00
8	2.00	1599.	15.68	4.90	5.03	4.96	5.61	5.13	0.32
9	2.00	1750.	17.17	5.42	5.22	5.62	5.72	5.49	0.22
10	2.50	1713.	16.80	5.56	5.56	5.55	6.01	5.87	0.22

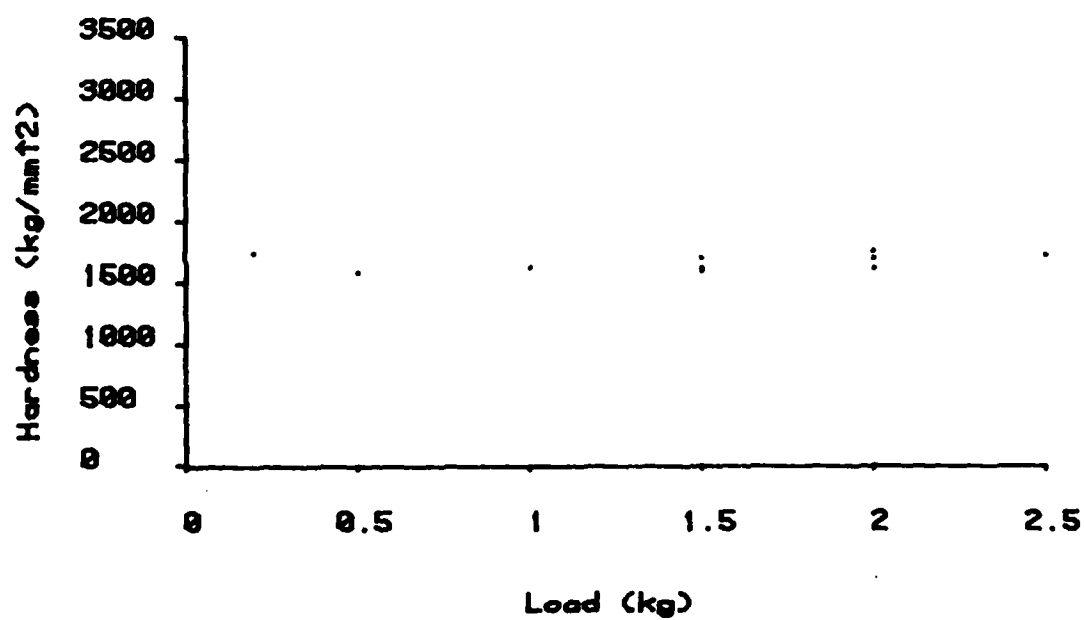


TABLE 3-10. FRACTURE TOUGHNESS BY INDENTATION FOR CVD
 α -Si₃N₄ (SPEC. NO. HW-4-200-4).

Indentation Load (kg)	Hardness kg/sq.mm N/mm ²	K _{Ic} (MN/m ^{3/2})						Avg	S
		1	2	3	4	Avg			
1	0.05	3480.	33.35	0.00	0.00	0.00	0.00	0.00	0.00
2	0.05	3052.	29.93	0.00	0.00	0.00	0.00	0.00	0.00
3	0.05	3986.	36.98	0.00	0.00	0.00	0.00	0.00	0.00
4	0.10	2678.	26.23	2.63	2.31	1.62	3.25	2.45	0.66
5	0.10	2620.	25.68	3.00	2.42	2.42	2.96	2.70	0.32
6	0.10	2879.	26.23	2.73	2.31	2.92	2.53	2.62	0.25
7	0.20	2579.	25.98	2.78	2.58	2.19	3.88	2.82	0.71
8	0.20	2700.	26.57	3.03	2.99	3.06	2.98	2.87	0.92
9	0.20	2383.	29.37	3.05	2.40	1.93	3.53	2.72	0.71
10	0.50	2478.	24.31	3.45	1.81	3.37	1.66	2.57	0.97
11	0.50	2438.	23.83	2.63	2.65	2.47	3.43	2.80	0.43
12	0.50	2608.	25.57	2.73	1.39	2.98	2.73	2.46	0.72
13	1.00	2146.	21.04	3.38	2.95	3.32	0.88	3.22	0.24
14	1.00	2356.	23.12	2.45	2.52	2.38	3.20	2.63	0.38
15	1.00	2326.	22.81	2.44	3.98	2.61	2.58	2.93	0.86
16	1.50	2428.	23.81	2.63	3.47	3.38	3.32	3.18	0.37
17	1.50	2185.	21.42	3.48	2.91	2.94	4.20	3.23	0.60

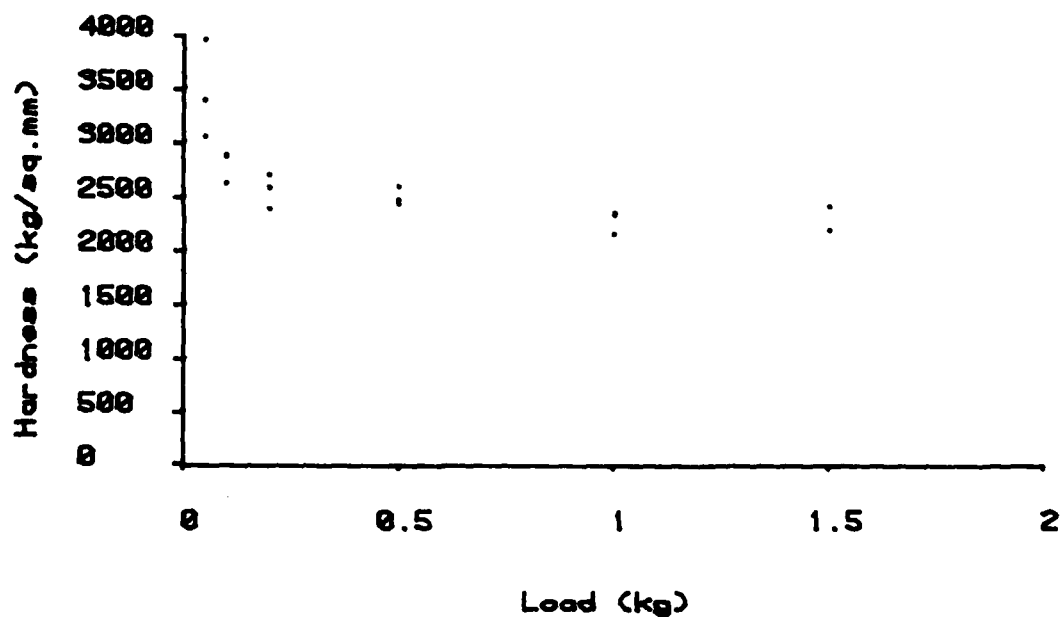


TABLE 3-11. CORRELATION OF FRACTURE TOUGHNESS WITH STRENGTH AND GRAIN-SIZE

SPECIMEN NO.	FLEXURE STRENGTH MPa (kpsi)	FRACTURE TOUGHNESS* (MN m ^{-1.5})	GRAIN SIZE (Mm)	VICKERS HARDNESS* (kg mm ⁻²)
HW-4-202-2	256.42 (37.19)	3.61	16.9	2241
HW-4-202-10	220.42 (31.97)	3.13	23.3	2412
HW-4-202-1	188.78 (27.38)	2.92	33.9	2446

*1 kg indent or load

TABLE 3-12. FLEXURE PROPERTIES OF CVD α -Si₃N₄ AS A FUNCTION OF TEMPERATURE
AND DEPOSIT COLOR (RUN NO. HW-4-139)

SPECIMEN NO.	TEMP. (°C)	FLEXURE STRENGTH* MPa (kpsi)	FAILURE STRAIN (%)	ELASTIC MODULUS GPa (Mpsi)	COLOR
HW-4-139-B3	RT	162.58 (23.58)	0.058	282.82 (41.02)	Brown
HW-4-139-B5	"	156.23 (22.66)	0.061	249.25 (36.15)	Brown
HW-4-139-G3	"	120.52 (17.48)	0.066	187.54 (27.20)	Green
<hr/>					
HW-4-139-B6	1000	109.63 (15.90)	0.040	275.38 (39.94)	Brown
HW-4-139-G4	"	94.46 (13.70)	0.030	334.88 (48.57)	Green
<hr/>					
HW-4-139-B1	1400	118.18 (17.14)	0.040	332.88 (48.28)	Brown
HW-4-139-B2	"	107.21 (15.55)	0.040	247.66 (35.92)	Brown
HW-4-139-G2	"	108.39 (15.72)	0.040	263.72 (38.25)	Green

*4-point loading

TABLE 3-13. FLEXURE STRENGTH OF SELECTED MONOLITHIC COLD-WALL REACTOR DEPOSITS

RUN NO.	FLEXURE STRENGTH MPa (kpsi)	MORPHOLOGY	DEP. RATE (mm hr ⁻¹)
CW14-1	21.10 (3.06)	Banded	1.07
-2	10.07 (1.46)		
CW15-1	18.62 (2.70)	Banded	1.32
-2	28.27 (4.10)		
CW16	219.74 (31.87)	Uniform-Brown	1.67
CW19-1	238.97 (34.66)	Uniform-Brown	1.88
-2	229.11 (33.23)		
CW30-1	267.24 (38.76)	Uniform-Brown	1.09
-2	254.49 (36.91)		
CW31	27.03 (3.92)	Banded	1.17
CW32-1	29.30 (4.25)	Banded	1.44
-2	36.89 (5.35)		
CW35-1	230.42 (33.42)	Uniform-Green	0.84
-2	296.20 (42.96)		
CW36-1	193.88 (28.12)	Uniform-Green	0.99
-2	254.00 (36.84)		
CW44-1	111.28 (16.14)	Uniform-Brown (Laminar)	1.52
-2	107.49 (15.59)		

TABLE 3-14. COMPARISON OF DILATOMETRIC THERMAL EXPANSION BEHAVIOR OF CVD α -Si₃N₄
 (THIS WORK) AND THAT DEDUCED FROM TEMPERATURE-DEPENDENT LATTICE
 PARAMETER DATA (REF 3-15)

Temperature °C	CVD α -Si ₃ N ₄		Lattice Parameter Data on α -Si ₃ N ₄ Fractional Expansion (av.) (cm/cm)
	Thermal Expansion Coeff. (1/°C)	Fractional Expansion (cm/cm)	
30	0.76 x 10 ⁻⁶	0.000139	-
100	1.17 x 10 ⁻⁶	0.000207	0.0002
200	1.73 x 10 ⁻⁶	0.000352	0.0005
300	2.24 x 10 ⁻⁶	0.000551	0.0008
400	2.71 x 10 ⁻⁶	0.000799	0.0010
500	3.13 x 10 ⁻⁶	0.001091	0.0015
600	3.51 x 10 ⁻⁶	0.001424	0.0018
700	3.85 x 10 ⁻⁶	0.001793	0.0023
800	4.15 x 10 ⁻⁶	0.002193	0.0027
900	4.40 x 10 ⁻⁶	0.002621	0.0030
1000	4.61 x 10 ⁻⁶	0.003072	0.0037
1100	4.78 x 10 ⁻⁶	0.003541	-
1200	4.90 x 10 ⁻⁶	0.004025	-

TABLE 3-15. COMPARISON OF THERMAL DIFFUSIVITY (CM²/SEC) OF
REACTION-BONDED, HOT-PRESSED AND CVD α -Si₃N₄

Temp (°C)	NC-132	NC-350	HW-4-139			HW-4-166
	HPSN	RSSN	Brown	Green	White	Brown
312	0.070	0.043	0.085	0.067	0.052	0.110
830	0.040	0.023	0.041	0.035	0.029	0.050
1290	0.032	0.019	n.m	n.m	n.m	n.m

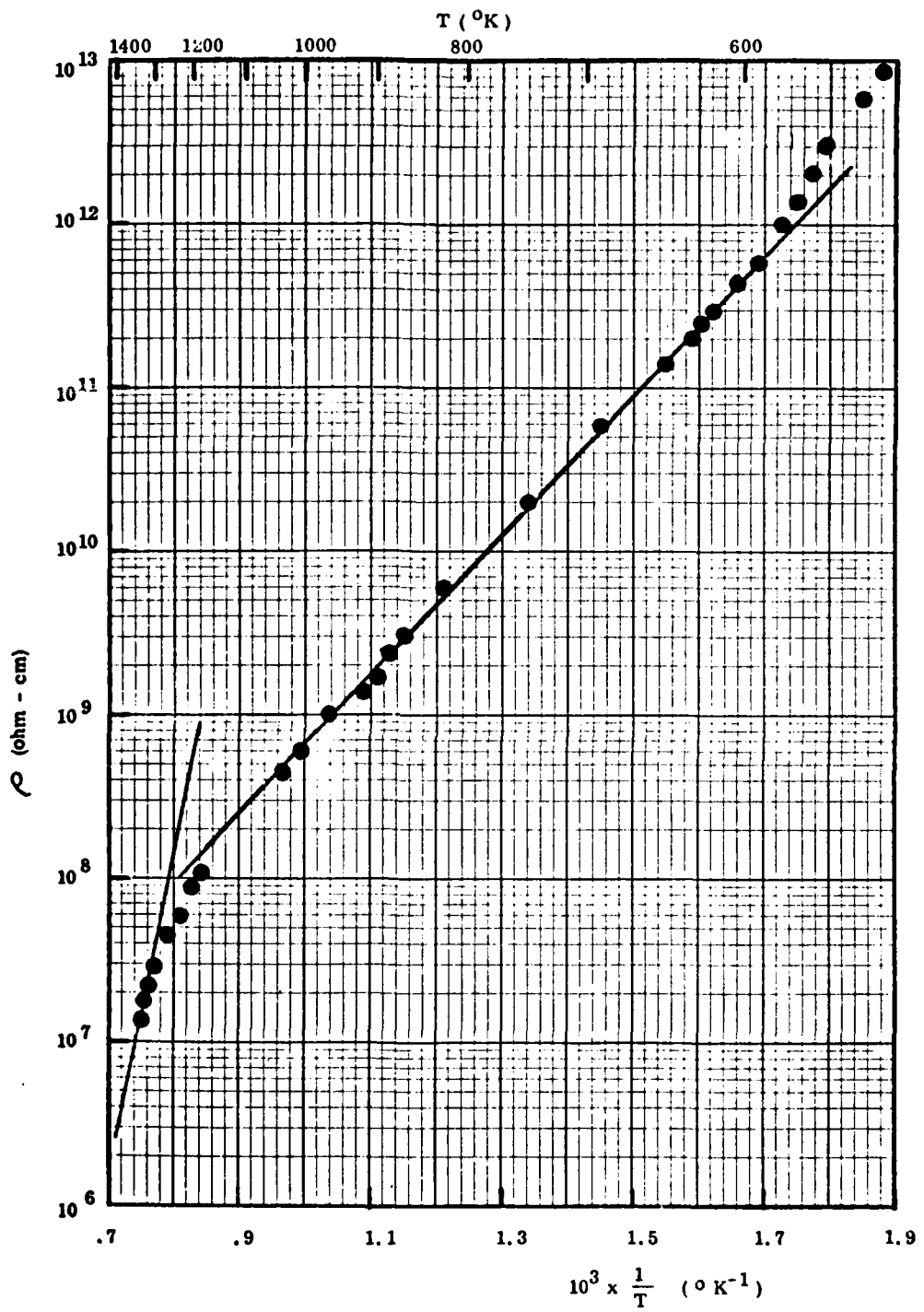


Figure 3-1. Resistivity of White Silicon Nitride (Spec. No. 139-W1) as a Function of $1/T$ between 1366°K and 526°K. From the slope of the curve in the intrinsic region above 1250°K, a value of 4.9 eV is determined for the band gap. An activation energy (E) obtained from $\rho \sim \exp(E/RT)$ is 0.83 eV (1053°K - 588°K).

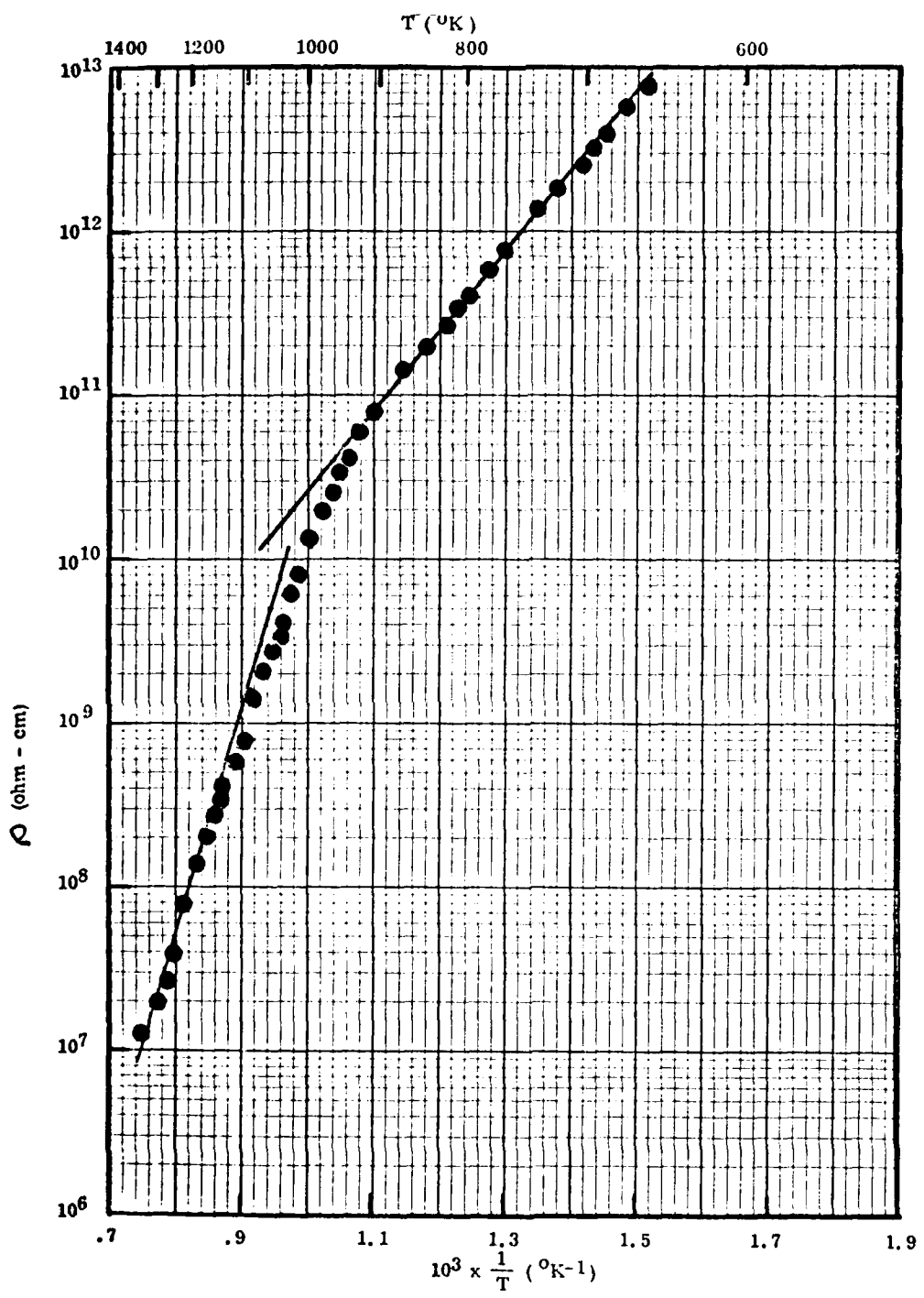


Figure 3-2. Resistivity of Green Silicon Nitride (Spec. No. 139-G1) as a Function of $1/T$. Values of 4.7 eV and 0.96 eV are obtained from the slopes of the curve for the band gap and E respectively.

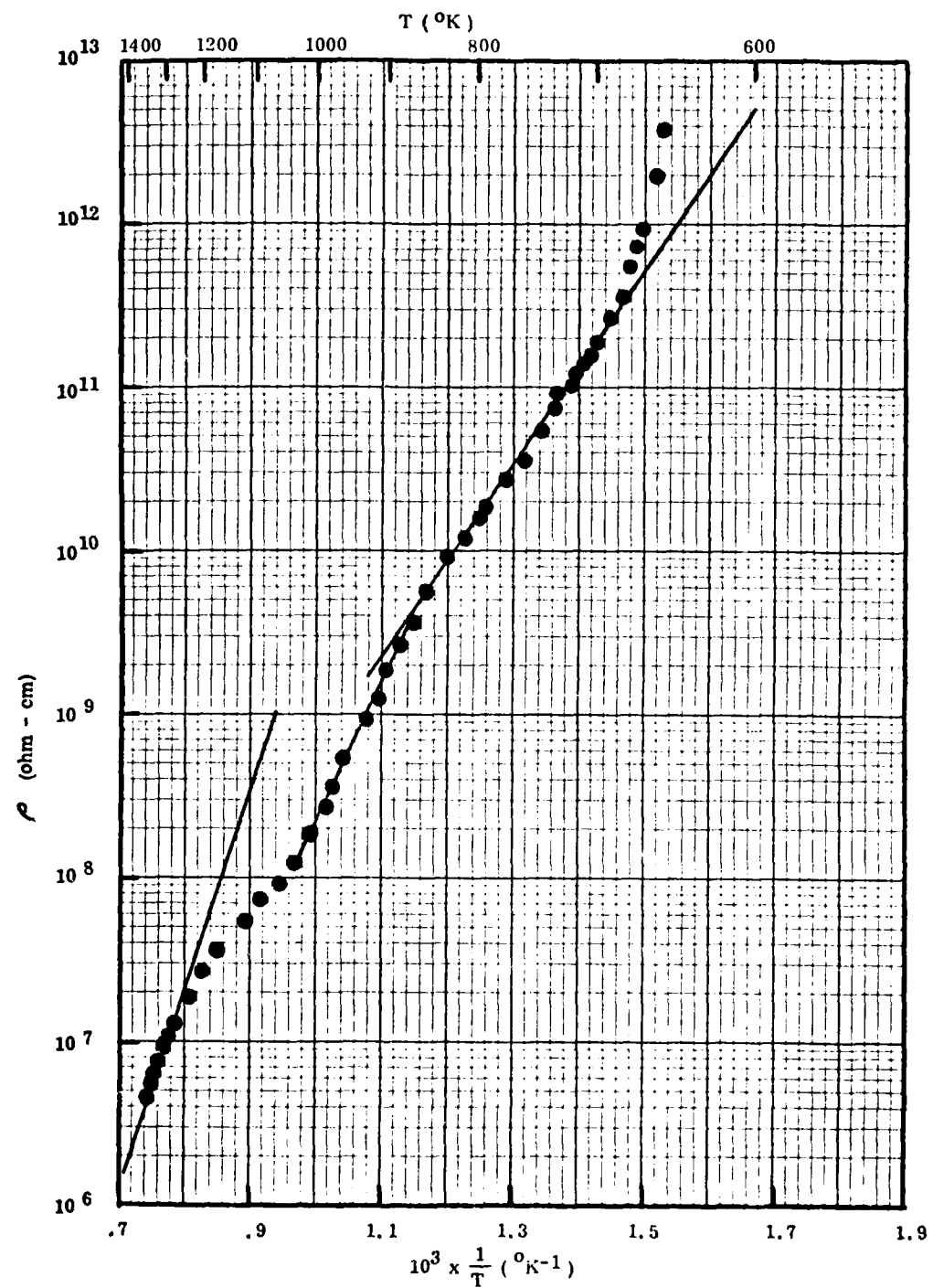


Figure 3-3. Resistivity of Brown Silicon Nitride (Spec. No. 139-B5) as a Function of $1/T$. A Value of 4.3 eV is Determined for the Band Gap. Values for E are 1.12 eV (870°K - 667°K) and 1.53 eV (1053°K - 870°K).

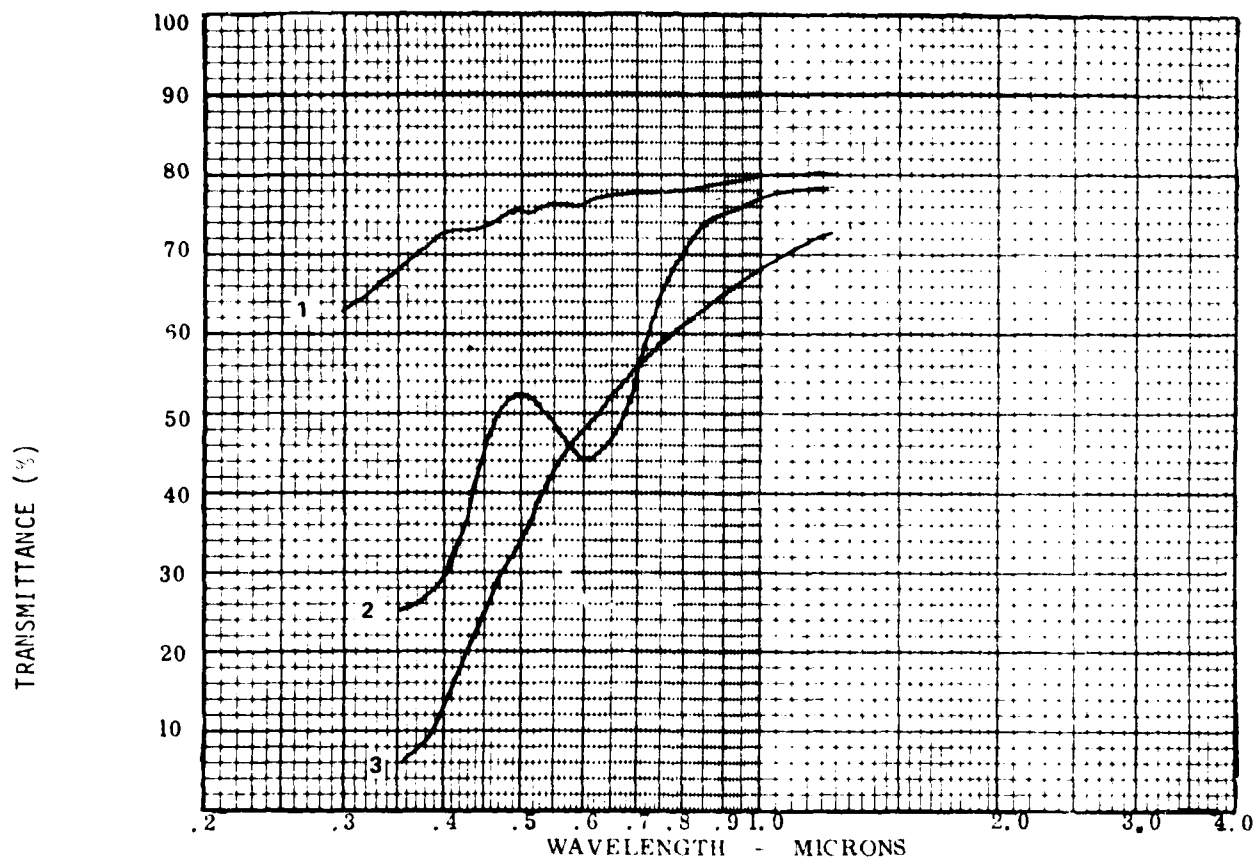


Figure 3-4. Comparison of Total Spectral Transmittance Function (Diffuse Plus Specular) of White (No. 1, $t = 0.188$ mm), Green (No. 2, $t = 0.229$ mm), and Brown (No. 3, $t = 0.241$ mm) Alpha Silicon Nitride.

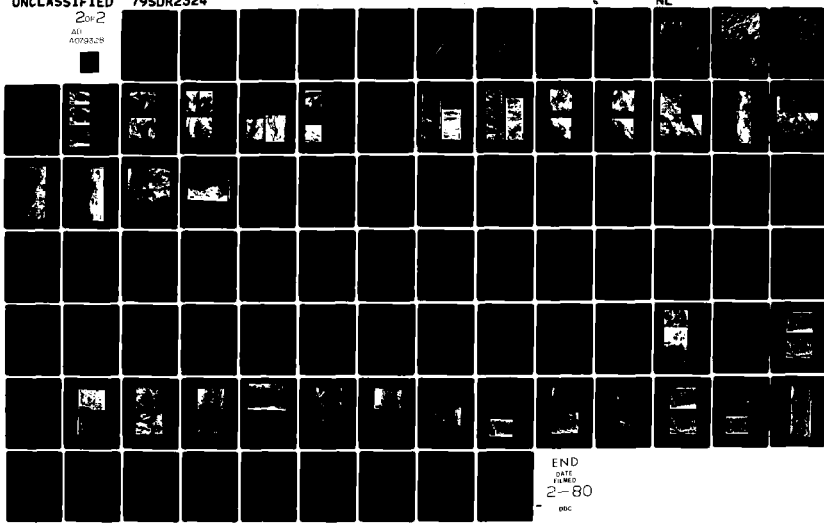
AD-A079 328

UNCLASSIFIED

2 of 2

All rights reserved

GENERAL ELECTRIC CO PHILADELPHIA PA RE-ENTRY AND ENV--ETC F/6 13/8
PROCESSING RESEARCH ON CHEMICALLY VAPOR DEPOSITED SILICON NITRI--ETC(U)
DEC 79 R A TANZILLI, J J GEBHARDT, J D'ANDREA N00014-78-C-0107
79SDR2324 NL



END
DATE
FILED
2-80
DEC

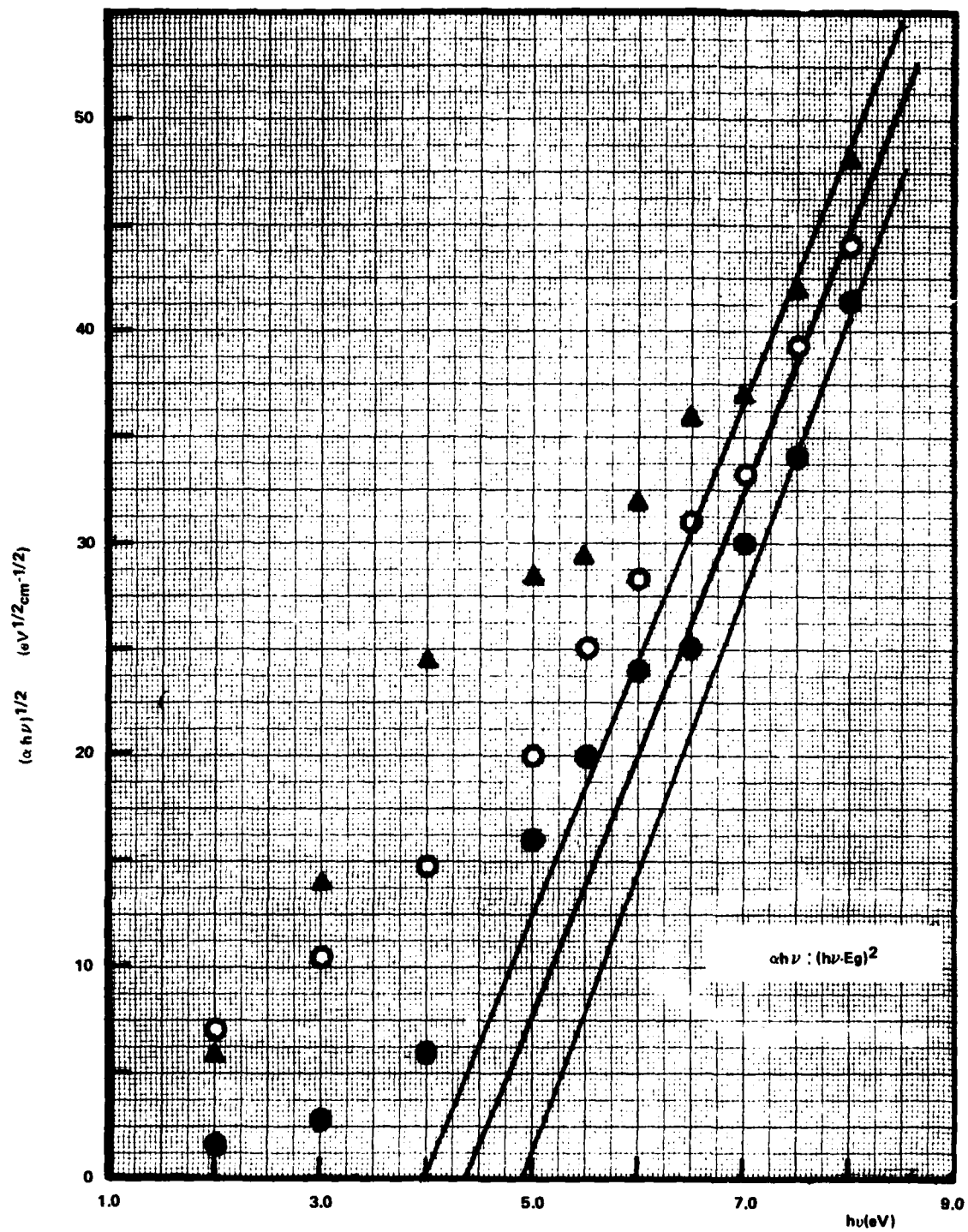


Figure 3-5. Plot of Experimental and Extrapolated $(\alpha h\nu)^{1/2}$ Values Against $h\nu$ for determining E_g . Values of 5.0, 4.4, and 4.0 eVs obtained for the White (●), Green (○), and Brown (▲) Alpha Silicon Nitride.

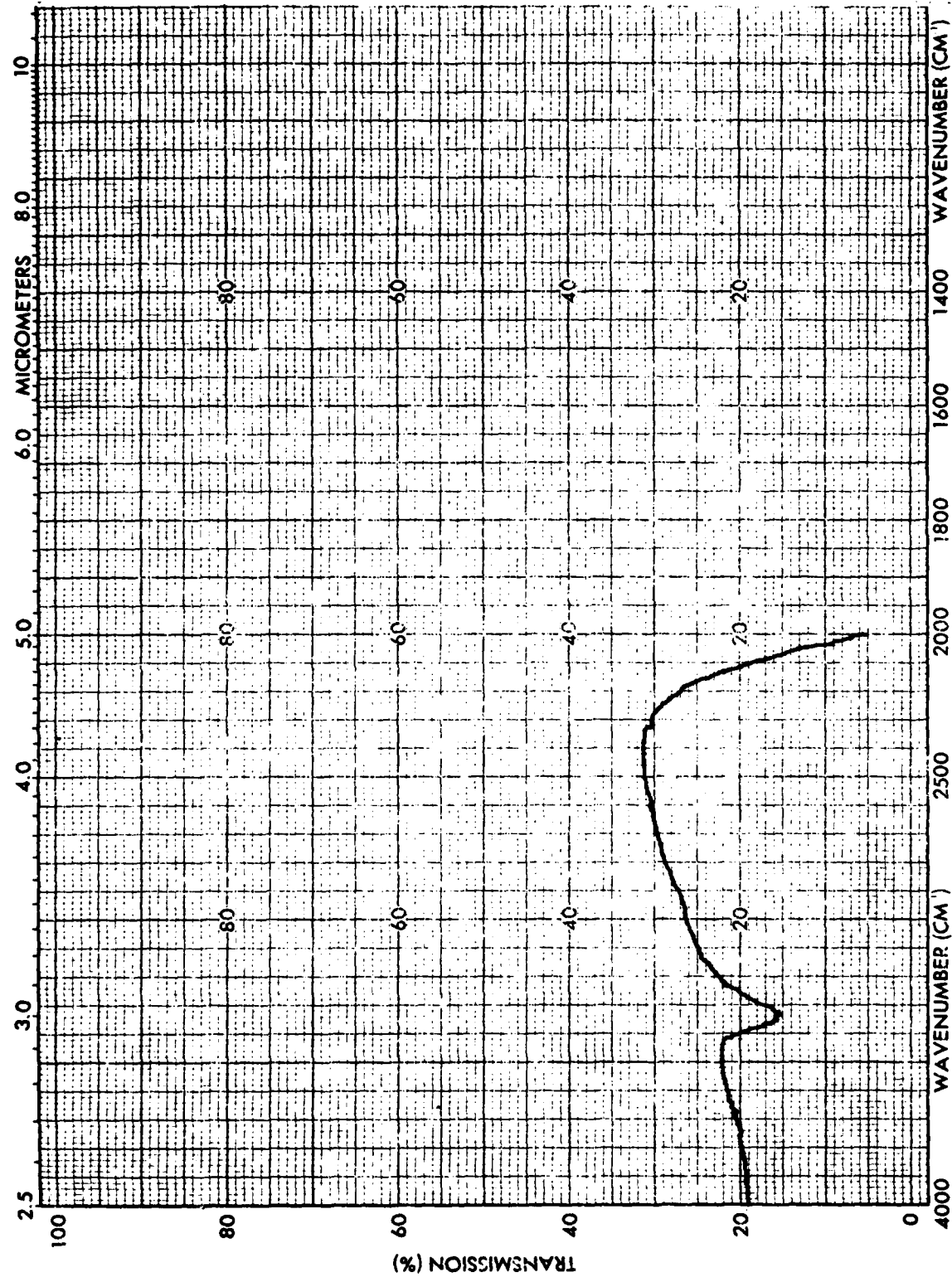


Figure 3-6. Infrared Transmittance of Amorphous Si_3N_4 . Specimen Thickness = 0.254 mm (Run No. HW-4-224).

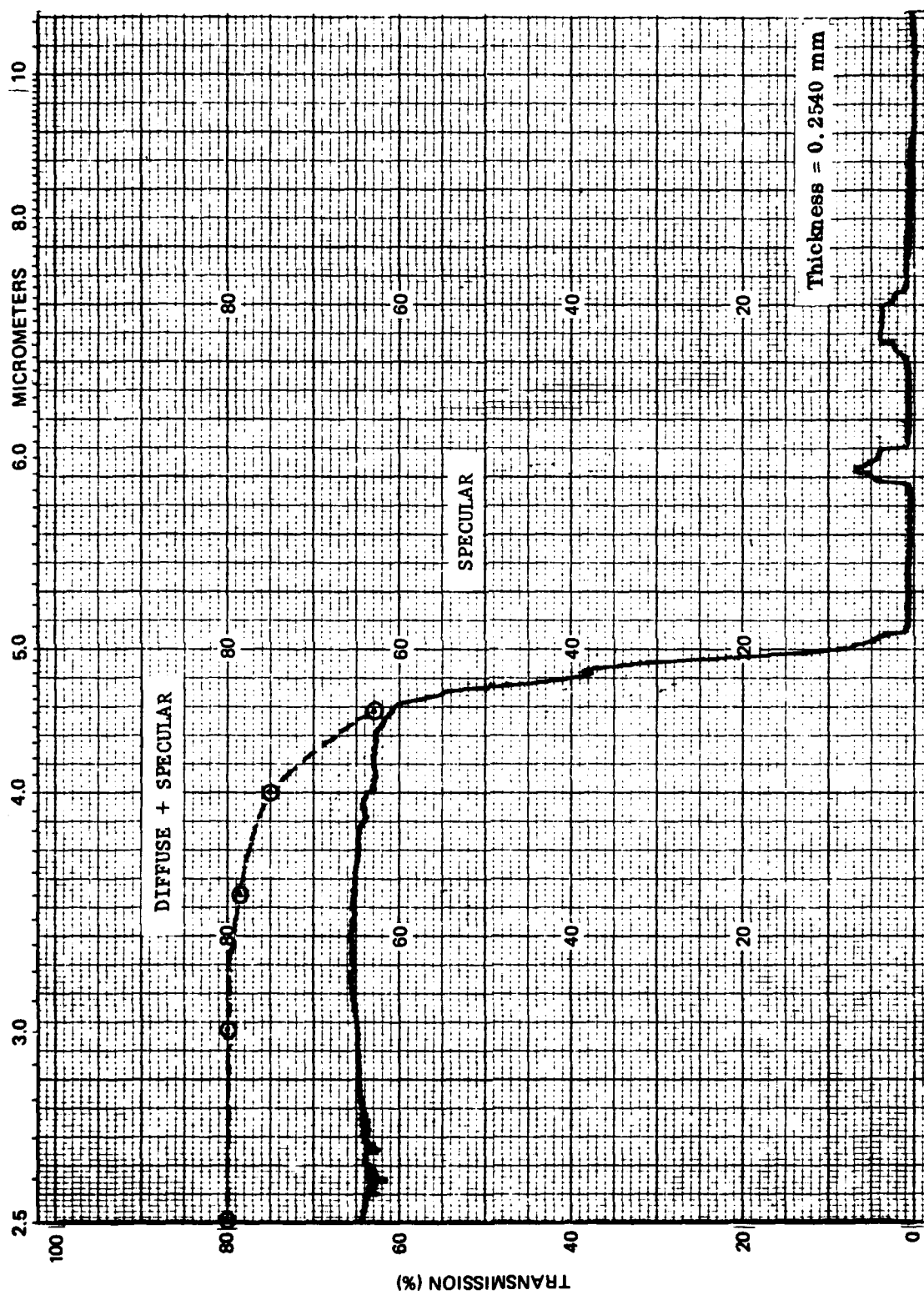


Figure 3-7. Infrared Transmittance of Crystalline α - Si_3N_4 (Run No. HW-4-128).

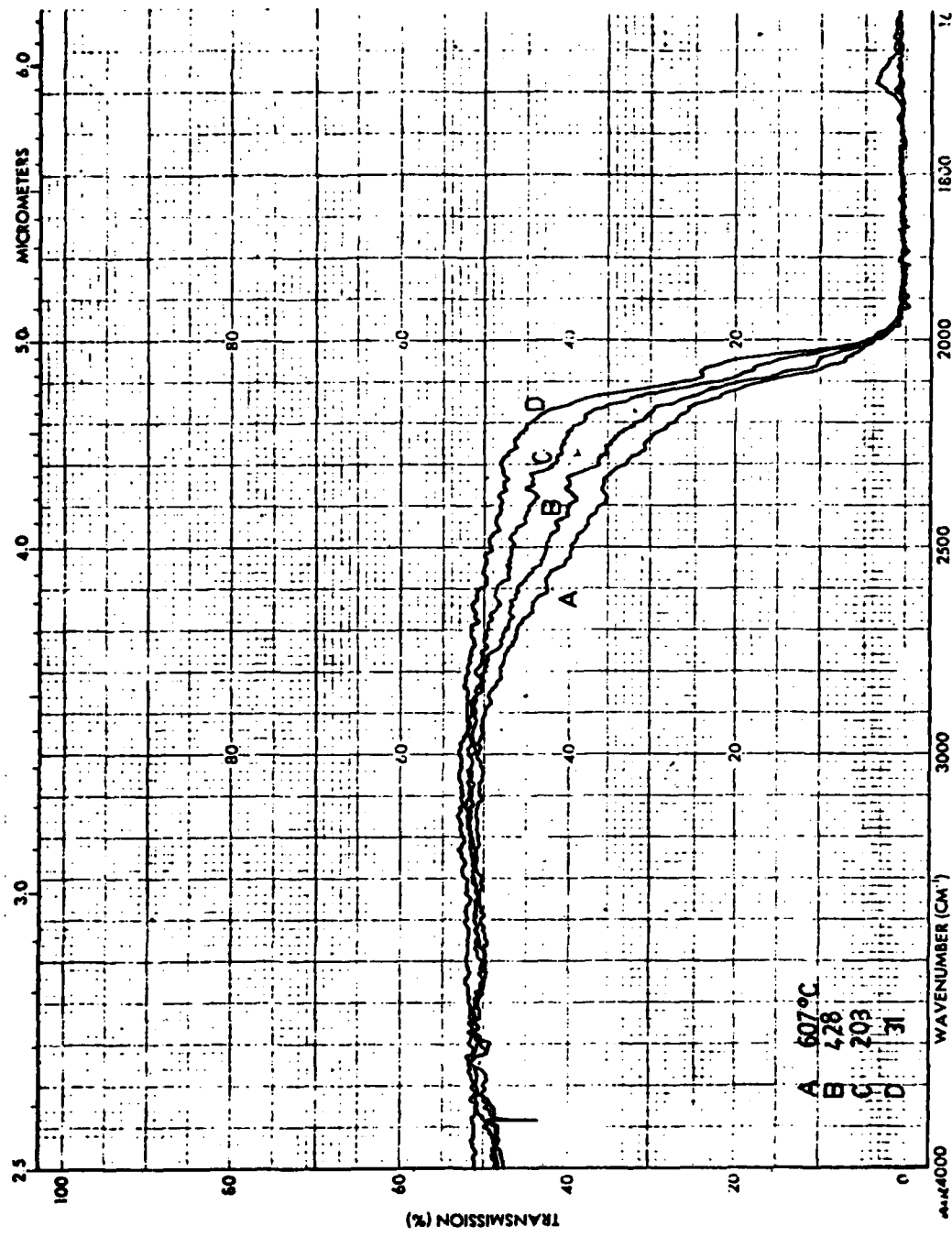


Figure 3-8. Infrared Transmittance of Crystalline α -Si₃N₄ as a Function of Temperature
 (Run No. HW-4-139). Specimen Thickness = 0.361 mm.

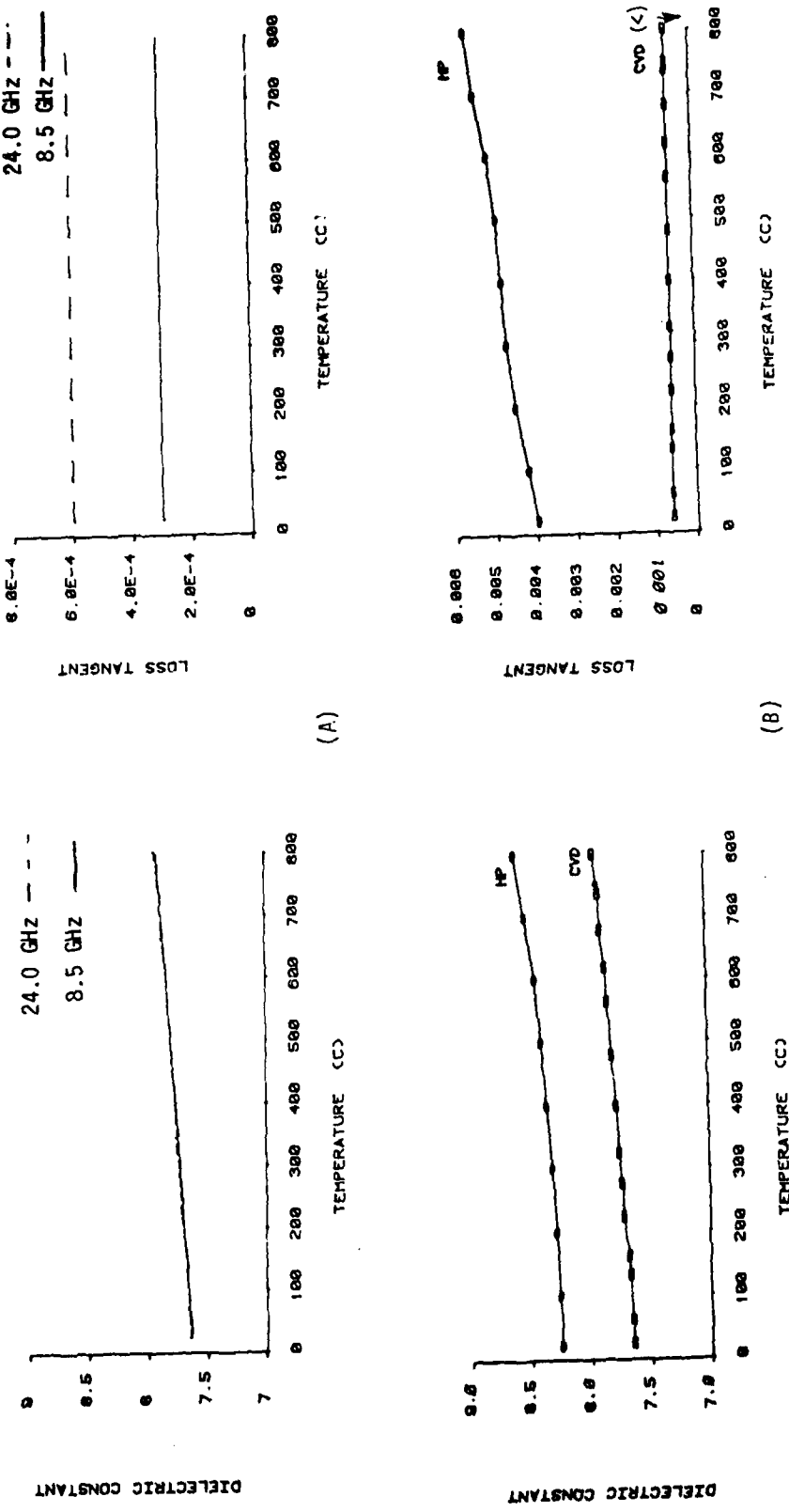


Figure 3-9. Dielectric Properties of CVD α -Si₃N₄ as a Function of Temperature and Frequency (A). Comparison of Radar Properties of CVD Versus HP Silicon Nitride at 24 GHz (B). (REF. 3-7)

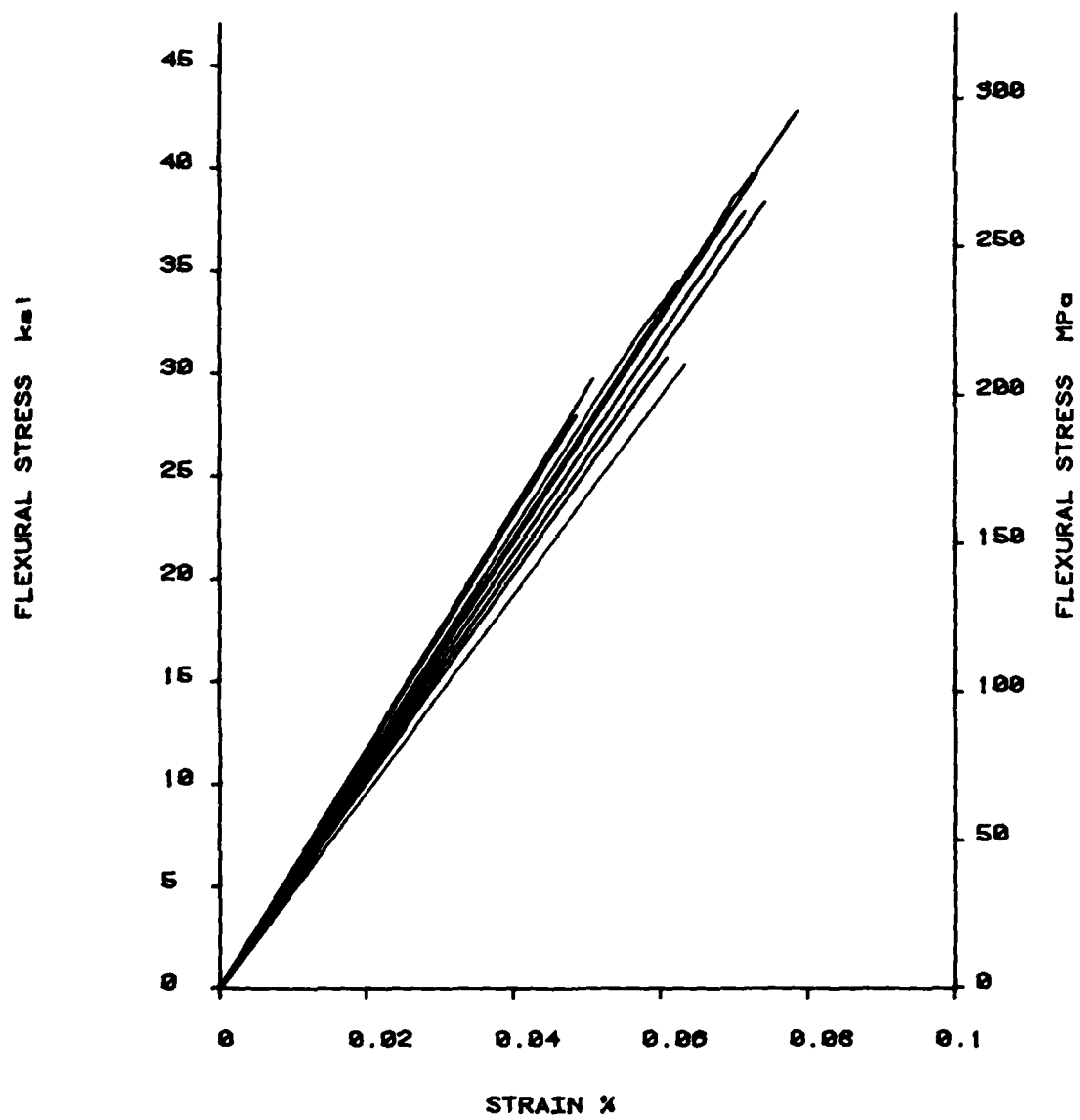


Figure 3-10. Flexure Stress-Strain Behavior of Several Specimens from Deposition HW-4-200. Average MOR = 242.76 MPa (35.21 kpsi), Average Fracture Strain = 0.07%, Average Elastic Modulus = 379.21 GPa (55.00 Mpsi).

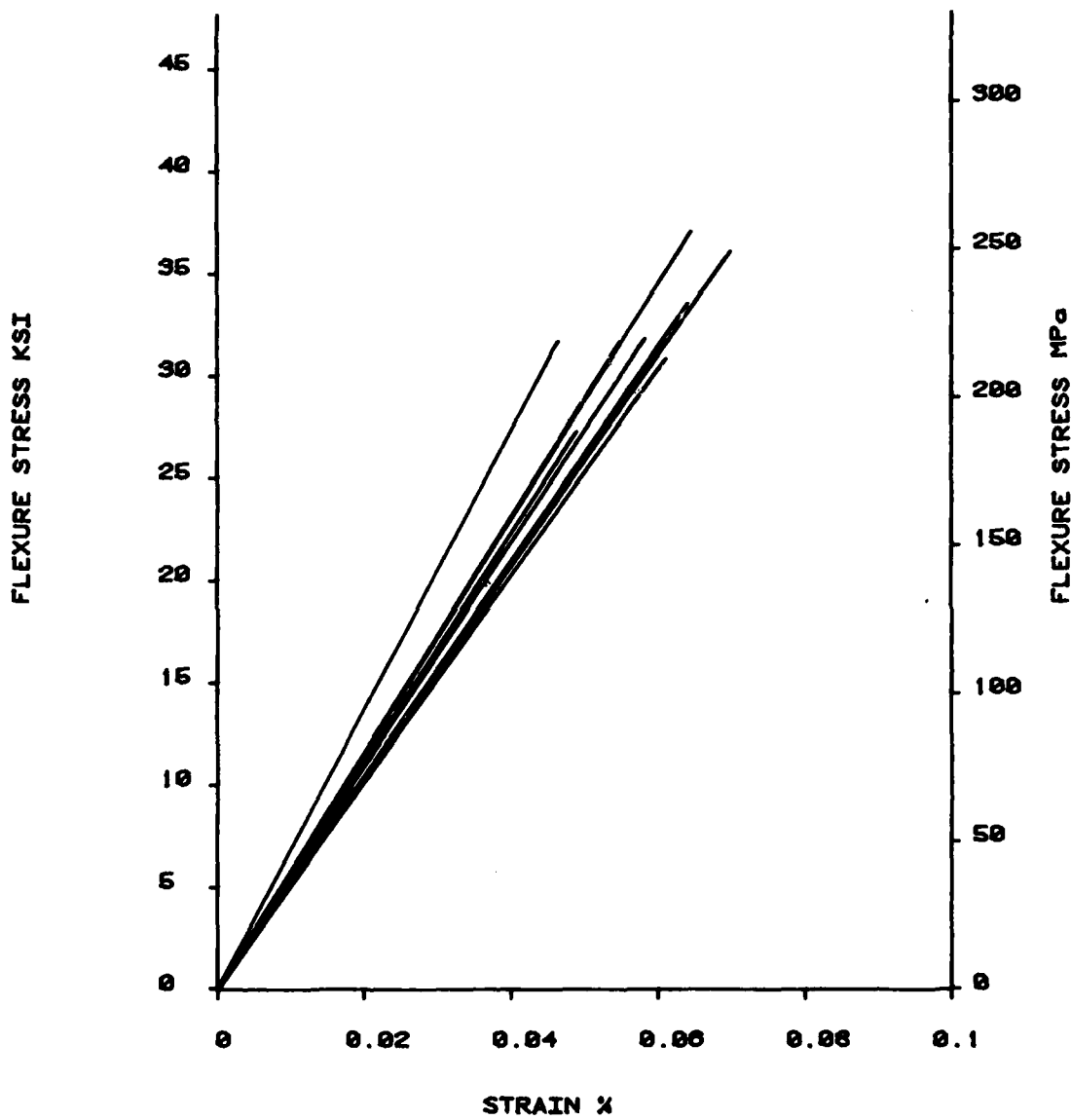


Figure 3-11. Flexure Stress-Strain Behavior of Several Specimens from Deposition HW-4-202. Average MOR = 223.11 MPa (32.36 kpsi), Average Fracture Strain = 0.06%, Average Elastic Modulus = 389.48 GPa (56.49 Mpsi).

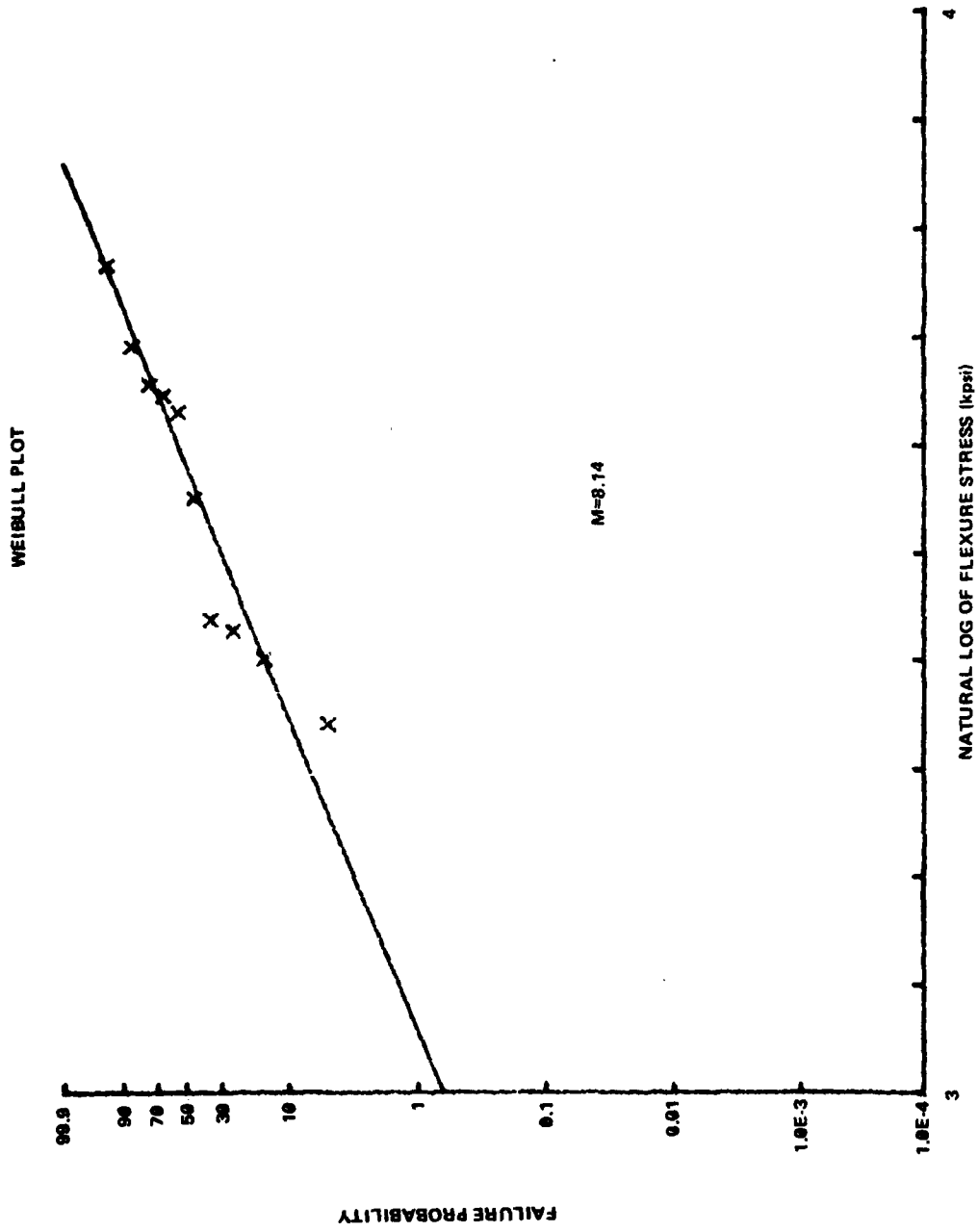


Figure 3-12. Weibull Plot of Flexure Data from Deposit HW-4-200

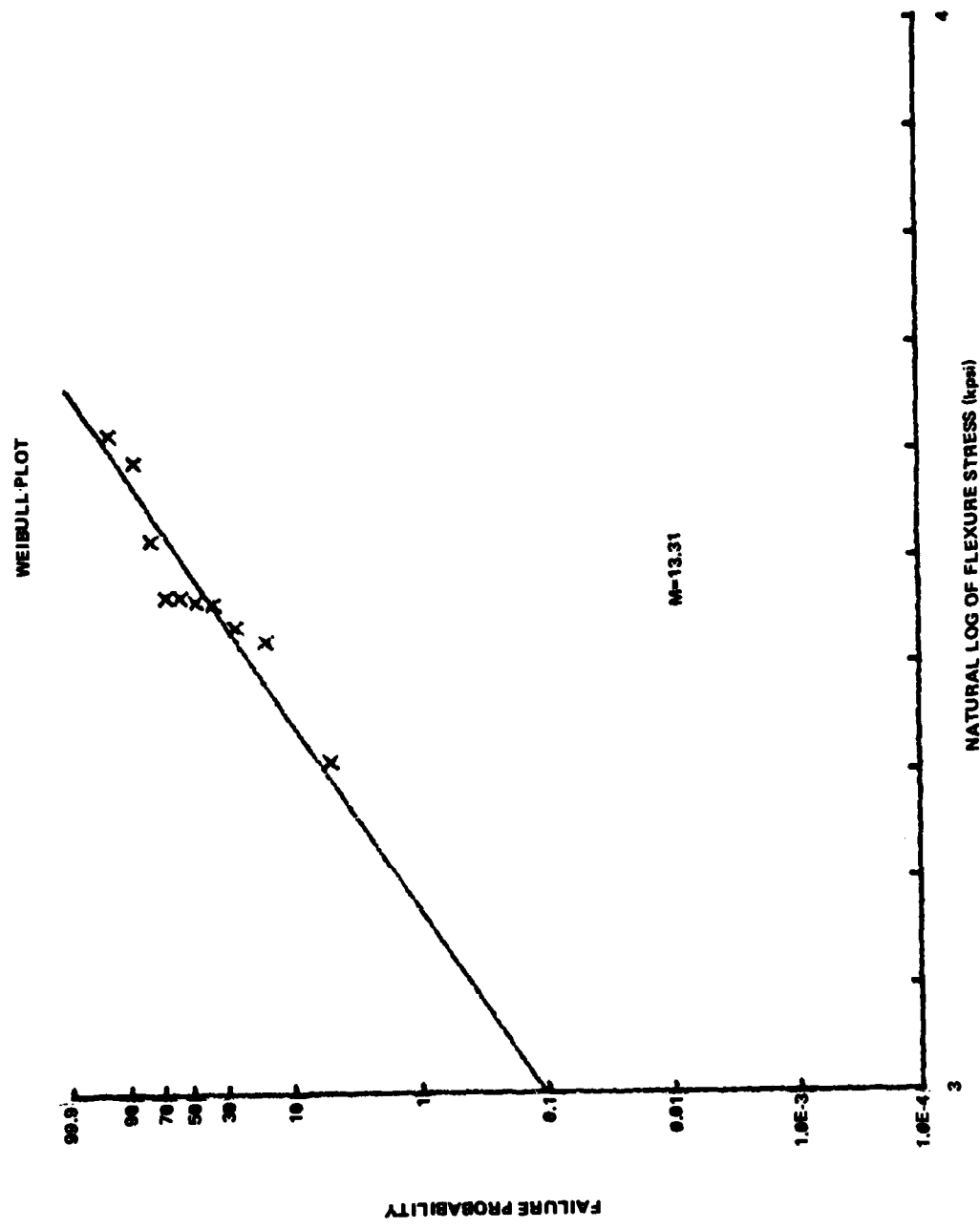
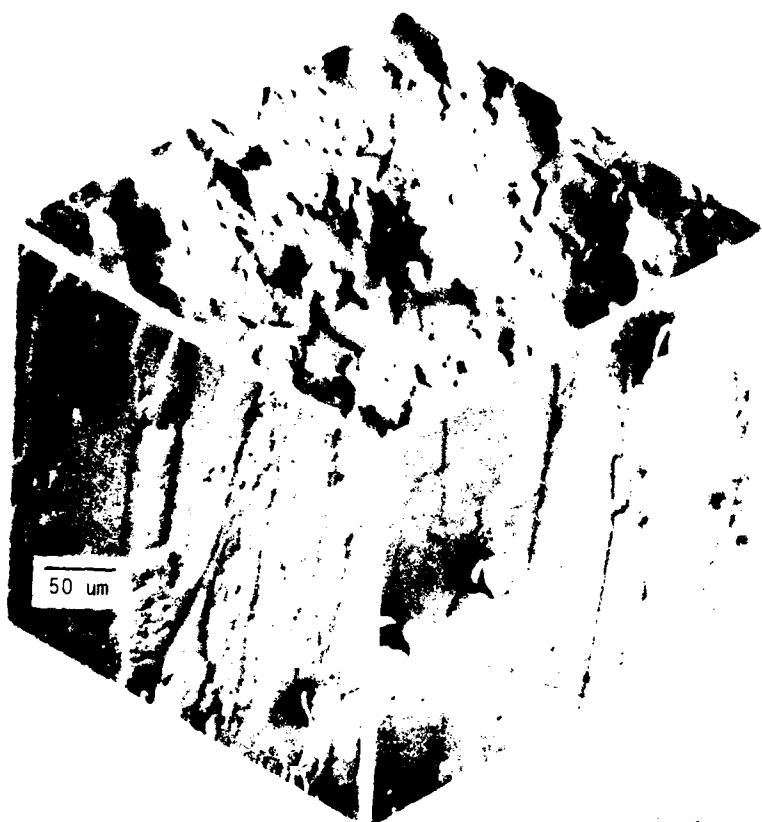


Figure 3-13. Weibull Plot of Flexure Data from Deposit HW-4-202



MONTAGE OF 400-200-4, TENSION ON TOP, ILLUSTRATING THE LINEAR ORIENTATION OF THE GRAIN STRUCTURE OF CVD-Si₃N₄. THE ANGULAR CHARACTER OF THE COLUMNAR GRAINS IS ATTRIBUTED TO THE INTER-PENETRATION OF THE CRYSTALS DURING THE GROWTH OF THE DEPOSIT.
(NOMARSKI CONTRAST)



MONTAGE OF 400-200-4,
COMPRESSION SIDE ON TOP.
(NOMARSKI CONTRAST)

Figure 3-14. Typical Microstructure of CVD α -Si₃N₄

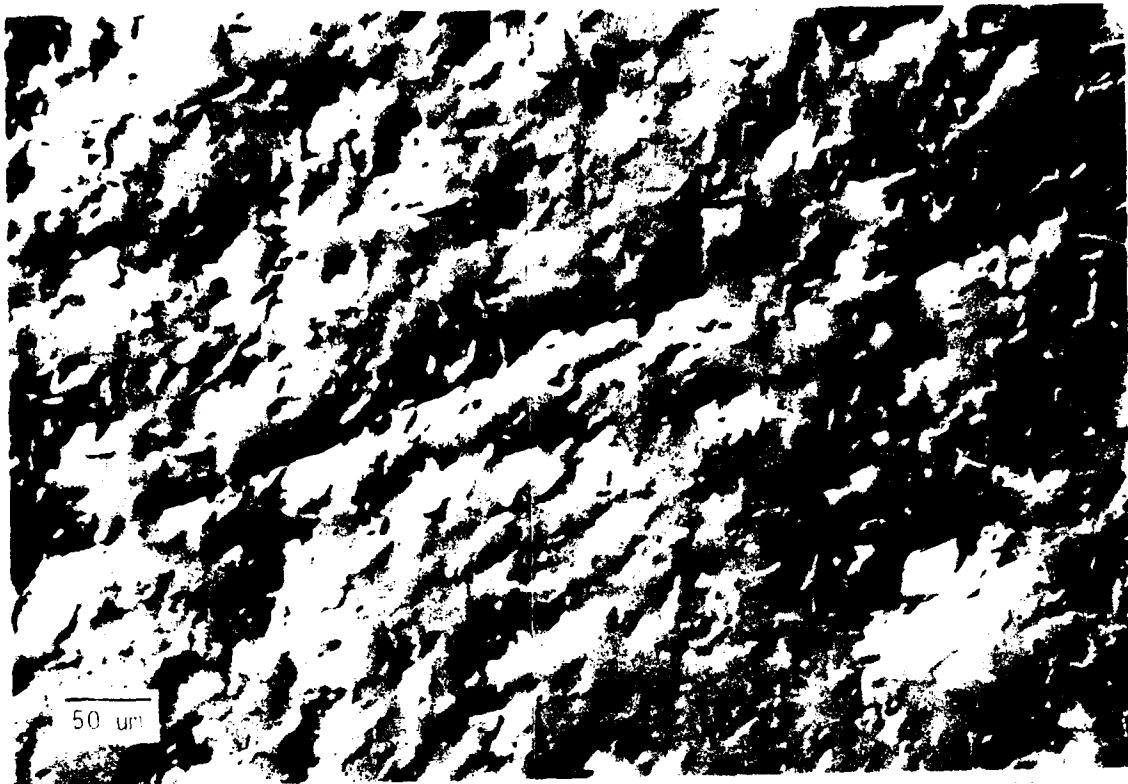


Figure 3-15. Tension Side (Top) and Compression Side (Bottom) of Flexure Specimen HW-4-200-4. Modulus of Rupture = 297.09 MPa (43.09 kpsi). (Nomarski Contrast)



Figure 3-16. Tension Side (Top) and Compression Side (Bottom) of Flexure Specimen HW-4-200-10. Modulus of Rupture = 194.64 MPa (28.23 kpsi). (Nomarski Contrast)

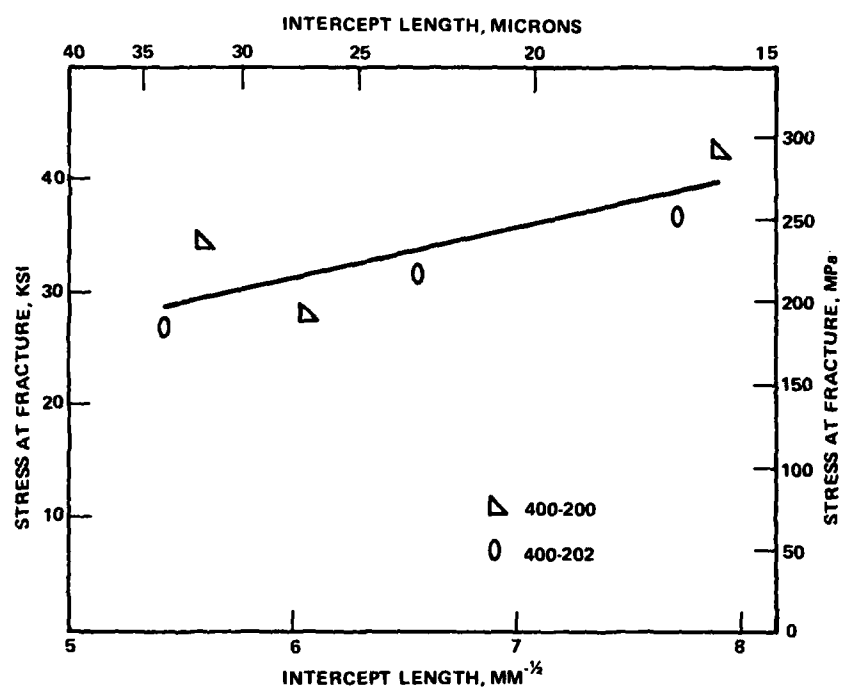
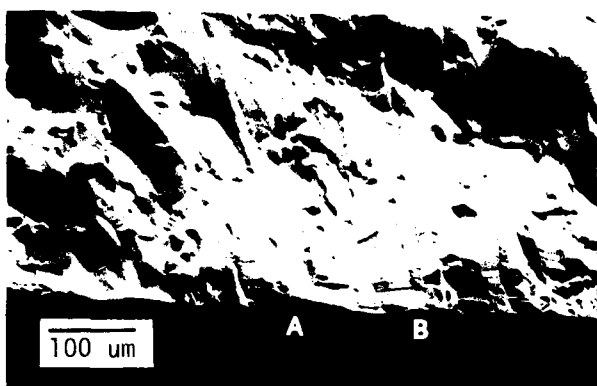
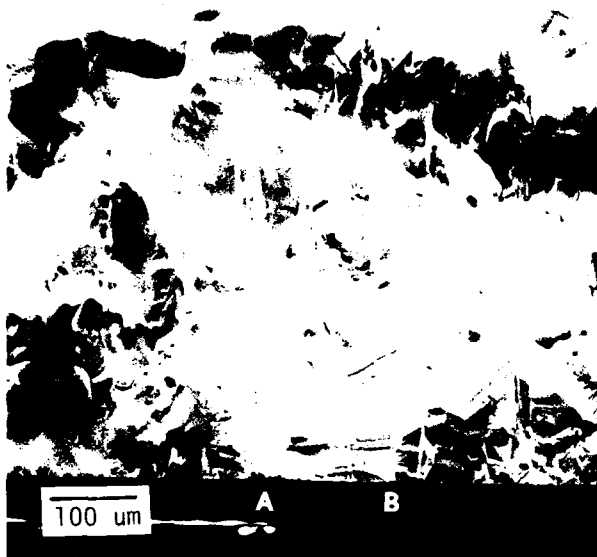


Figure 3-17. Fracture Stress: Grain Size Correlation



SPECIMEN TILTED 45° TO
ELECTRON BEAM TENSION
SIDE AT BOTTOM.

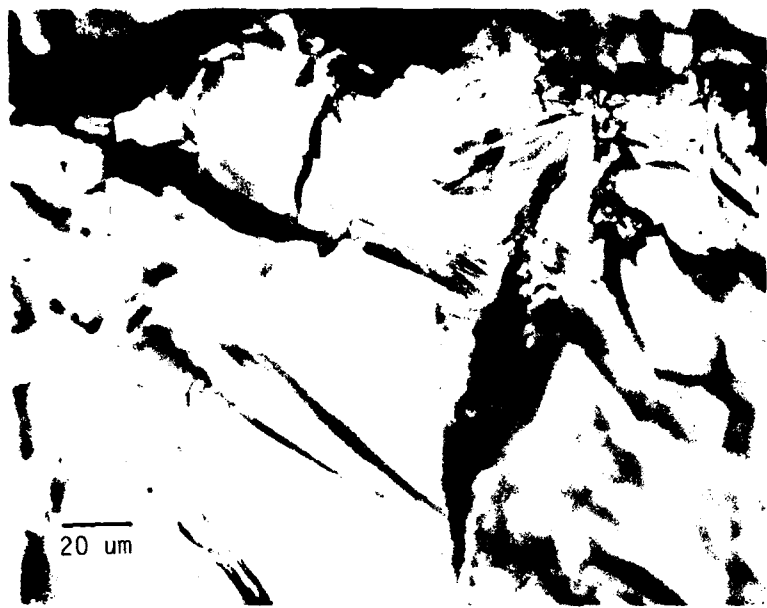


SPECIMEN ALMOST NORMAL TO BEAM.
THE DOMINANT FRACTURE MODE IS
CLEAVAGE. THE COLUMNAR NATURE
OF THE CVD-Si₃N₄ IS READILY
APPARENT WTH MANY DISCRETE
SITES OF CONCHOIDAL FRACTURE.



REGION A IS CONSIDERED A POS-
SIBLE FRACTURE INITIATION SITE
DUE TO THE RIVER PATTERNS LEADING
(IN GENERAL) TO THIS AREA, AND
THE SURFACE CRACKS AT THE TENSION
SIDE. (BOTTOM)

Figure 3-18. SEM Fractographs of Flexure
Specimen HW-4-202-2



OPTICAL FRACTOGRAPH
ILLUSTRATING CLEAVAGE STEPS
ENDING AT A TWIST BOUNDARY.
A TWIST BOUNDARY IS A GRAIN OR
SUBGRAIN BOUNDARY WITH
CLEAVAGE PLANES ROTATED ON AN
AXIS PREPENDICULAR TO THE
BOUNDARY. CLEAVAGE STEPS
USUALLY TERMINATE AT TWIST
BOUNDARIES.



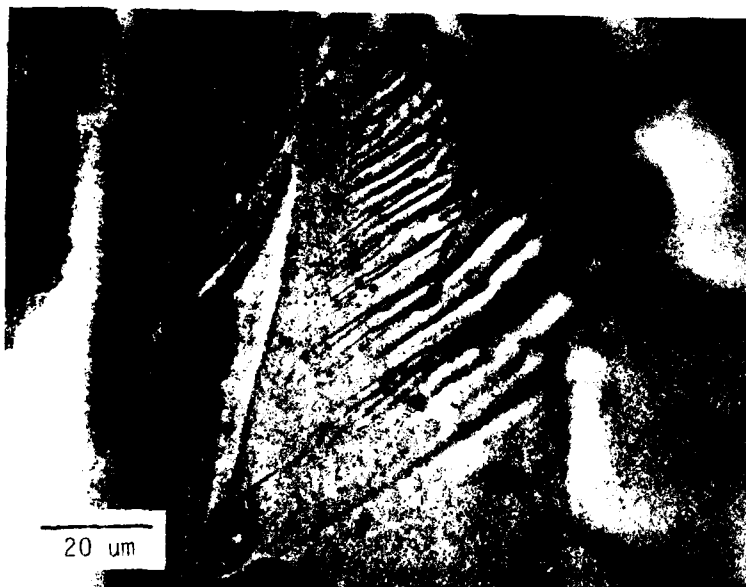
OPTICAL FRACTOGRAPH SHOWING
CLEAVAGE STEP PROPAGATION
ACROSS TILT BOUNDARIES.
TILT BOUNDARIES ARE CLEAVAGE
PLANES ROTATED ON AN AXIS
PARALLEL TO THE BOUNDARY.
CLEAVAGE STEPS USUALLY
PROPAGATE ACROSS TILT
BOUNDARIES.

Figure 3-19. Optical Fractographs of Flexure Specimen HW-4-202-11



OPTICAL FRACTOGRAPH
ILLUSTRATING THE
CLEAVAGE FEATURE CALLED
WALLNER LINES, A GROUP
OF INTERSECTING PARALLEL
LINES. WALLNER LINES ARE
THE RESULT OF INTERACTION
OF THE CRACK FRONT AND AN
ASSOCIATED ELASTIC SHOCK-
WAVE.

(A)



OPTICAL FRACTOGRAPH
SHOWS RIVER PATTERNS
OF A CLEAVAGE FRACTURE.
THESE FEATURES CORRECTLY
INDICATE THE FRACTURE
DIRECTION IS TOWARDS
THE UPPER RIGHT CORNER,
WHICH IS THE COMPRESSION
SIDE OF THE SPECIMEN.

(B)

Figure 3-20. Optical Fractographs of Flexure Specimen HW-4-202-10

SPECIMEN IS AN EXAMPLE OF A
FRACTURE SURFACE WHERE THE
COLUMNAR STRUCTURE OF THE
CVD-Si₃N₄ IS LESS APPARENT AND
REPRESENTS A SITUATION WHERE
INTERNAL MICROCRACKS PROBABLY
DOMINATED THE FRACTURE PATH
PROPAGATION.



REGION A ILLUSTRATES THE FRACTURE
MODE IS CLEAVAGE AND A POSSIBLE
INITIATION SITE.



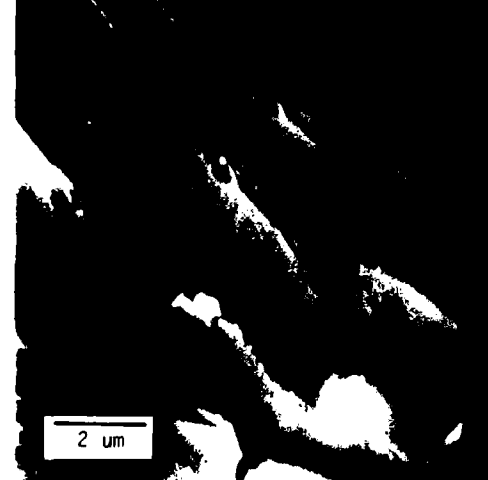
Figure 3-21. SEM Fractographs of Flexure Specimen HW-4-200-4



THE COMPRESSION SIDE OF
HW-4-202-10 ILLUSTRATING
CLEAVAGE STEPS AT A
TWIST BOUNDARY.



DETAIL OF CLEAVAGE STEPS AT A
TWIST BOUNDARY. THE RIVER
PATTERN INDICATES THE FRACTURE
PROPAGATION IN A DIRECTION
TOWARDS THE COMPRESSION SIDE
OF THE SPECIMEN.



DETAIL OF CLEAVAGE STEPS.
NOTE CHIPPED EDGES PROBABLY
DUE TO FRACTURE SURFACES
RUBBING TOGETHER.

Figure 3-22. SEM Fractographs of Compression Side of Flexure Specimen HW-4-202-10

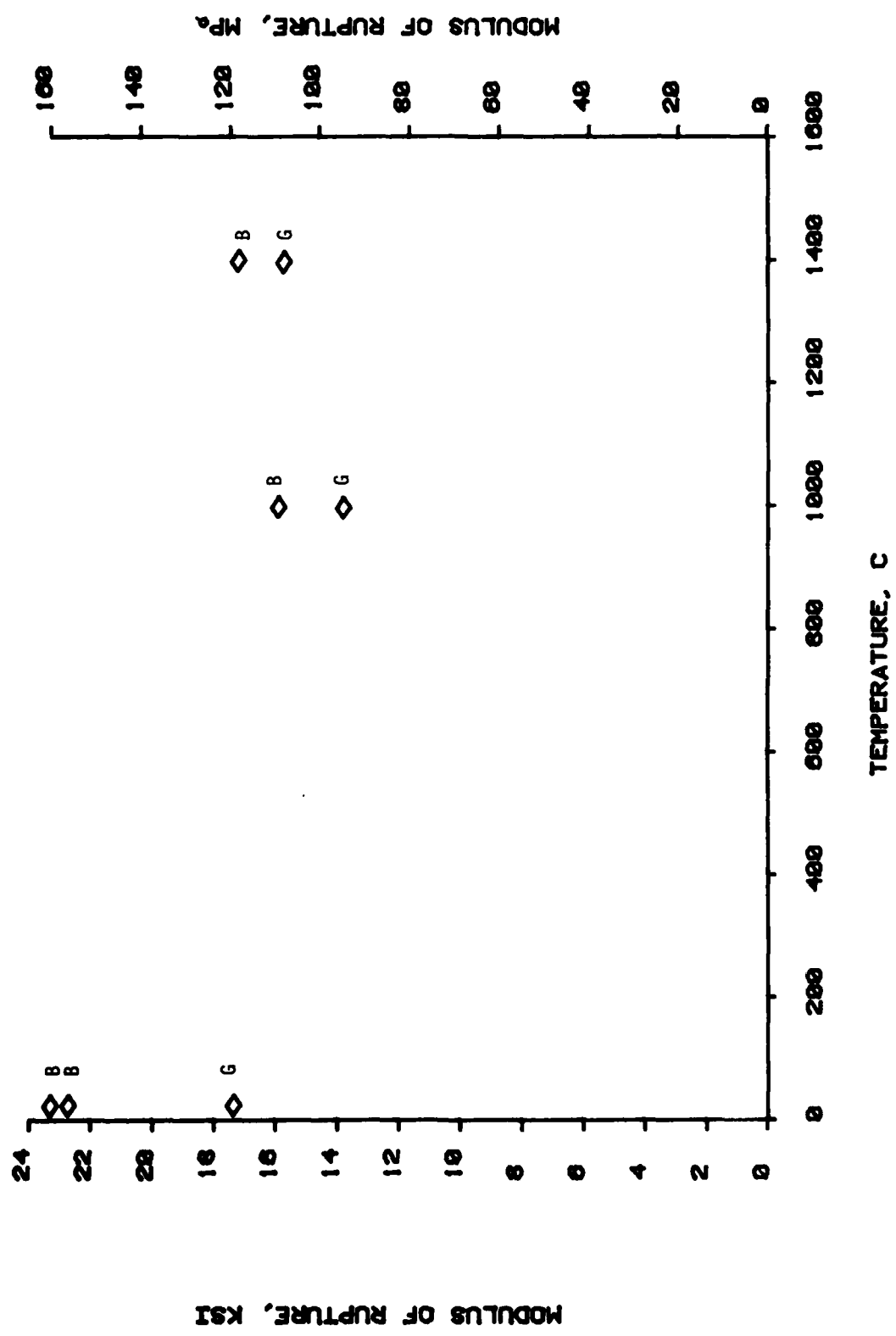
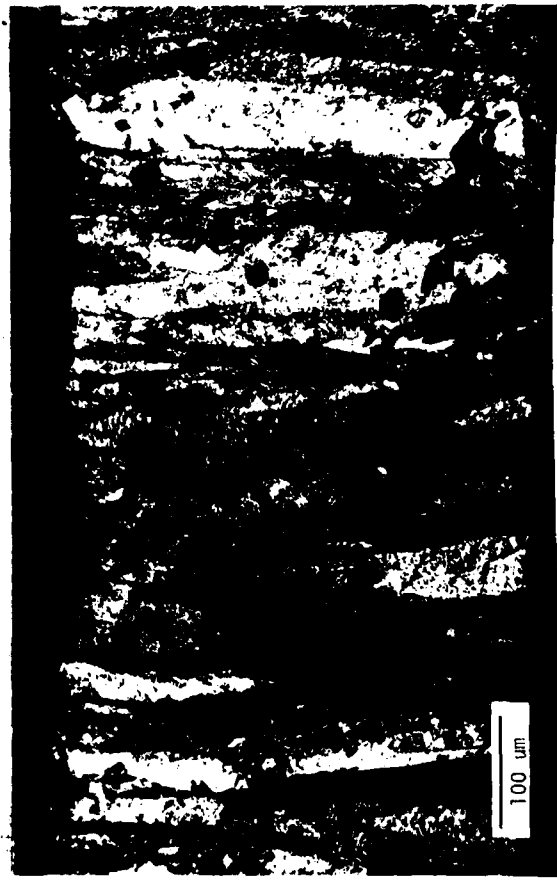


Figure 3-23. Flexure Strength as a Function of Color and Temperature (Run No. HW-4-139)



(A)



(B)

Figure 3-24. Microstructure of Polished (A) and Etched (B) Cross-Sections of Brown Flexure Specimen HW-4-139-B5. (See Table 3-12)



Figure 3-25. Microstructure of Polished (A) and Etched (B) Cross-Sections of Green Flexure Specimen HW-4-139-G3. (See Table 3-12)

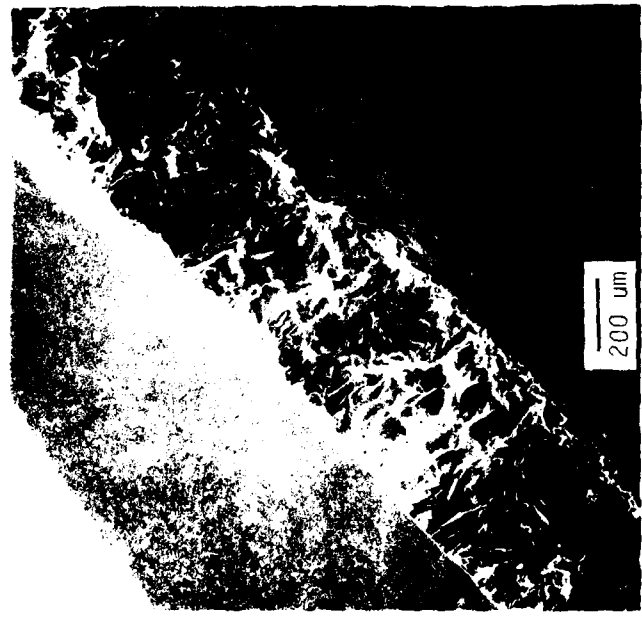
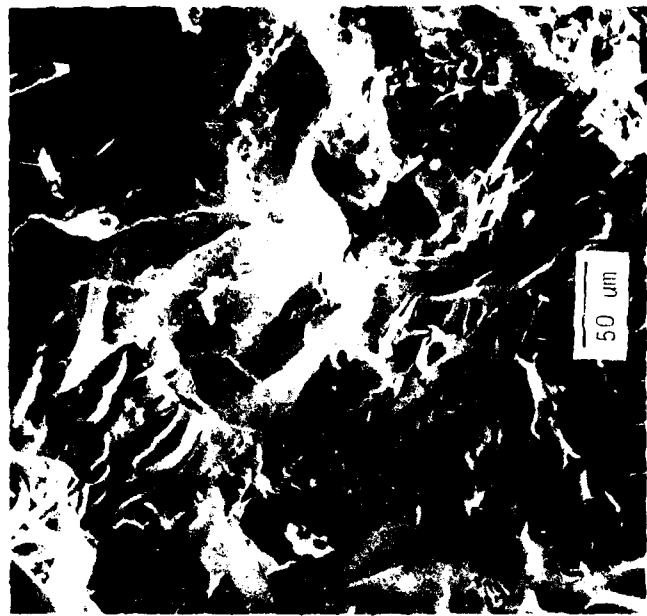


Figure 3-26. Fracture Surface of Brown α - Si_3N_4 (Spec. No. HW-4-139-B6) Tested at 1000°C (See Table 3-12)

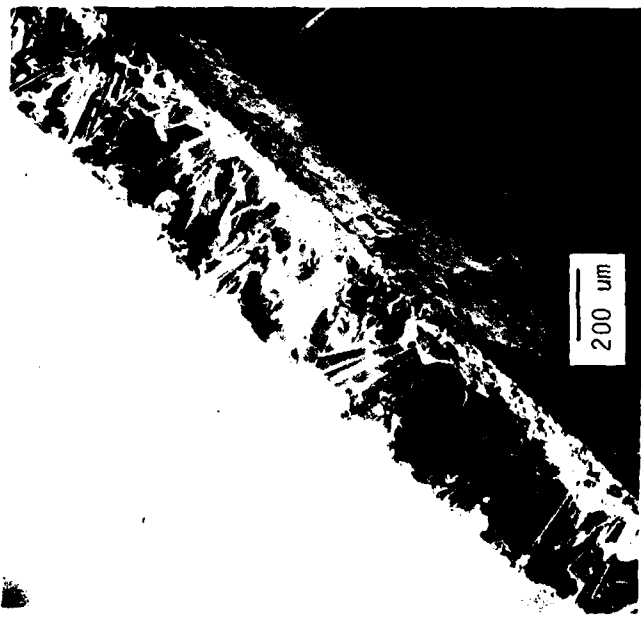
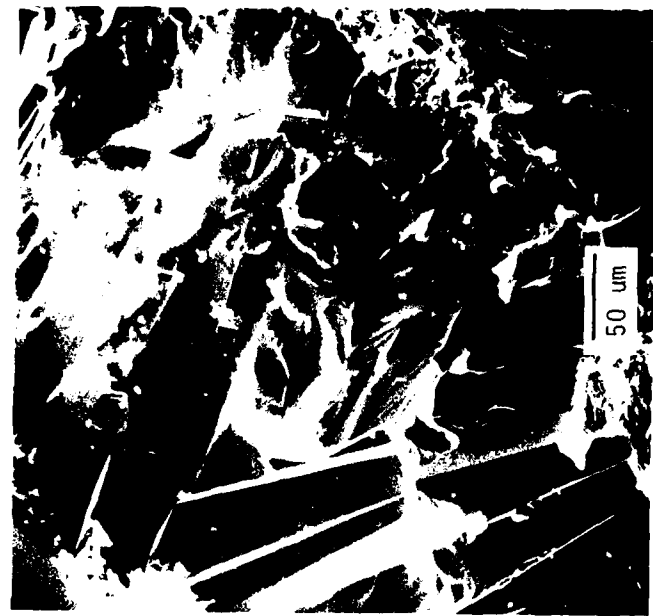


Figure 3-27. Fracture Surface of Green α - Si_3N_4 (Spec. No. HW-4-139-G4) Tested at 1000°C (See Table 3-12)

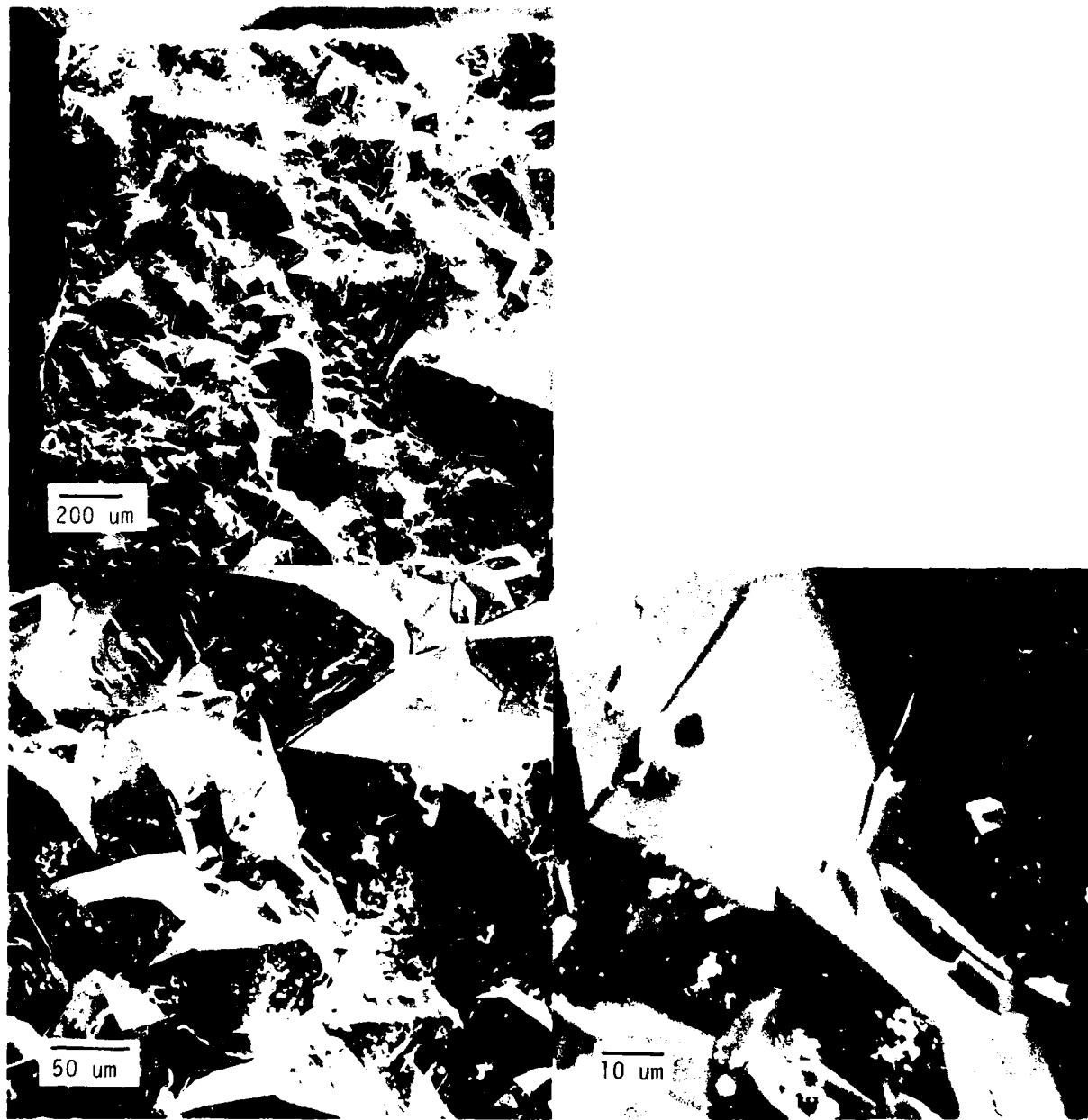


Figure 3-28. Photomicrograph Showing Tensile Stressed Surface of Flexure Specimen CW-19-2. Modulus of Rupture = 229.11 MPa (33.23 kpsi)



Figure 3-29. Optical Fractograph of Flexure Specimen CW-19-1. Modulus of Rupture = 238.97 (34.66 kpsi)

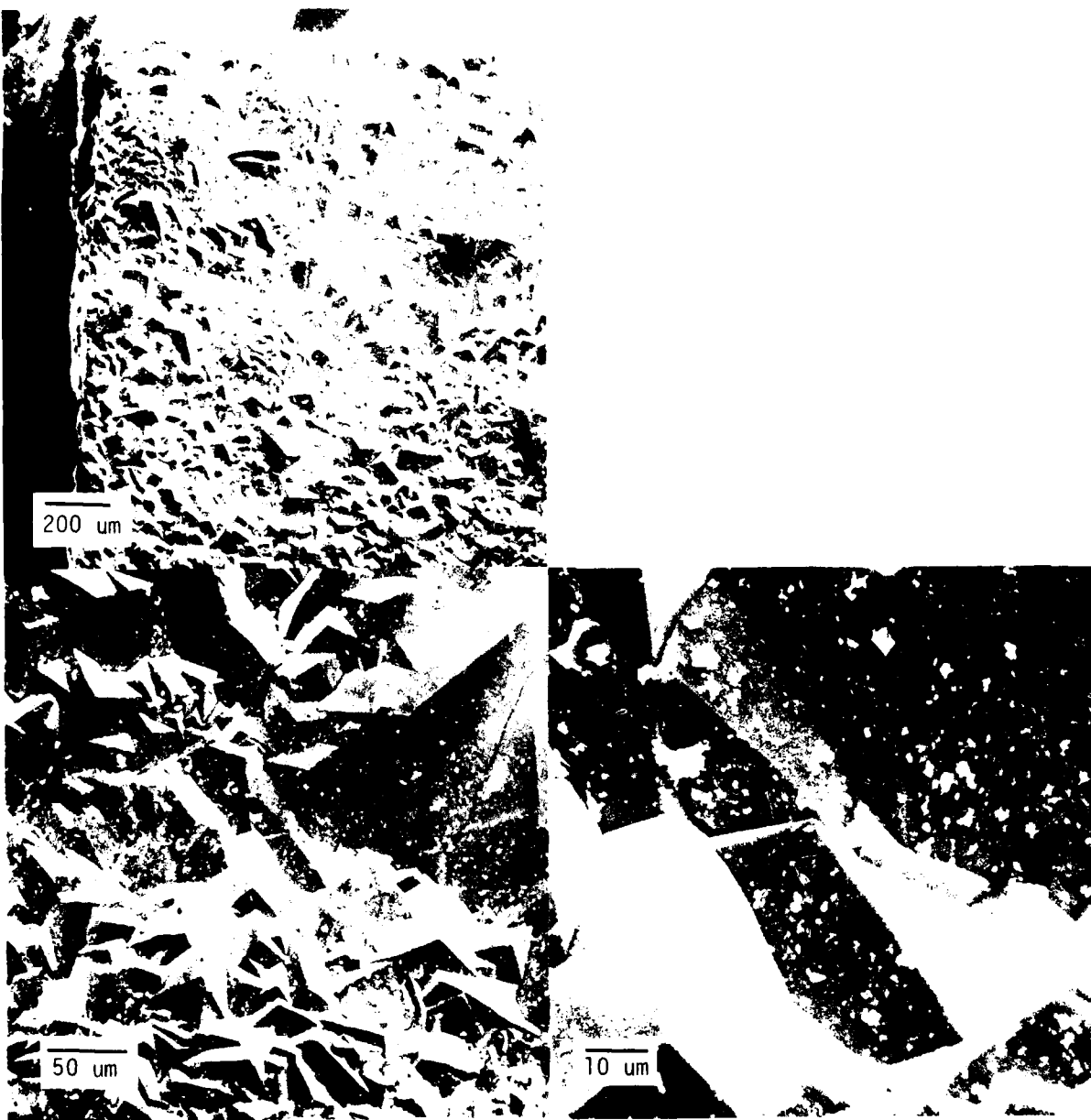


Figure 3-30. Photomicrograph Showing Tensile Stressed Surface of Flexure Specimen CW-30-2. Modulus of Rupture = 254.49 MPa (36.91 kpsi)



Figure 3-31. Optical Fractograph of Flexure Specimen CW-30-1. Modulus of Rupture = 267.24 MPa (38.76 kpsi)

Figure 3-32. Optical Fractograph of Flexure Specimen CW-32-2. Modulus of Rupture = 36.89 MPa (5.35 kpsi)



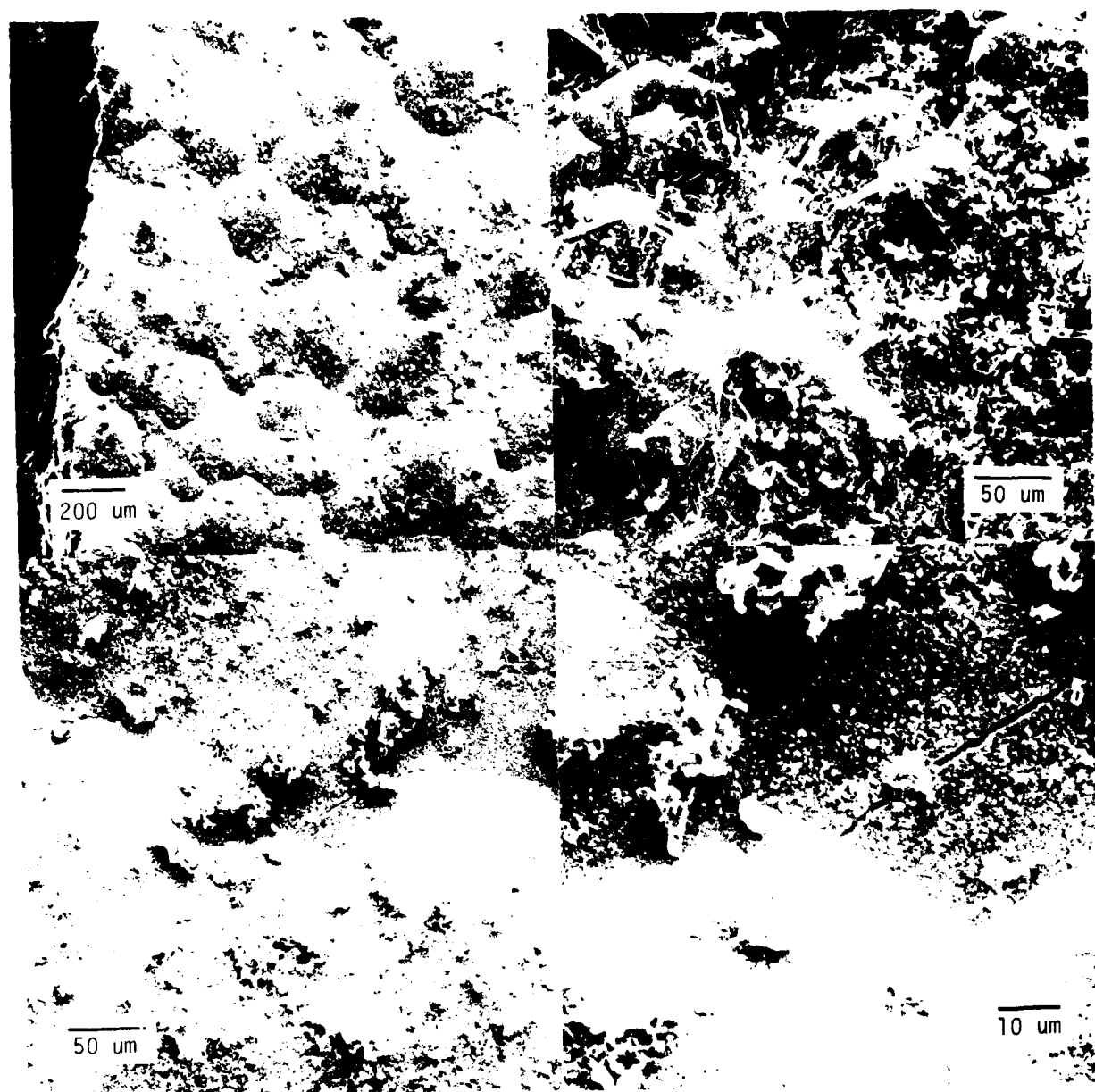


Figure 3-33. Photomicrograph Showing Tensile Stressed Surface of Flexure Specimen CW-32-1. Modulus of Rupture = 29.30 MPa (4.25 kpsi)



Figure 3-34. Optical Fractograph of Flexure Specimen CW-44-1. Modulus of Rupture = 111.28 MPa (16.14 kpsi)

SECTION 4.0
CONCLUSIONS

SECTION 4.0

CONCLUSIONS

Experimental work during this contract phase has led to the following conclusions:

1. Several processes have now been discovered for forming free-standing α - Si_3N_4 of near theoretically density using both "hot-wall" and "cold-wall" reactors (e.g., hot-wall reactor runs HW-4-81, 128, 200 and 202, and, cold-wall reactor runs CW-16, 19, 30, 35 and 36). Mechanical property measurements of these deposits indicate average flexure strengths (3-point) in the 200 to 300 MPa range. These strength levels may already be adequate for many close-in tactical missile applications.
2. Microstructural analyses of these deposits indicate strength is currently being limited by the polycrystalline grain morphology (grain-size,-shape and-orientation) and microcrack defect net-work within the bulk volume of deposits. Control of these extrinsic variables could provide higher strength level (estimated to be in excess of 1000 MPa).
3. Electromagnetic property evaluations continue to reinforce original expectations that the CVD form of silicon nitride may be useful as a multimode window with transmittance band-passes in the ultraviolet, visible, infrared and microwave range. Particularly noteworthy are the ultra-low absorption coefficients in the respective band passes (compared to other forms of Si_3N_4), and also, the relative insensitivity of these band-passes to elevated temperature effects.
4. Other physical properties of CVD α - Si_3N_4 (in addition to its mechanical and electromagnetic properties), such as its high electrical resistivity at elevated temperatures, high microhardness, corrosive resistance, and good thermal shock behavior, continue to suggest its utilization as a unique high-performance, structural ceramic.

**SECTION 5.0
RECOMMENDATIONS**

SECTION 5.0

RECOMMENDATIONS

Exploratory research during this contract phase has led to the following recommendations:

1. Processes identified in the hot-wall reactor should be further refined with emphasis on the formation of figured geometries (hemispherical and ogive shells). As part of this effort, experimental studies should be initiated addressing the development of low-cost cutting, grinding and polishing methods for preparing such shapes.
2. Exploratory processing research should continue in the laboratory-scale cold-wall reactor with the goal of developing microstructures leading to improvements in strength, and also, transmittance properties in the optical and infrared passbands (i.e., reduction of diffuse scattering). This work should emphasize the use of precursors which will favorably alter the nucleation and grain growth kinetics during deposition.
3. Physical property characterizations should be continued with the objectives of expanding and "filling-in" gaps regarding the intrinsic properties of α -Si₃N₄ synthesized by the chemical vapor deposition method.

**SECTION 6.0
REFERENCES**

SECTION 6.0

REFERENCES (SECTION 2)

- 2-1. Niihara, K. and Hirai, T., J. Mat. Sci 11 (1976) 593-603.
- 2-2. Niihara, K. and Hirai, T., J. Mat. Sci 11 (1976) 604-611.
- 2-3. Hirai, T., Niihara, K., Hayashi, S., and Goto, T. Science Reports of Res. Inst., Tohoku University Volume 26, November 4-5, March 1977.
- 2-4. Kijima, K., Setaka, N., Ishii, M., and Tanaka, H., J. Am. Ceram Soc. 56 346 (1973).
- 2-5. Billy, M; Compt. Rend. 246 (1958), No. 3, 433-436 ibid, 250 4163-4. (1960)
- 2-6. Glemser, O. and Naumann, P., Z. anorg u. allegm. Chemie 298 134-141 (1958).
- 2-7. Mellottée H., and Cochet, G., Rev. Int. Htes. Temp et Re'fract. 1976 31-36.
- 2-8. Cochet G., Mellottée, H., and Delbourgo, R., Proc 5th Int. Conf. on CVD., 1975 pp. 43-55.
- 2-9. Niihara, K., and Hirai, T., J. Mat. Sci 13 (1978) 2585-2393.
- 2-10. Kijima, K., Yogyo Kyokai Shi 83 46-47 (1975). cf. MC1C-79-41 Annotated Bibliography on Silicon Nitride for Structural Applications D. Messier and M. Murphy, July 1979.
- 2-11. Lin, S.S., J. Am Ceram Soc. 58 271-73 (1975).
- 2-12. Lindley, M. W. et al, J. Mat. Sci, 14 70-85 (1979).
- 2-13. Messier, D. R., Wong P. and Ingram, A. E., J. Am. Ceram. Soc. 56 171-2 (1973).
- 2-14. Mitomo, M., Tanaka, H. and Tanaka, J., Yogyo Kyokai Shi 82 144-45 (1974) cf. MC1C-79-41 (Ref. 560).

REFERENCES (SECTION 3)

- 3-1. Tanzilli, R. A. et. al., "Chemical Vapor Deposition of Silicon Nitride", GE-RESD Doc. No. 77SDR2257, September, 1977.
- 3-2. Niihara, K., Hirai, T., J. Mat. Sci., 12, 1233-1242 (1977).
- 3-3. Wild, S., et. al., "The Crystal Structures of Alpha and Beta Silicon and Germanium Nitrides", published in Special Ceramics 5, British Ceramic Research Association, 1972, pp. 385-395.
- 3-4. Slack, G.A., J. Phys. Chem. Solids 34, (1973) 321
- 3-5. Bauer, J., "Optical Properties, Band Gap, and Surface Roughness of Si_3N_4 ", Phys. Stat. Sol. 39, 411 (1977).
- 3-6. "Advanced Optical Ceramics - Phase 2" ONR Contract No. N00014-78-C-0466 (in progress).
- 3-7. Brazel, J. et al, "Millimeter Wave Hardened Antenna Window Materials Development", AMMRC TR 79-45, August, 1979.
- 3-8. Davies, D.G.S., "The Statistical Approach to Engineering Design in Ceramics", Proc. Brit. Ceram. Soc., Vol. 22, 1973, pp. 429-452.
- 3-9. Evans, A.G. et. al., "The Strength and Oxidation of Reaction - Sintered Silicon Nitride" Journal of Material Science, Vol. 5, 1970, pp. 314-325
- 3-10. Edington, J.W., "The Mechanical Properties of Silicon Nitride and Silicon Carbide - Part I: Materials and Strength", Powder Metallurgy International, Vol. 7, No. 2, 1975, pp. 88-89.
- 3-11. Evans, A.G. et. al., "Fracture Toughness Determinations by Indentation", J. of Am. Ceram. Soc., Vol. 59, No. 7-8, July-August 1976, pp. 371-372.
- 3-12. Edington, J. W., et. al., "The Mechanical Properties of Silicon Nitride and Silicon Carbide - Part II Engineering Properties", Powder Metallurgy International, Vol. 7, No. 3, 1975, p. 136-137.
- 3-13. Bansal, G.K. et. al., "Strength Analysis of Brittle Materials", Final Report on ONR Contract No. N00014-73-C-0408, November, 1977. pp. B-2, 3.
- 3-14. Niihara, K. et. al., "Growth, Morphology and Slip System of $\alpha\text{-Si}_3\text{N}_4$ Single Crystal", J. Mat. Sci., Vol. 14, 1979, pp. 1952-1960.

REFERENCES (SECTION 3) (Continued)

- 3-15. Henderson, C. M. B., et. al., "Thermal Expansion of the Nitrides and Oxynitride of Silicon in Relation to their Structures", Trans. Brit. Ceram. Soc., Vol. 75, 1976, pp. 49-53.
- 3-16. Hirai, T., et. al., "Thermal Diffusivity, Specific Heat and Thermal Conductivity of Chemically Vapor-Deposited Si₃N₄", Ceramic Bulletin, Vol. 57, No. 12, 1978, pp. 1126-1130.

**APPENDIX A
PRECISION LATTICE DETERMINATION
ON BROWN AND WHITE α - Si_3N_4**

APPENDIX A

PRECISION LATTICE DETERMINATIONS ON BROWN AND WHITE $\alpha\text{-Si}_3\text{N}_4$

The samples analyzed were in the form of polished thin plates which had previously been characterized in terms of their optical properties (Ref. 3-1). Some physical characteristics of the two samples are listed below:

Sample	Color	Thickness	Area (Approximate)
HW4-128	amber	0.010 in (0.25 mm)	0.75 in x 0.75 in (19 mm x 19 mm)
HW4-129	white	0.011 in (0.28 mm)	0.75 in x 0.75 in (19 mm x 19 mm)

Corners approximately 50 mm² were broken off of each plate. The broken corners were pulverized in a clean steel mortar. The resulting powders were first passed over a magnet to remove any steel particles resulting from pulverization and then passed through a 320 mesh sieve. Each of the (-)320 mesh $\alpha\text{-Si}_3\text{N}_4$ powders were then mixed with equal volumes of (-)320 mesh, silicon powder (NBS-silicon standard). The silicon was added to each sample as an internal standard which would later be used to permit us to make appropriate corrections for the $\alpha\text{-Si}_3\text{N}_4$ diffraction data in our determinations of precision lattice parameters.

The powders, $\alpha\text{-Si}_3\text{N}_4$ plus Si, were packed into 0.3 mm φ , 0.01 mm wall thickness, Lindemann glass capillaries. Diffraction photographs were then obtained using vanadium filtered chromium X-radiation in a 57.3 mm φ powder diffraction camera. The positions, ℓ , of the resulting X-ray diffraction lines on the diffraction photographs were very carefully measured using a film measuring system with a resolution of 0.05 mm. The film in the powder camera was mounted in the asymmetric manner (Straumanis method) and the camera constant ($K = \text{degrees of } \theta/\text{mm measured on film}$) for each film was determined from measurements made on several pairs of forward and back diffraction lines. The two positions $\ell_{\theta=0^\circ}$ and $\ell_{\theta=90^\circ}$ were determined ($\theta = \text{Bragg diffraction angle}$) and the diffraction

angles θ were determined from the relation: $\theta = K(\ell - \ell_{\theta=0})$. The interplanar (atomic planes) separations, d , were determined for each of the diffraction lines between $\theta = 0^\circ$ to $\theta = 90^\circ$ using Bragg's law

$$d = \frac{\lambda}{2 \sin \theta}$$

where $\lambda = Cr K_\alpha = 2,29092 \text{ \AA}$

Corrections in $\alpha\text{-Si}_3\text{N}_4$ d -values were then made using the following method.

From the d -values associated with the silicon internal standards on each paragraph and a knowledge of the precision lattice parameter of silicon, i.e., a_0 (silicon) = 5.4301 \AA , from ASTM card 5-565, the correction Δd_{Si} for each silicon line was determined:

$$\Delta d_{\text{Si}} = d_{0\text{Si}} - d_{\text{measured Si}}$$

where $d_{0\text{Si}} = a_{0\text{Si}} (h^2 + k^2 + \ell^2)^{-\frac{1}{2}}$, where h, k, ℓ are the Miller indices for the family of reflecting planes.

A least square linear fit for the values of Δd_{Si} versus f was then made where f is the Nelson and Riley extrapolation function,

$$f = \frac{1}{2} \left(\frac{\cos^2 \theta}{\sin \theta} + \frac{\cos^2 \theta}{\theta} \right).$$

The equation for the least square fitted straight line was determined, its form was:

$$\Delta d = mf + b.$$

Using this relation, corrections for each $\alpha\text{-Si}_3\text{N}_4$ d -value were made. Presented in Table A-1 are the corrected d -values for the two $\alpha\text{-Si}_3\text{N}_4$ samples HW-4-128-1 and HW-4-129-2. Included in Table A-1 for comparison, is the ASTM data from ASTM reference card 9-250 for $\alpha\text{-Si}_3\text{N}_4$. All calculations in our work were carried out using six significant figures. Although the data in Table A-1 are shown to six significant figures they are probably no more accurate than to five significant figures.

TABLE A-1. X-RAY DIFFRACTION DATA FOR α -Si₃N₄

ASTM 9-250			HW-4-128-1			HW-4-129-2		
I/I ₀	d(Å)	hkl	I	d(Å)	hkl	I	d(Å)	
8	6.69	100	mW	6.59775				
60	4.32	101	ms	4.30182				
30	3.88	110	w	3.84296				
30	3.37	200	nW	3.35059				
85	2.893	201	s	2.87944	201			
6	2.823	002				ms	4.30114	
75	2.599	102	ms	2.59049	102	ms	3.85382	
100	2.547	210	s	2.53670	210	s	3.36742	
60	2.320	211	m	2.30859	211	m	2.88623	
8	2.283	112						
6	2.244	300				ms	2.59152	
30	2.158	202	m	2.16151	202	s	2.53772	
55	2.083	301	m	2.07512	301	m	2.31310	
2	1.937	220						
8	1.884	212				nW	2.15338	
8	1.864	310				m	2.08147	
12	1.806	103	w	1.80192	103			
25	1.771	311	w	1.77012	311	nW	1.88597	
2	1.751	302				w	1.80059	
8	1.637	203				w	1.76702	
35	1.596	222	m	1.59651	222	m	1.59681	
2	1.552	312						
6	1.542	320				w	1.50283	
8	1.507	213	w	1.50944		ms	1.48417	
70	1.486	321	s	1.48836	321	ms	1.43651	
55	1.437	303	ms	1.44031	303	ms	1.41786	
60	1.418	411	ms	1.41876	411	nW	1.40447	
20	1.406	004	w	1.40712		nW	1.37831	
12	1.376	104	s	1.35122	322	s	1.35184	
75	1.351	322						
2	1.343	500	m	1.32161	114,	m	1.32011	
30	1.321	313			313			
16	1.306	501	nW	1.30859	501	nW	1.30775	
50	1.299	412	ms	1.30108	412	ms	1.29903	
30	1.293	330	nW	1.29500	330	m	1.29298	
8	1.269	420	w	1.26900				
30	1.238	421	w	1.23957	421	m	1.23790	
30	1.229	214	m	1.22997	214	m	1.23006	
8	1.213	502						

w=weak, m=medium, s=strong, n=very

The values for a_0 and c_0 (hexagonal unit cell dimensions) were then determined for the two $\alpha\text{-Si}_3\text{N}_4$ samples using the corrected d-values and the relation for the hexagonal unit cell:

$$\frac{1}{d^2} = \frac{4}{3} \left(\frac{h^2 + hk + k^2}{a^2} \right) + \frac{\ell^2}{c^2}$$

Again, a least square determination was made. The method used is outlined below.

A function $S(x, y)$ is defined:

$$S(x, y) \equiv \sum_{i=1}^N w_i \left\{ f_i^{(c)} - f_i^{(d)} \right\}^2$$

where $f_i^{(d)} = \frac{1}{d_i^2}$ (measured),

$$f_i^{(c)} = \alpha_i x + \beta_i y,$$

and w_i = weighting function which we assumed to be unity since the d-values we used were corrected values.

$$\alpha_i \equiv \frac{4}{3} (h^2 + hk + k^2)$$

$$\beta_i \equiv \ell^2$$

$$x \equiv \frac{1}{2} \frac{1}{a_0}$$

$$y \equiv \frac{1}{2} \frac{1}{c_0}$$

For condition of least squares:

$$\frac{\partial S}{\partial x} = \frac{\partial S}{\partial y} = 0$$

Hence, since

$$S(x, y) = \sum_{i=1}^N w_i \left\{ \alpha_i x + \beta_i y - f_i^{(d)} \right\}^2$$

Then, from $\frac{\partial S}{\partial x} = 0$ and $\frac{\partial S}{\partial y} = 0$, we have,

$$\begin{aligned} (\sum w_i \alpha_i^2) x + (\sum w_i \alpha_i \beta_i) y &= \sum w_i \alpha_i f_i^{(d)} \\ (\sum w_i \alpha_i \beta_i) x + (\sum w_i \beta_i^2) y &= \sum w_i \beta_i f_i^{(d)} \end{aligned}$$

A computer program was written for the solution of the above least square relations in which one supplies d-values and h, k, l for any number of diffraction lines in the hexagonal system and one then obtains values for x and y and hence obtains the lattice parameters a_0 and c_0 . The computer listing for this program (HEXLSQ) is presented in Table A-2.

Twenty h k l values from Table A-1 were selected to be run in our least square determination of a_0 and c_0 for each of our α -Si₃N₄ samples. The twenty lines selected are shown in the h k l column between the two experimentally determined d-values (for samples HW4-128-1 and HW4-128-2) in Table A-1. The computer read out for this data is presented in Table A-3.

TABLE A-2. COMPUTER LISTING OF LATTICE PARAMETER CODE

```

*OLD HEXLSQ
*DELETE 00371-00379
*RESAVE HEXLSQ
DATA SAVED-HEXLSQ
*LIST

00010      DIMENSION D(100),H(100),EK(100),EL(100),ALPHA(100),BETA(100),F(100
00015      PRINT:"READ NO. OF VALUES"
00016      READ:N
00025      PRINT:" READ D,H,K,L, ONE SET AT A TIME"
00030      DO 3 I=1,N
00050      3 READ:D(I),H(I),EK(I),EL(I)
00110      SUM1=0.
00120      SUM2=0.
00130      SUM3=0.
00140      SUM4=0.
00145      SUM5=0.
00150      DO 1 J=1,N
00160      F(J)=1./(D(J)**2)
00170      ALPHA(J)=H(J)**2+H(J)*EK(J)+EK(J)**2
00175      ALPHA(J)=(4./3.)*ALPHA(J)
00180      1 BETA(J)=EL(J)**2
00190      DO 2 I=1,N
00200      SUM1=SUM1+ALPHA(I)**2
00210      SUM2=SUM2+ALPHA(I)*BETA(I)
00220      SUM3=SUM3+BETA(I)**2
00230      SUM4=SUM4+ALPHA(I)*F(I)
00240      2 SUM5=SUM5+BETA(I)*F(I)
00250      DENOM=SUM1*SUM3-SUM2*SUM2
00320      X=(SUM4*SUM3-SUM2*SUM5)/DENOM
00330      Y=(SUM1*SUM5-SUM2*SUM4)/DENOM
00340      PRINT:"X=",X
00345      PRINT:"Y=",Y
00350      AO=1./SQRT(X)
00360      PRINT:"AO=",AO
00370      PRINT:"CO=",1./SQRT(Y)
00380      STOP
00390      END

*NEWU

```

TABLE A-3. COMPUTER READOUT OF DATA

HW-4-128-1

```
*FRUN
READ NO. OF VALUES
=20
  READ D,H,K,L, ONE SET AT A TIME
=2.87944,2.,0.,1.
=2.59049,1.,0.,2.
=2.53670,2.,1.,0.
=2.30859,2.,1.,1.
=2.16151,2.,0.,2.
=2.07512,3.,0.,1.
=1.80192,1.,0.,3.
=1.77012,3.,1.,1.
=1.59651,2.,2.,2.
=1.48836,3.,2.,1.
=1.44031,3.,0.,3.
=1.41876,4.,1.,1.
=1.35122,3.,2.,2.
=1.32161,1.,1.,4.
=1.32161,3.,1.,3.
=1.30859,5.,0.,1.
=1.30108,4.,1.,2.
=1.29500,3.,3.,0.
=1.23957,4.,2.,1.
=1.22997,2.,1.,4.
X= 0.16586773E-01
Y= 0.31639522E-01
AO= 0.77645993E 01
CO= 0.56219249E 01
```

HW-4-129-1

```
*FRUN
READ NO. OF VALUES
=20
  READ D,H,K,L, ONE SET AT A TIME
=2.88623,2.,0.,1.
=2.59152,1.,0.,2.
=2.53772,2.,1.,0.
=2.31310,2.,1.,1.
=2.15338,2.,0.,2.
=2.08147,3.,0.,1.
=1.80059,1.,0.,3.
=1.76702,3.,1.,1.
=1.59681,2.,2.,2.
=1.48417,3.,2.,1.
=1.43651,3.,0.,3.
=1.41786,4.,1.,1.
=1.35184,3.,2.,2.
=1.32011,1.,1.,4.
=1.32011,3.,1.,3.
=1.30775,5.,0.,1.
=1.29903,4.,1.,2.
=1.29298,3.,3.,0.
=1.23790,4.,2.,1.
=1.23006,2.,1.,4.
X= 0.16622570E-01
Y= 0.31685348E-01
AO= 0.77562341E 01
CO= 0.56178581E 01
```

**APPENDIX B
COMPILATION OF FRACTURE TOUGHNESS
DATA ON FLEXURE SPECIMENS FROM
DEPOSITIONS HW-4-200 AND -202.**

TABLE B-1. FRACTURE TOUGHNESS BY INDENTATION
FOR FLEXURE SPECIMEN HW-4-202-2.

Indent	Indentation Load (kg)	Hardness		K_I (MN/m ^{0.5})					
		kg/sq.mm	N/sq.m	1	2	3	4	Avg	S
1	0.50	2314.	22.69	3.48	3.18	2.96	3.00	3.16	0.27
2	0.50	2479.	24.31	0.00	0.00	2.56	3.72	3.14	0.63
3	0.50	2406.	23.68	3.73	2.54	2.96	0.00	3.06	0.61
4	1.00	2184.	20.63	5.89	2.74	4.35	3.92	4.81	0.96
5	1.00	2294.	22.50	2.79	3.78	2.97	3.70	3.30	0.53
6	1.00	2326.	22.81	4.38	3.05	2.93	3.23	3.53	0.59

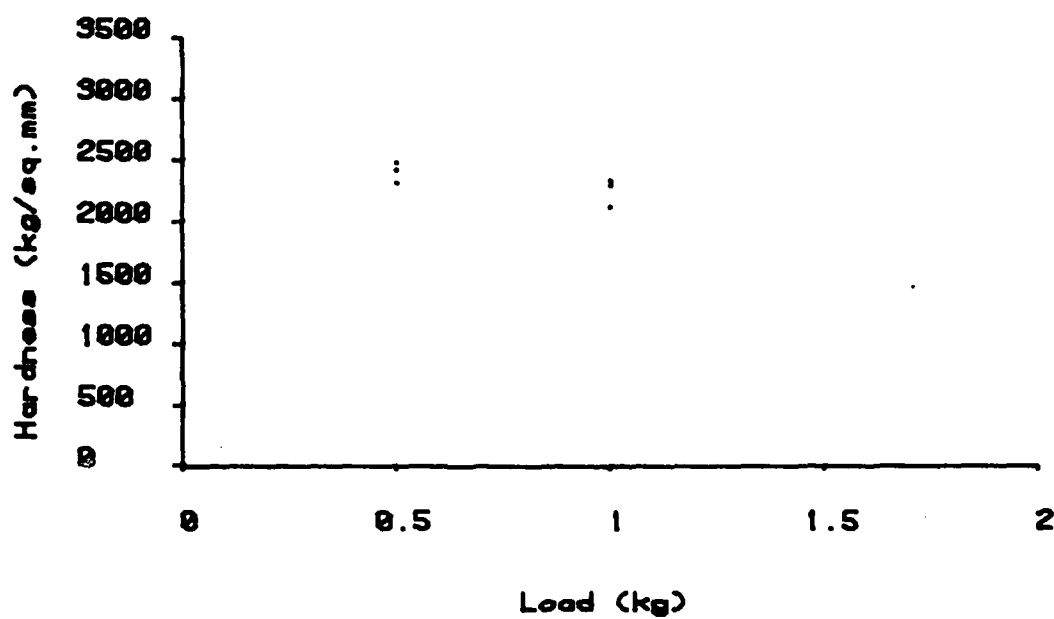


TABLE B-2. FRACTURE TOUGHNESS BY IDENTATION
FOR FLEXURE SPECIMEN HW-4-202-1

Indent	Indentation Load (kg)	Hardness		K _{Ic} (MN/M ^{0.5})				Avg	S
		kg/sq.mm	N/mm ²	1	2	3	4		
1	0.18	2620.	25.69	2.98	2.63	2.12	0.00	2.56	0.40
2	0.18	2745.	26.92	2.81	2.61	3.00	5.27	2.98	0.29
3	0.18	2611.	27.56	2.25	2.13	2.71	0.00	2.36	0.31
4	0.20	2911.	22.66	2.91	3.05	2.61	3.42	3.05	0.27
5	0.20	2288.	21.66	2.68	2.81	2.69	3.68	2.98	0.73
6	0.20	2311.	22.66	2.66	0.00	2.29	3.29	2.75	0.58
7	0.50	2438.	23.63	2.61	2.54	2.68	3.77	2.96	0.56
8	0.50	2529.	24.68	2.15	2.62	2.66	3.19	2.76	0.44
9	0.50	2478.	24.31	2.62	2.56	3.20	0.00	2.68	0.34
10	1.00	2641.	25.90	2.00	2.84	2.56	4.00	3.00	0.66
11	1.00	2358.	29.12	3.21	2.71	1.00	3.01	2.66	0.66
12	1.00	2342.	22.97	4.82	2.98	2.51	3.45	3.00	0.76
13	1.50	2894.	27.78	2.92	3.28	0.00	3.56	3.25	0.32
14	1.50	2321.	22.78	3.62	3.18	0.00	3.00	3.27	0.32
15	1.50	2347.	23.02	4.15	2.35	2.94	3.00	3.11	0.75

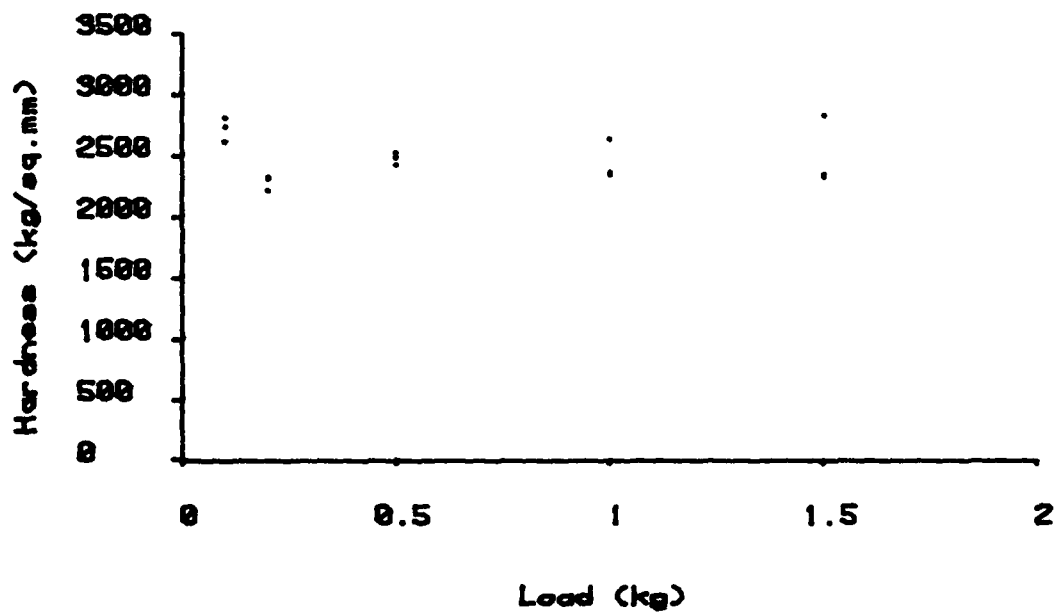


TABLE B-3. FRACTURE TOUGHNESS BY INDENTATION
FOR FLEXURE SPECIMEN HW-4-202-10

Indent	Indentation Load (kg)	Hardness		K _c (MN/M ^{0.5})					
		kg/sq.mm	N/sq.m	1	2	3	4	Ave.	S
1	0.05	2648.	27.93	2.47	2.47	0.00	0.00	2.47	0.00
2	0.10	2679.	28.23	2.73	0.00	0.00	2.10	2.41	0.45
3	0.10	3023.	29.64	2.67	2.29	2.29	0.00	2.42	0.22
4	0.10	3178.	31.16	2.71	3.06	2.76	0.00	2.65	0.20
5	0.20	2622.	25.71	3.26	3.07	3.15	3.15	3.16	0.06
6	0.20	2709.	26.57	2.99	3.03	3.06	2.84	2.98	0.10
7	0.20	2421.	23.74	2.70	2.77	2.93	3.70	2.88	0.56
8	0.50	2581.	25.31	3.72	2.42	2.68	3.57	3.10	0.64
9	0.50	2270.	22.26	2.69	2.31	2.91	0.00	2.70	0.34
10	0.50	2504.	24.55	2.53	2.49	2.67	3.73	2.66	0.58
11	1.00	2529.	24.81	3.04	4.21	2.83	3.44	3.38	0.61
12	1.00	2459.	24.11	3.33	2.56	2.98	3.46	3.08	0.40
13	1.00	2248.	22.86	2.74	2.57	3.05	3.37	2.93	0.36
14	1.50	2556.	25.09	3.14	2.19	3.51	2.45	2.82	0.61
15	1.50	2442.	23.95	2.87	3.37	4.15	3.14	3.33	0.82

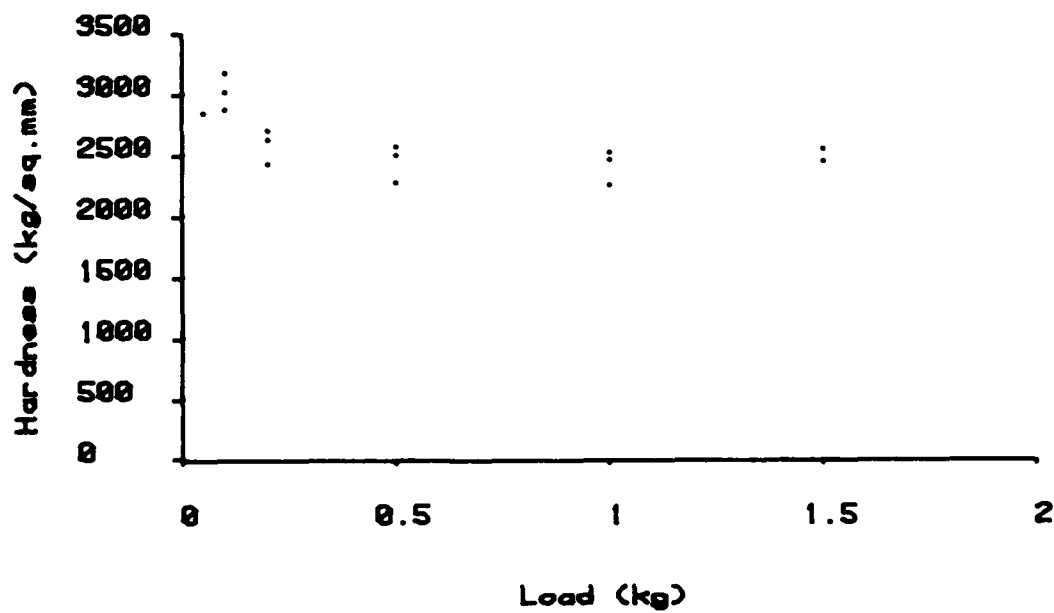
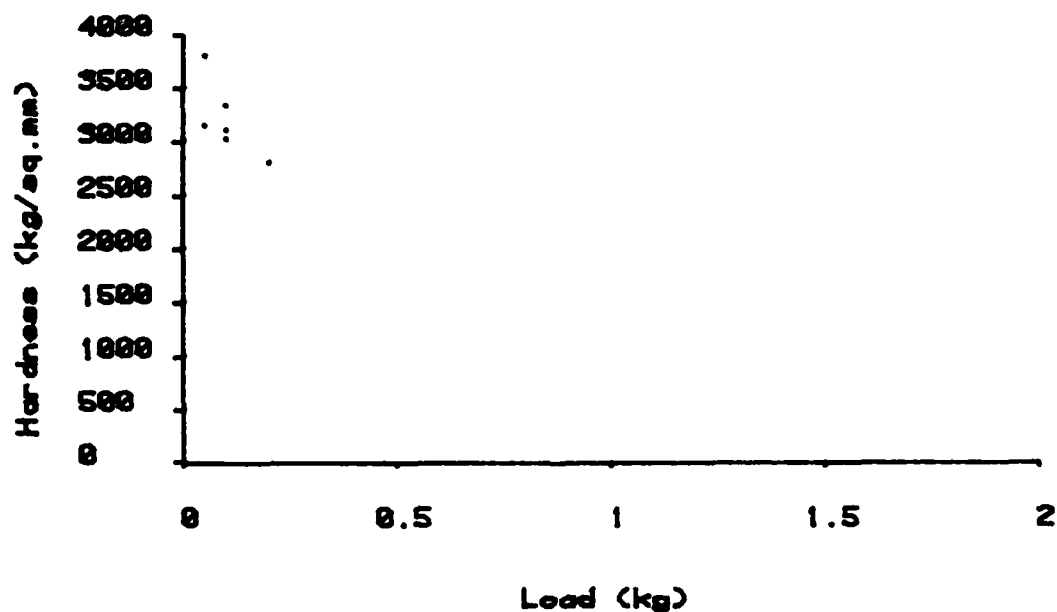


TABLE B-4. FRACTURE TOUGHNESS BY INDENTATION
FOR FLEXURE SPECIMEN HW-4-200-3

Indent	Indentation	Hardness		K _{Ic} (MN/m ^{0.5})					
		Load (kg)	kg/mm ²	3N/mm	1	2	3	4	Ave.
1	0.05	3182.	31.81	0.00	0.00	0.00	0.00	0.00	0.00
2	0.05	3812.	37.36	0.00	0.00	0.00	0.00	0.00	0.00
3	0.05	3812.	37.36	0.00	0.00	0.00	0.00	0.00	0.00
4	0.10	3098.	30.99	0.00	0.00	0.00	0.00	0.00	0.00
5	0.10	3345.	32.68	0.00	0.00	0.00	0.00	0.00	0.00
6	0.10	3023.	29.64	2.78	2.31	2.75	3.38	2.77	0.41
7	0.20	2891.	27.47	3.81	3.25	2.97	0.00	3.08	0.15



**APPENDIX C
COMPILED OF FLEXURE STRESS-STRAIN
DATA ON FLEXURE SPECIMENS
FROM DEPOSITION HW-4-139**

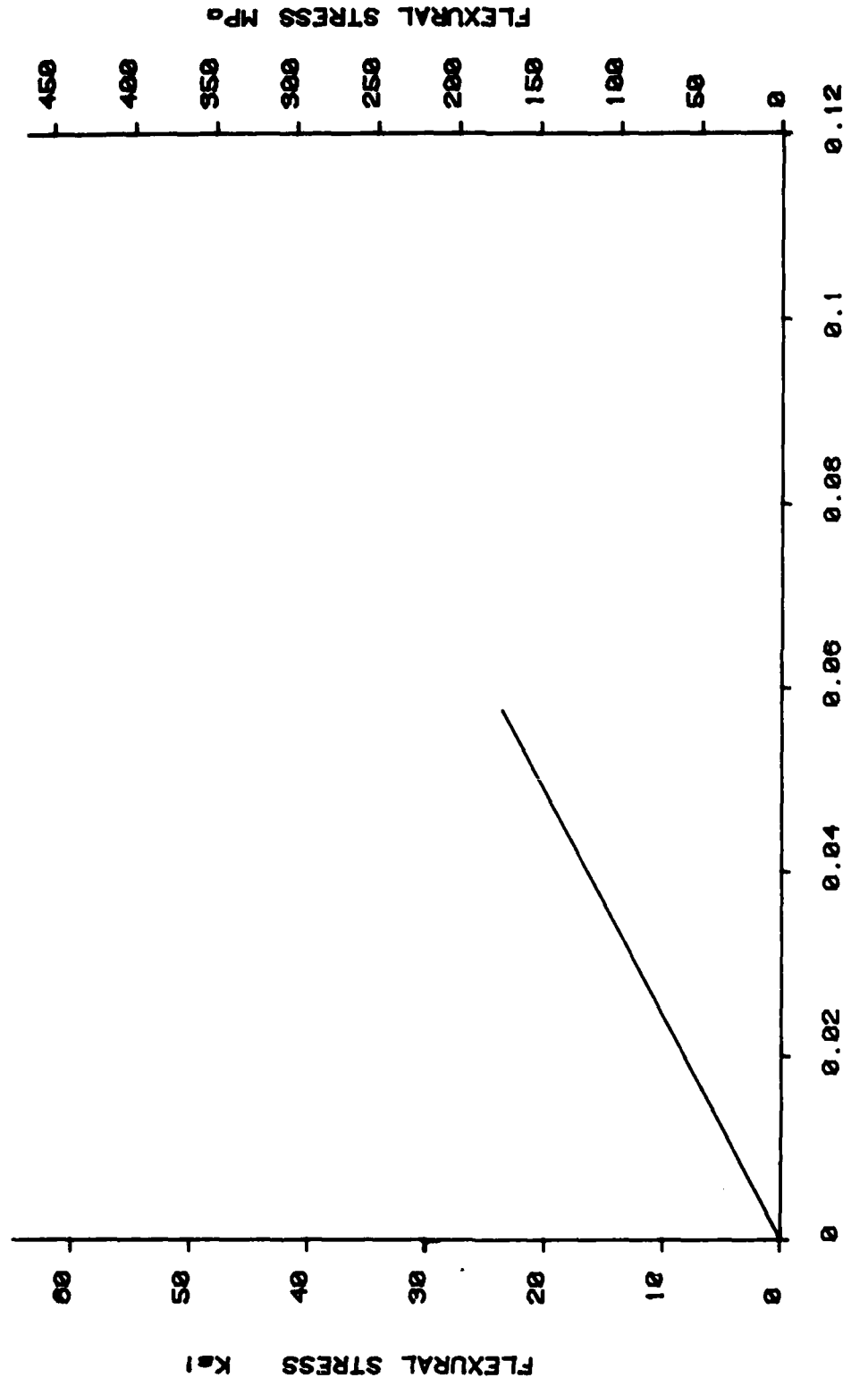


Figure C-1. Flexure Stress - Strain Behavior of Flexure Specimen HW-4-139-B3
 MOR = 162.58 MPa (23.58 ksi), Fracture Strain = 0.058%,
 Elastic Modulus = 282.82 GPa (41.02 Mpsi), T = 25°C

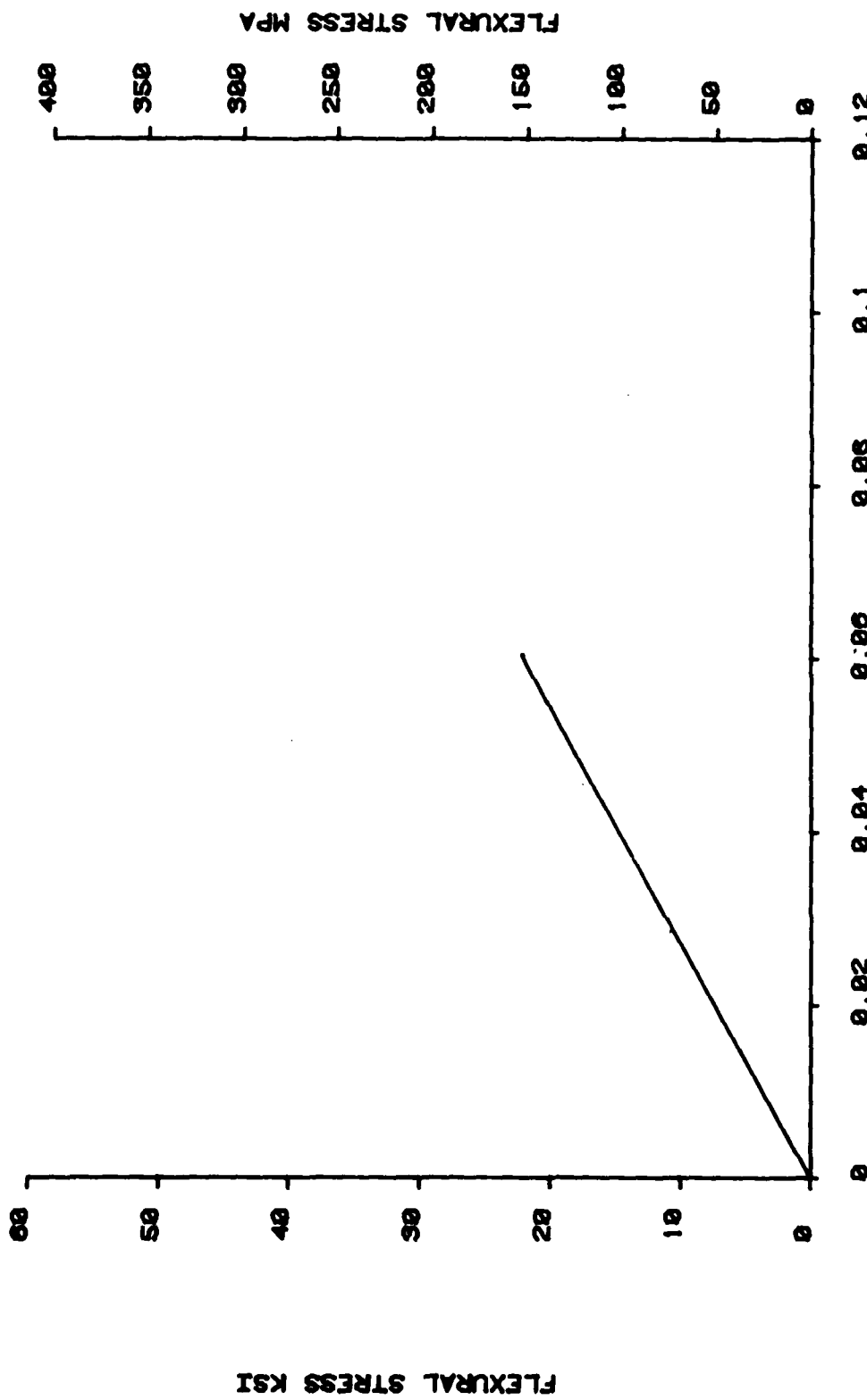


Figure C-2. Flexure Stress-Strain Behavior of Flexure Specimen HW-4-139-B5.
 MOR = 156.23 Mpa (22.66 kpsi), Fracture Strain = 0.061%,
 Elastic Modulus = 249.45GPa(36.15 Mpsi), T=25°C

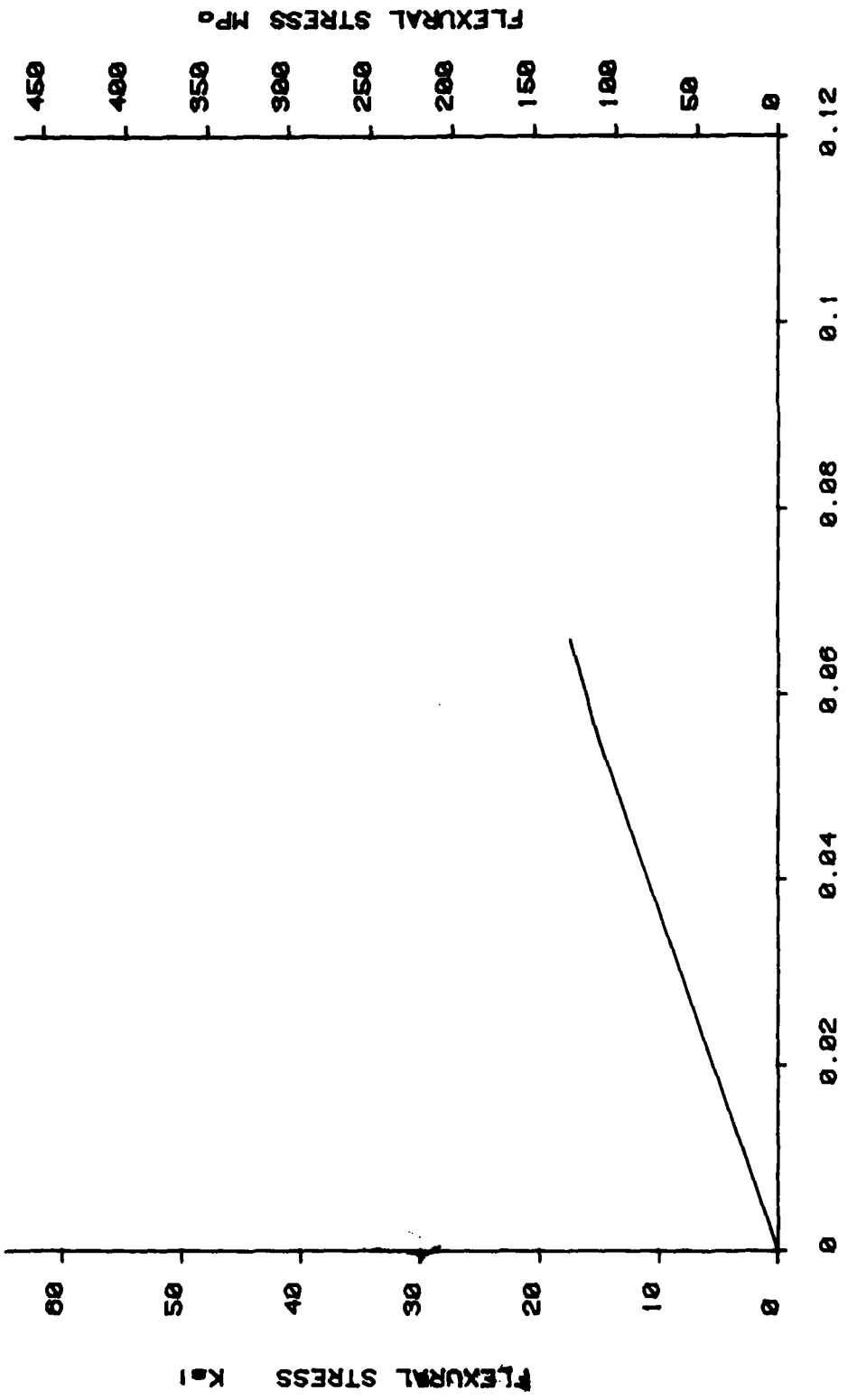


Figure C-3. Flexure Stress-Strain Behavior of Flexure Specimen HW-4-139-G3
 MOR = 120.52 MPa (17.48 kpsi), Fracture Strain = 0.0667%,
 Elastic Modulus = 187.54 GPa (27.20 Mpsi), T = 25°C.

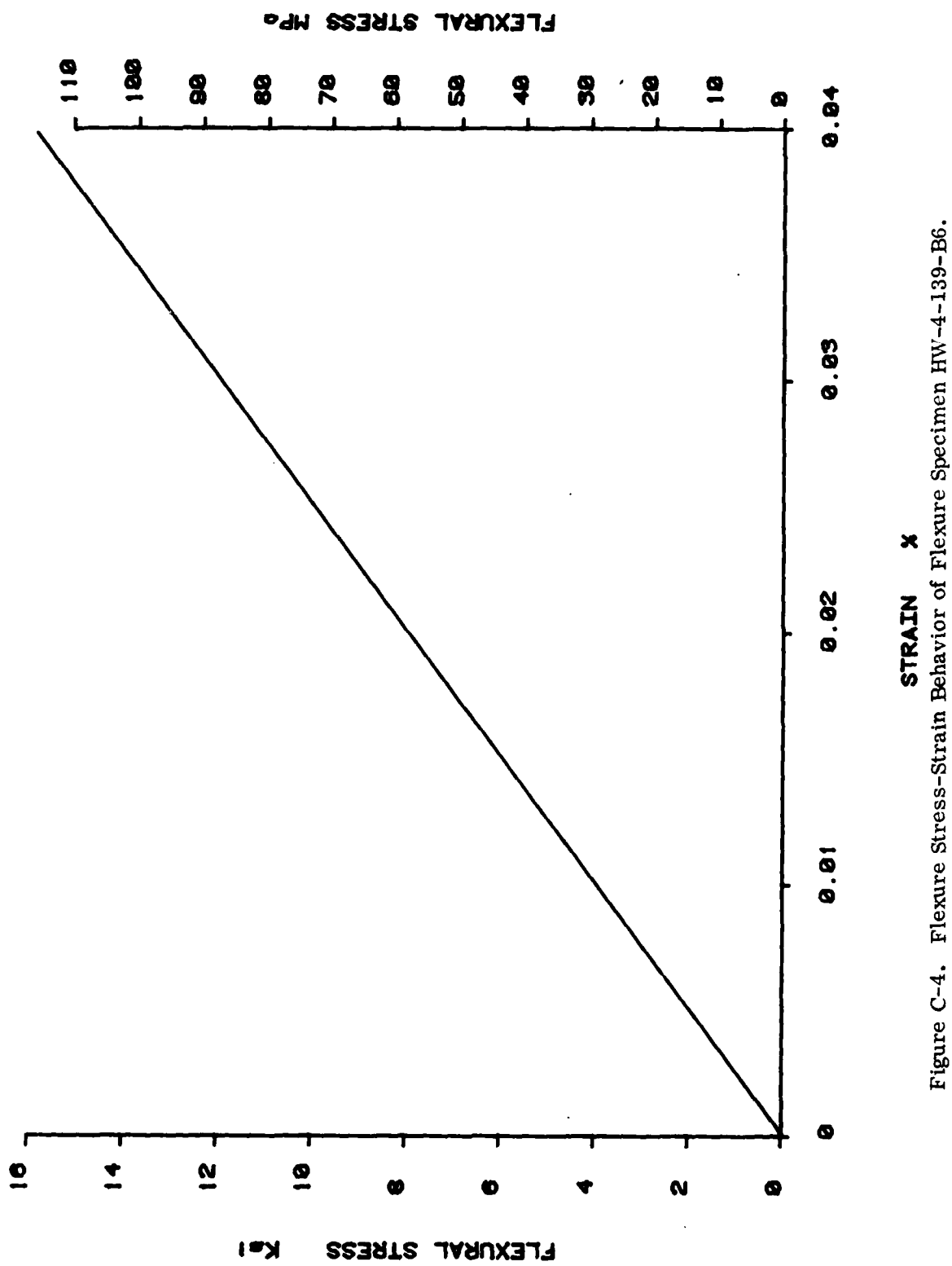


Figure C-4. Flexure Stress-Strain Behavior of Flexure Specimen HW-4-139-B6.
 MOR = 109.63 MPa (15.9 kpsi), Fracture Strain = 0.04%,
 Elastic Modulus = 275.38 GPa (39.94 MPsi) T = 1000°C

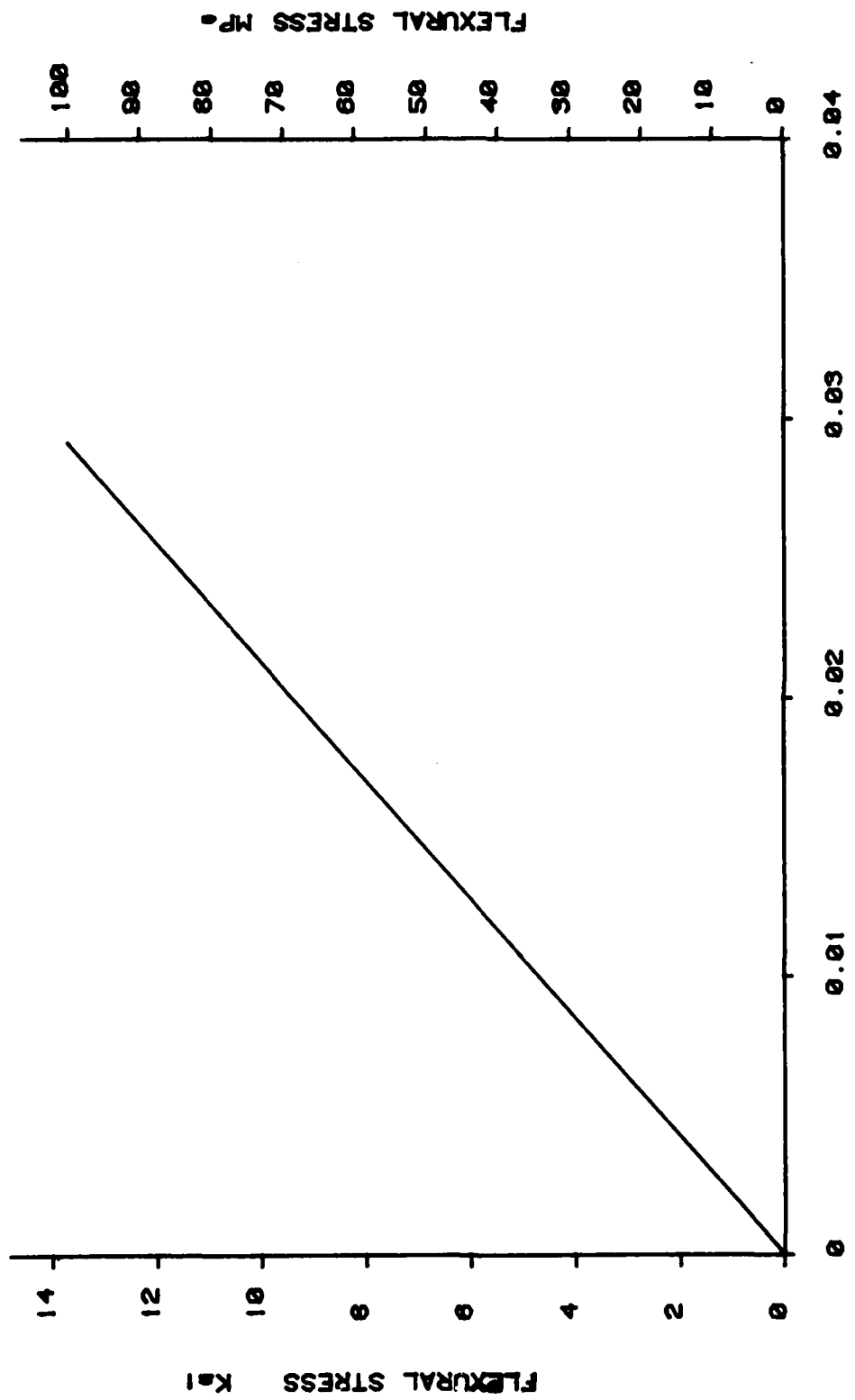


Figure C-5. Flexure Stress-Strain Behavior of Flexure Specimen HW-4-139-G-4.
 MOR = 94.46 MPa (13.7 kpsi), Fracture Strain = 0.03%,
 Elastic Modulus = 334.88 GPa (48.57 Mpsi), T = 1000°C.

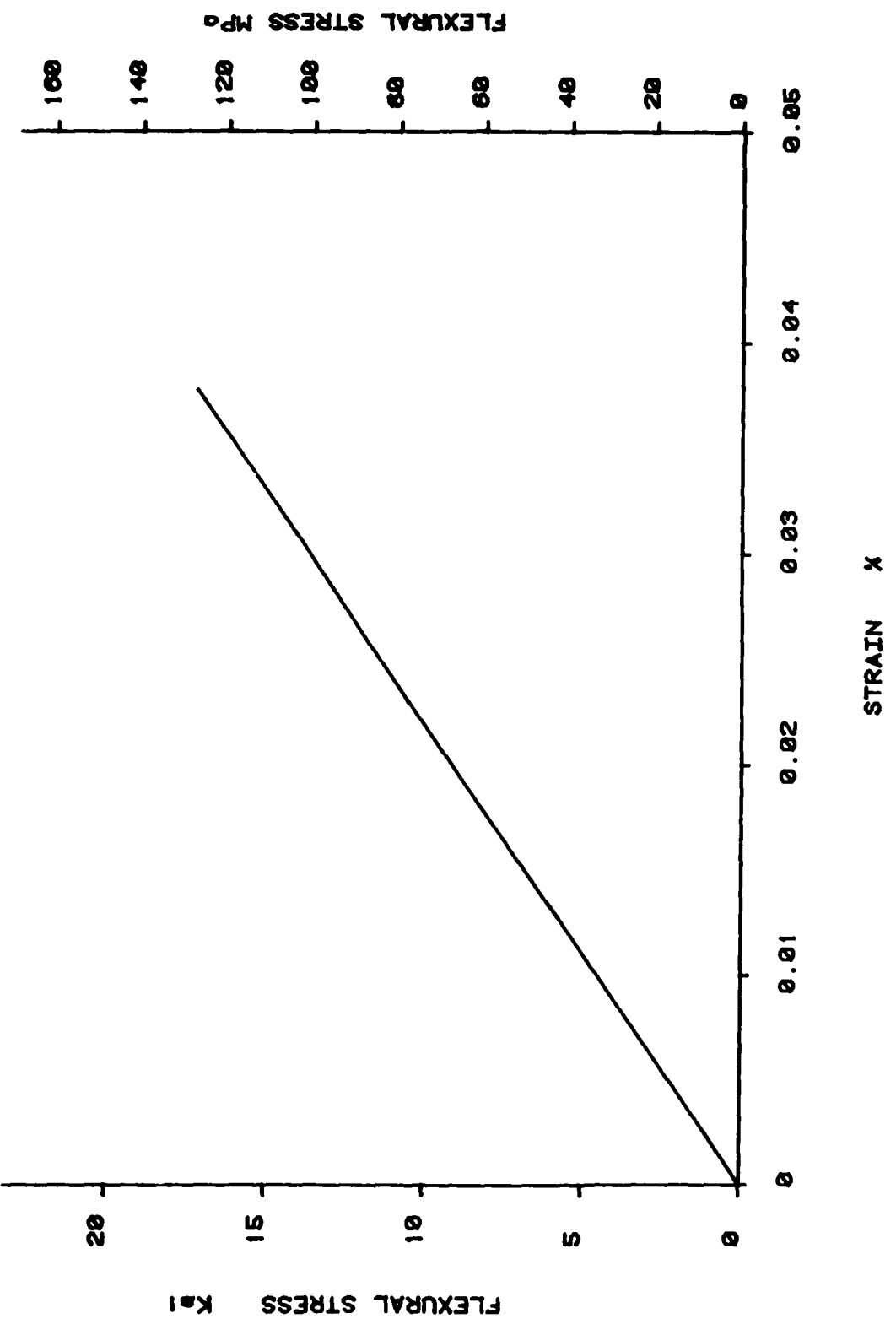


Figure C-6. Flexure Stress-Strain Behavior of Flexure Specimen HW-4-139-B1
 MOR = 118.18 MPa (17.14 kpsi), Fracture Strain = 0.040%,
 Elastic Modulus = 332.88 GPa (48.28 Mpsi). T = 1400°C.

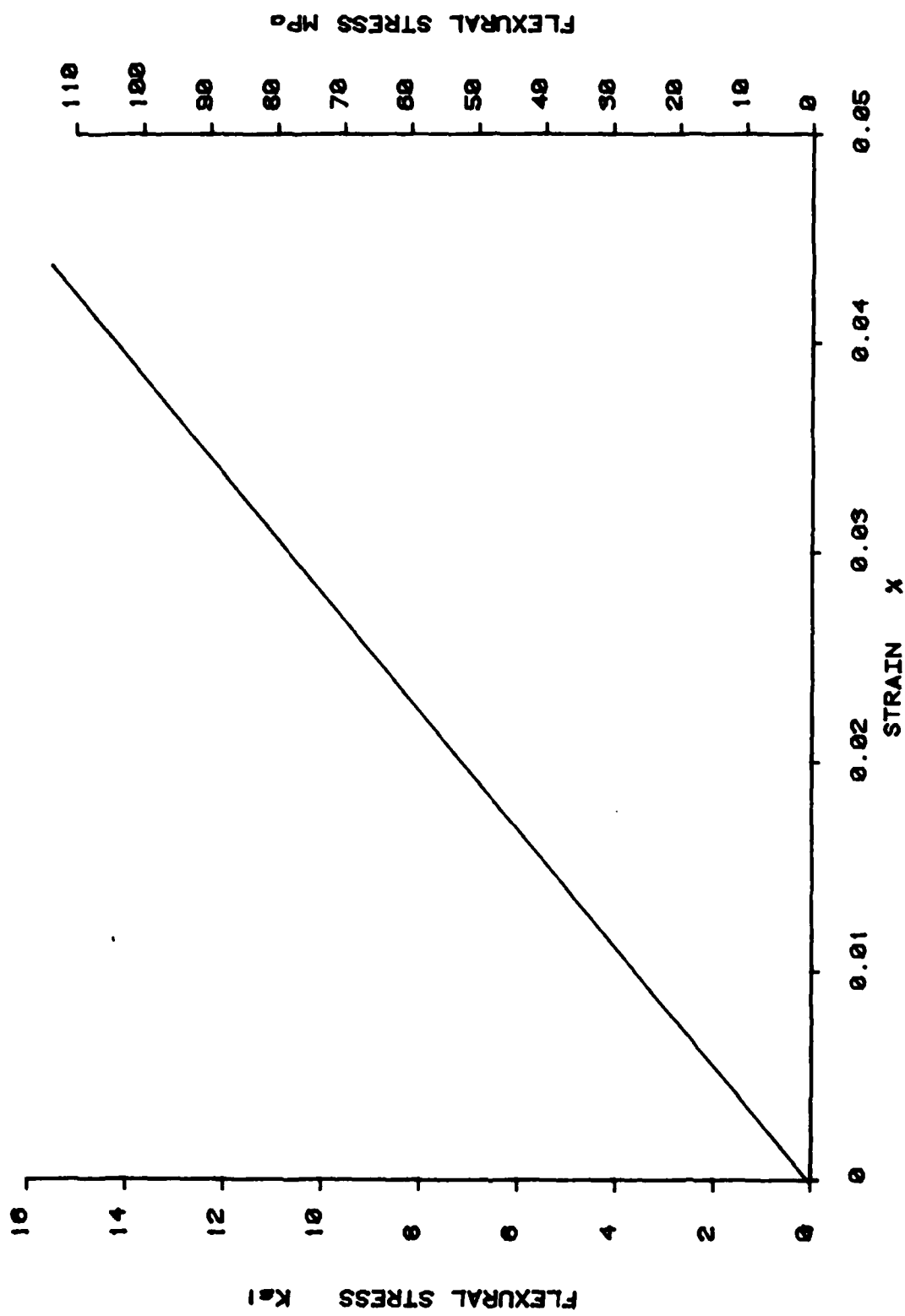


Figure C-7. Flexure Stress-Strain Behavior of Flexure Specimen HW-4-139-B2.
 MOR = 107.21 MPa (15.55 ksi), Fracture Strain = 0.040 ϵ_r ,
 Elastic Modulus = 247.16 GPa (35.87 ksi), T = 1400°C.

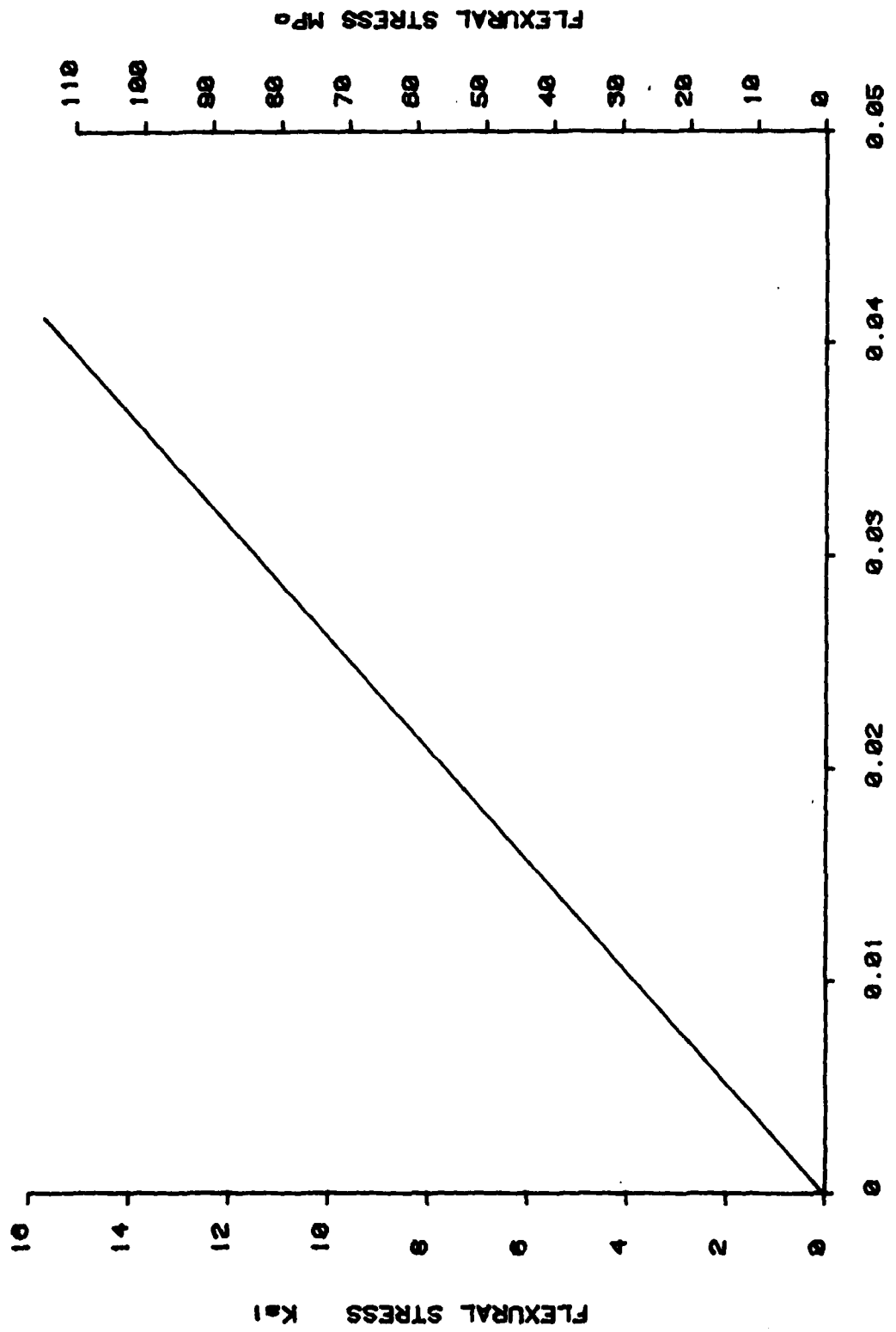


Figure C-8. Flexure Stress-Strain Behavior of Flexure Specimen HW-4-139-G2.
 MOR = 108.39 MPa (15.55 kpsi), Fracture Strain = 0.040%,
 Elastic Modulus = 263.72 GPa (38.25 Mpsi), T = 1400°C.

**APPENDIX D
TRIAL MICROETCHING RESULTS
ON SELECTED Si₃N₄ SAMPLES**

APPENDIX D

TRIAL MICROETCHING RESULTS ON SELECTED Si₃N₄ SAMPLES

D.1 SUMMARY:

Fused salt and mixed acid etchants were used to attempt etching of Si₃N₄ samples. The fused salt etchant selectively etched the voids and second phases present in the microsection rather than the Si₃N₄.

The mixed acid was most effective when operated at 300° C. The mixed acid was selective with respect to color of the Si₃N₄ deposit, where significant microetching was observed for a white material, but a brown material was totally resistant to chemical attack.*

D.2 RESULTS:

This report summarizes the results of microetching experiments on four Si₃N₄ specimens. Fused salt (NaOH + KOH + LiOH) and mixed acid (H₂SO₄ + HF + NH₄F) etchants were used at various times and temperatures.

The fused salt etch caused random surface pitting with no resolution of the grain structure and has been rejected for future use.

The mixed acid bath, used at low temperatures (100° C), etched the last deposit side of 400-129 (white) after 2-1/2 hours etch time, but the edge view (through-the-thickness) required 13-1/2 hours etch time to produce a superficial etch. With mixed acid etching conditions of 1/2 hour at ~ 300° C, specimen 400-129 (white) was micro-etched sufficiently to observe grain structure and decorated grain faces. The mixed acid bath was also used on specimen 400-128 (brown). Accumulated etching of 2 hours at 100° C plus 1-1/3 hours at ~ 200° C plus 1/2 hour at ~ 300° C produced no microetching.

Table D-1, Trial Microetching Results, details the conditions for 15 microetching experiments (and one as-received examination). Figure numbers are keyed to the table.

*Note: Subsequent etching studies indicated vacuum annealing at 1600° C provided selective vaporization of Si₃N₄ resulting in good decoration of grain boundaries.

TABLE D-1

TRIAL MICROETCHING RESULTS

<u>Specimen</u>	<u>Treatment</u>	<u>Result</u>	<u>Figure No.</u>
HW-1-66	As Received	Examined using polarized light. Compared growth cones to micro-cracking. Interfaces at growth cones do not appear to be sites for microcracking.	D-1
Flexure Spec. #3, HW-4-128	Specimen "quick" polished on diamond, 15 microns to 1/4 micron. Etched in ⁽¹⁾ 7 parts H ₂ SO ₄ 2 parts HF 2 parts NH ₄ F Etched for 4 hrs. @ 100°C.	Examined using bright and oblique light, and Nomarski interference contrast. Heterogeneous grain size with various residual machining marks. Scratches show different hardness for various grains, probably due to different crystal orientation between grains ⁽²⁾ .	D-2a, b
Flexure Spec. #3, HW-4-128	Specimen repolished Etched in ⁽³⁾ 4 parts NaOH 4 parts KOH 1 part LiOH Etched for 20 min. @ 180°C.	Etchant caused random pitting of surface with no resolution of grain structure	D-3

References

D-1 "Synthesis, Characterization, and Consolidation of Si₃N₄ Obtained from Ammonolysis of SiCl₄", K.S. Mazdiyasni and C.M. Cooke, J. of American Ceramic Society, December 1973.

D-2 "Structural Studies of Surface Deformation in MgO, SiC, and Si₃N₄", O.O. Adewoye, et. al., Cambridge Univ. (Report prepared for Army R&D Group (Europe), Oct. 1974).

D-3 Personal Communication, C.D. Greskovich, GE-CRDC

Specimen	Treatment	Result	Figure No.
HW-4-166	Cut-off in low-speed saw. Etch in Fused salts, 4 parts NaOH 4 parts KOH 1 part LiOH Etch for 25 mins. @ 180°C	Examined fracture surface at 200X and 800X. Surface features at 800X were unetched. Polarized light showed a four-layered structure	D-4a, b
HW-4-128	As Received	Specimen in metallographic mount. Examined at 200X (bright field) and 240X (Nomarski interference contrast). Two "phase" features. no grain structure.	D-5a, b
HW-4-128	Etched in 7 parts H ₂ SO ₄ (9. 2pbw) 2 parts HF (2 pbw) 2 parts NH ₄ F (2 pbw) Etched 2 hrs. @ 100°C	(Specimens removed from mount before etch). Two phase structure consisting of a) unetched matrix, b) heterogeneous distribution of second "phase"	D-6
HW-4-128	Etched in 9. 2 pbw H ₂ SO ₄ 2 pbw HF 2 pbw NH ₄ F. HF Etched for 1/2 hr. @ 572F ± 6F Measured, 412F Actual	Specimen not examined	
HW-4-128	Etched in 7 pbw H ₂ SO ₄ 2. 2 pbw HF 2 pbw NH ₄ F. HF Etched for 1/2 hr. @ 572F + 6-3 Meas., 412F Actual	Two phase structure consisting of a) unetched matrix, b) heterogeneous distribution of second "phase"	D-7
HW-4-128	Etched in 7 pbw H ₂ SO ₄ 2. 2 pbw HF 2 pbw NH ₄ F. HF Etched for 23 mins. @ 551F-654F Measured 443F Actual	Same appearance at low mag. (240X) as above. Examination at 900X showed two "phase" structure, no etching, but several hexagonal etch pits were noted.	D-8

Specimen	Treatment	Result	Figure no.
HW-4-128	Etched in same bath comp. as above; etched for 1/2 hr. @ 553F - 605F Actual	No weight loss. Examination showed two "phase" unetched structure	D-9
HW-4-129	Etched in 35 cc H ₂ SO ₄ 10 cc HF 10 gm NH ₄ F Etched for 1 hr. in hot (100°C ?) acid	(Specimens removed from mount before etch). Last deposit side shows v. slight etch; edge view unetched	D-10
HW-4-129	Same etch, etched an additional 1-1/2 hrs. @ 201F	Last deposit side etched showing heterogeneous microstructure. Edge view. v. slight etch.	D-11
HW-4-129	Same etch; etched an additional 3 hrs.	Last deposit side heterogeneous grain size with decoration of grains apparent. Edge view slight etch.	D-12a, b
HW-4-129	Same etch; etched an additional 4 hrs.	Last deposit side unchanged. Edge view slight etch shows columnar + islands of equi-axed grains; second phase may be voids or etched out phase.	D-13a, b
HW-4-129	Same etch; etched an additional 4 hrs.	Last deposit side = located slight etched area.	D-14
HW-4-129	Etched in 7 pbw H ₂ SO ₄ 2.2 pbw HF 2 pbw NH ₄ F. HF Etched for 1/2 hr. @ 585F - 573F Actual	Last deposit side = Heterogeneous grain size with terrace decoration of individ. grains. Weight loss = .0001 g	D-15

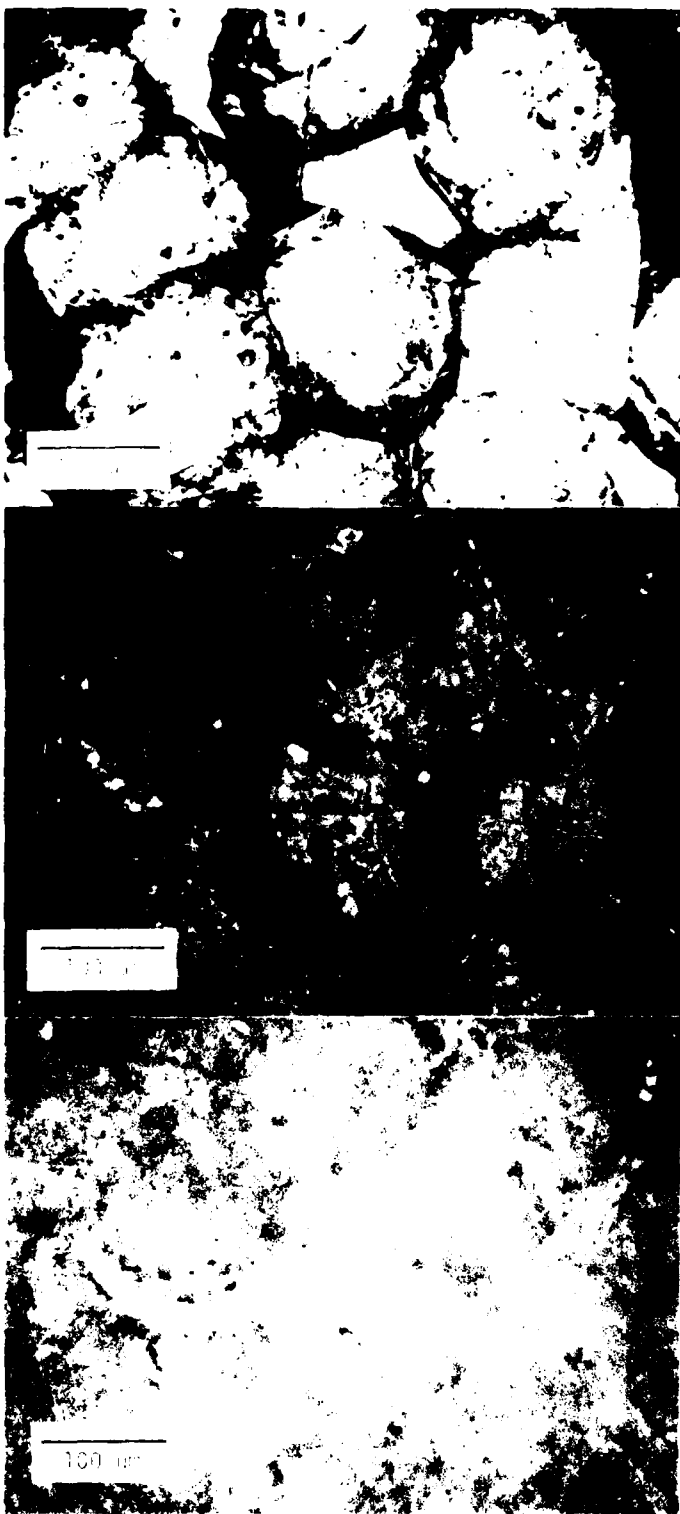
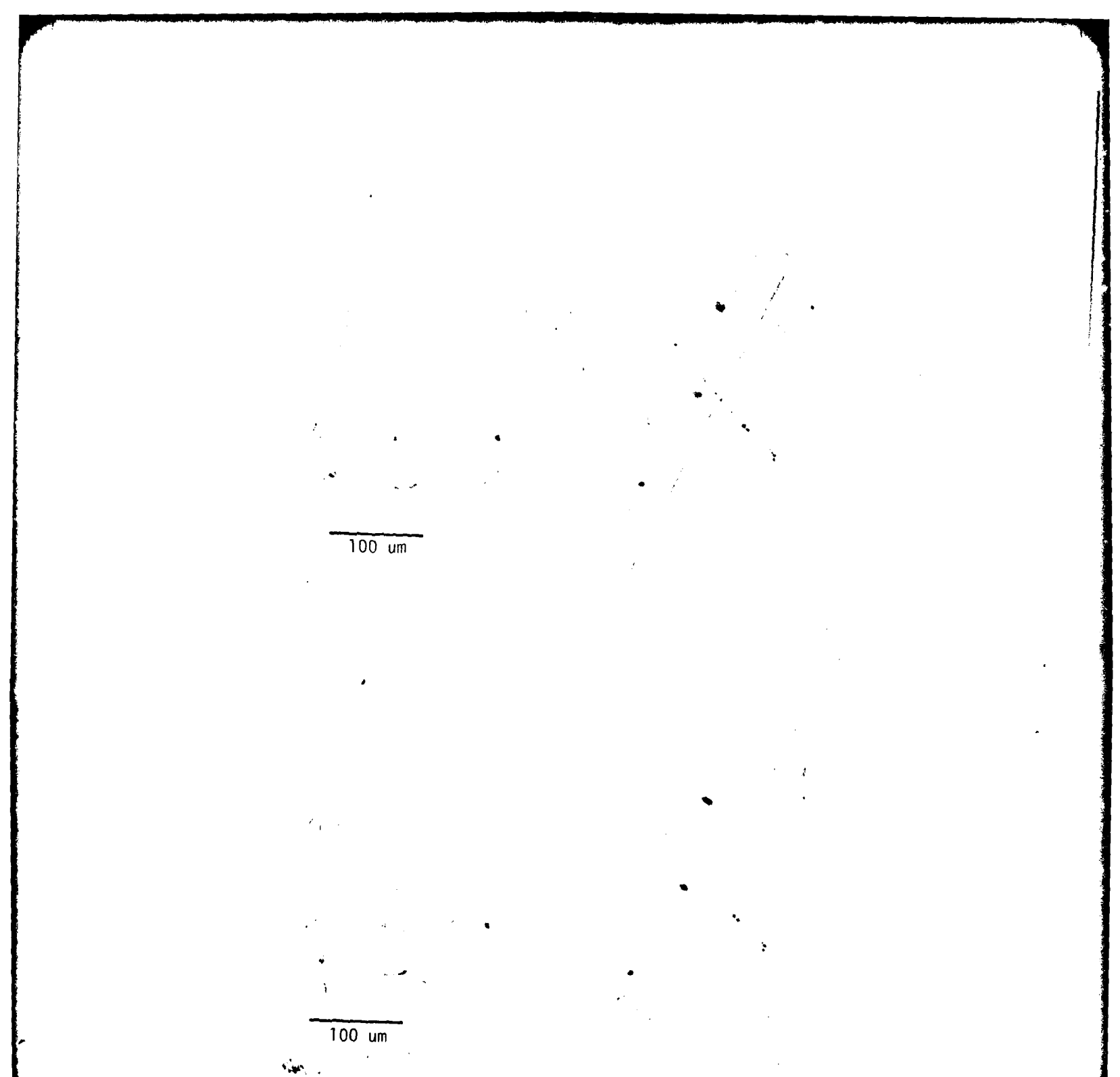
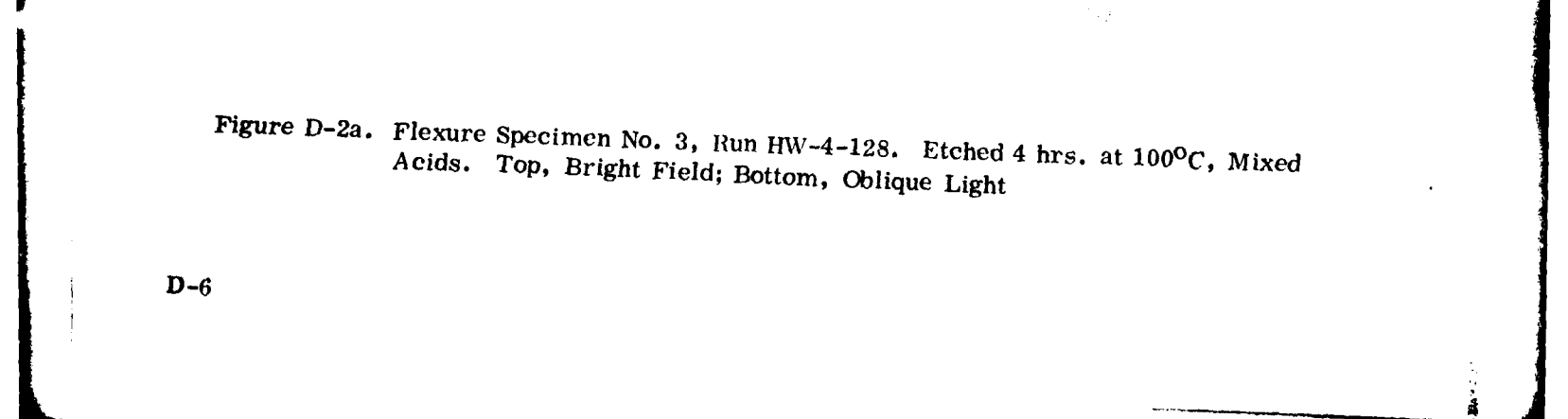


Figure D-1. As-Received Specimen of HW-1-66



100 um



100 um

Figure D-2a. Flexure Specimen No. 3, Run HW-4-128. Etched 4 hrs. at 100°C, Mixed Acids. Top, Bright Field; Bottom, Oblique Light

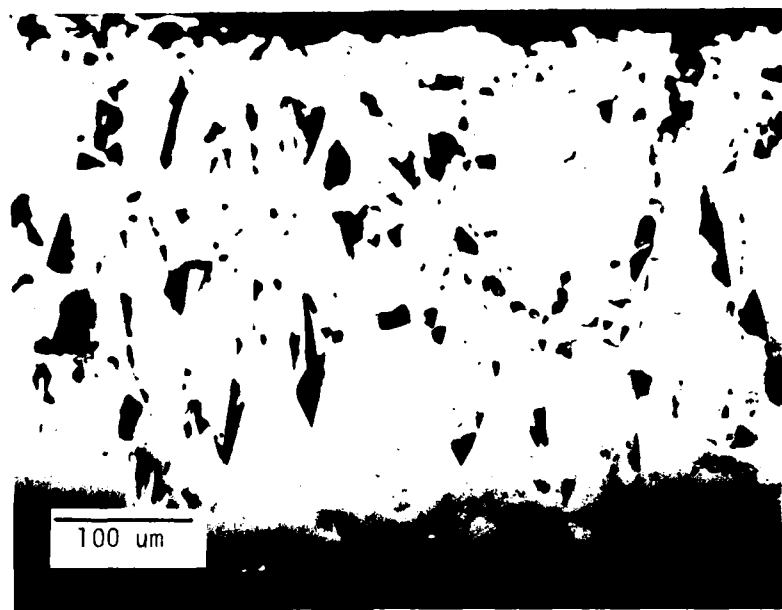


Figure D-2b. Top, Nomarski Interference Contrast; Bottom, Nomarski Interference Contrast With Monochromatic Filter

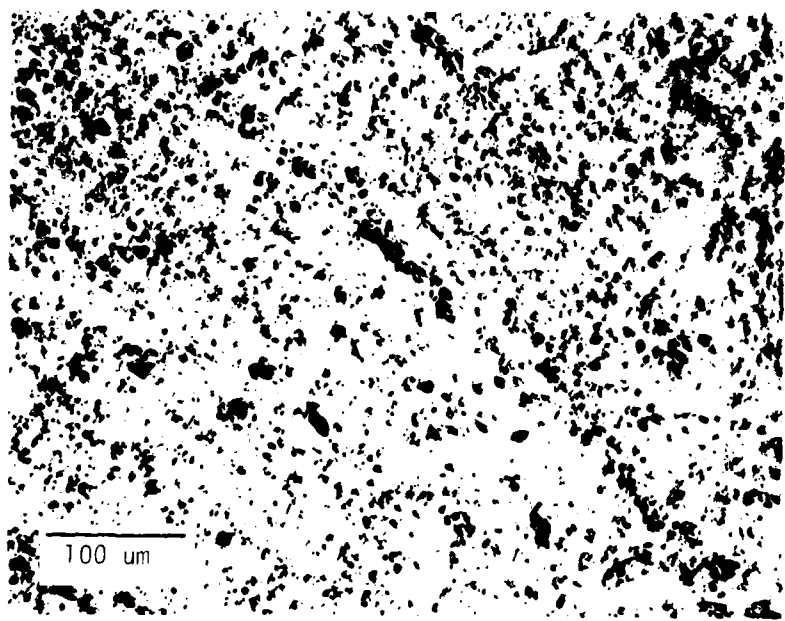


Figure D-3. Flexure Specimen No. 3, Run HW-4-128. Etched 20 min. at 180°C,
Fused Salts

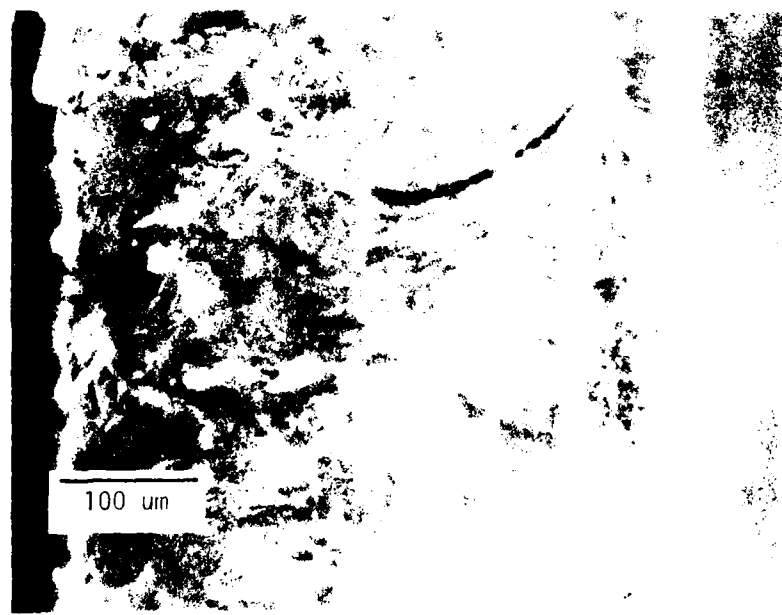
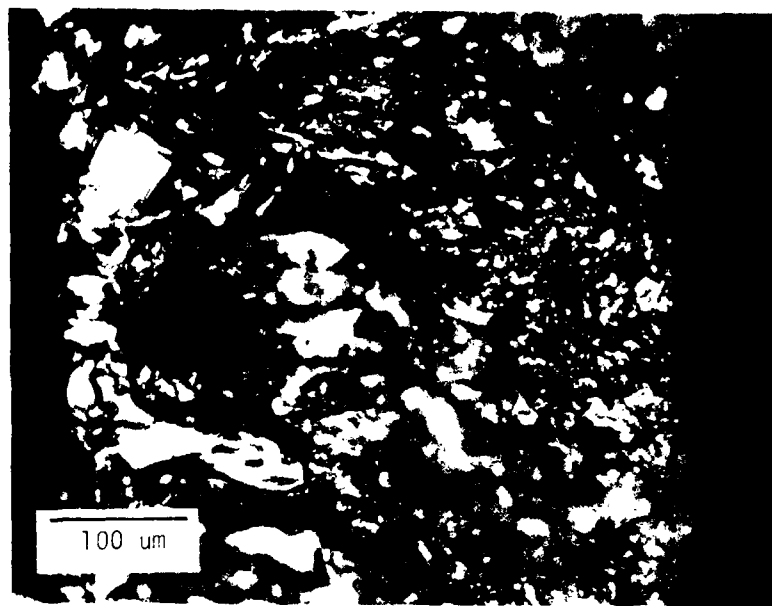


Figure D-4a. Fracture Surface Etched 25 min. at 180°C, Fused Salts. Top, Bright Field; Bottom, Polarized Light. Note Fine and Coarse Structure With Four Layers in Polarized Light Photomicrograph. Spec. HW-4-166

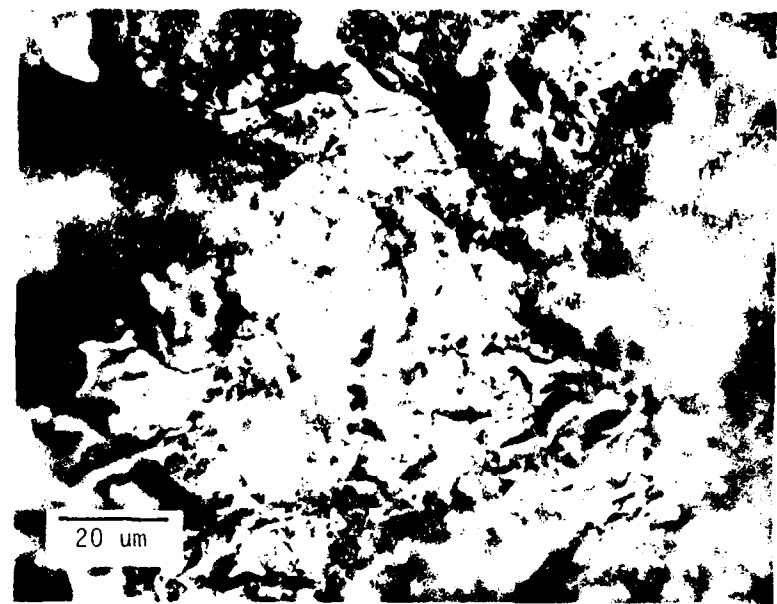


Figure D-4b. Top, Detail of "Fine" Structure, Bright Field. Bottom, Detail of "Coarse" Structure, Bright Field. Spec. No. HW-4-166

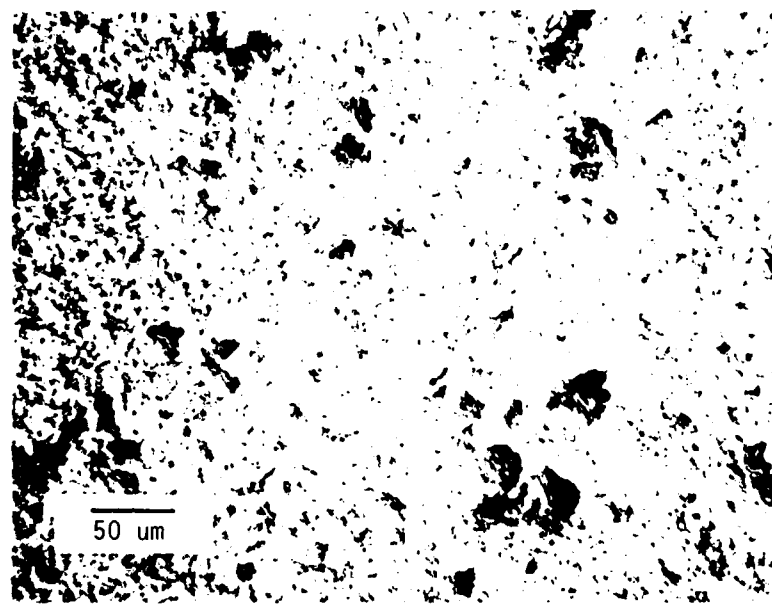
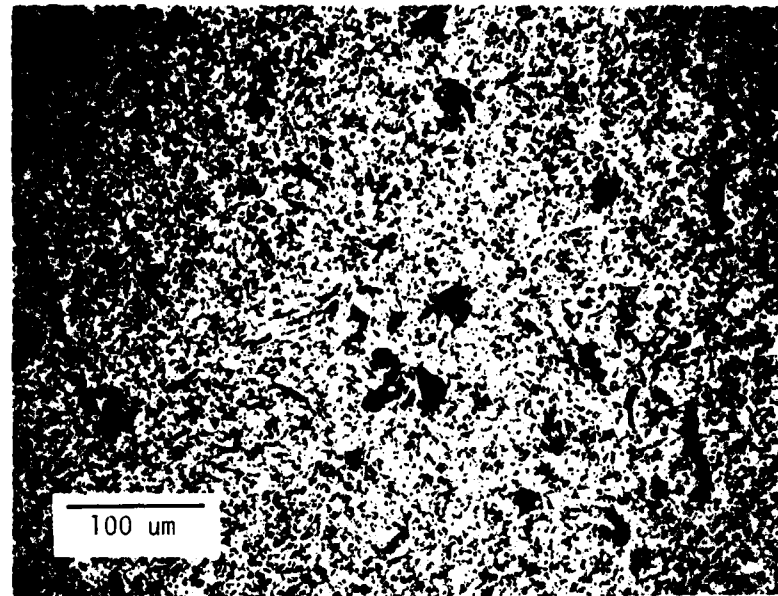


Figure D-5a. Pre-etch Condition, Last Deposit. Bright Field; Bottom, Nomarski Interference Contrast. Spec. No. HW-4-128

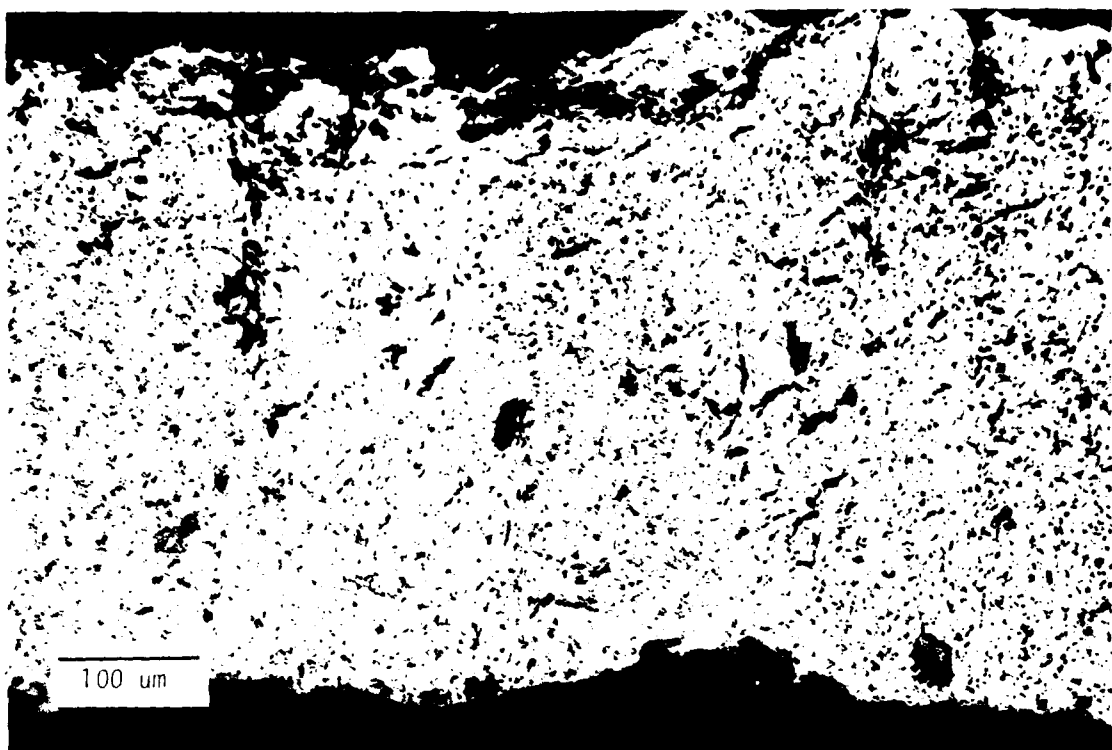


Figure D-5b. Pre-etch Condition, Edge View. Top, Montage, Bright Field; Bottom, Nomarski Interference Contrast. Spec. No. HW-4-128.

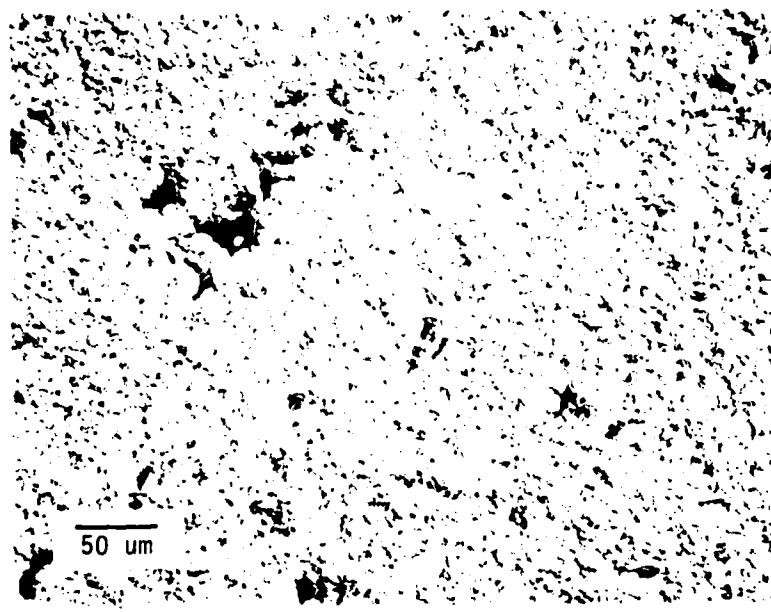
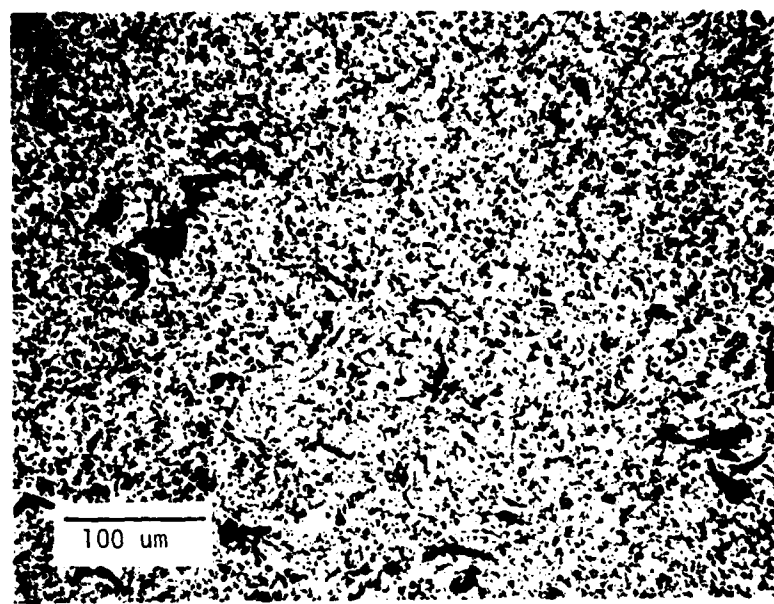


Figure D-6. Etched 2 Hours at 100°C, Mixed Acids. Top, Bright Field; Bottom, Nomarski Interference Contrast. Spec. No. HW-4-128

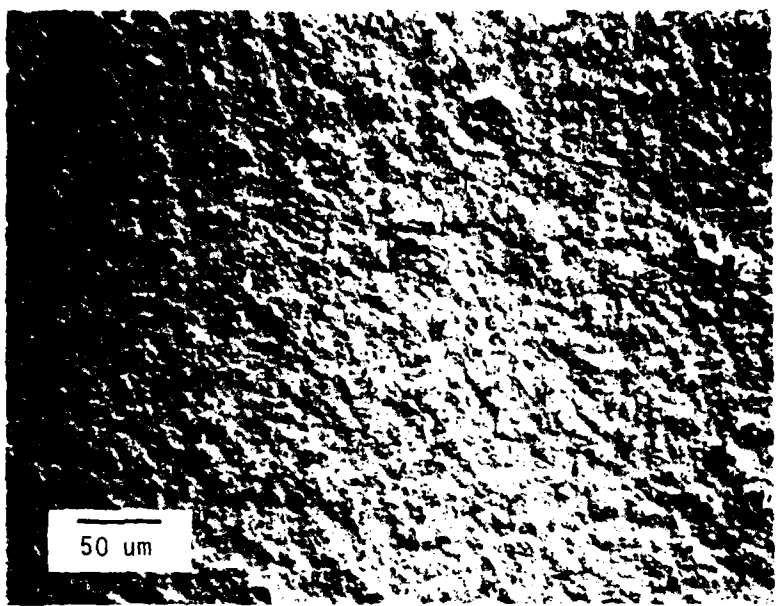


Figure D-7. 400-128. Additional Etch of 1 Hour (Total) at 412°F (211°C), Mixed Acids. Nomarski Interference Contrast. Spec. No. HW-4-128

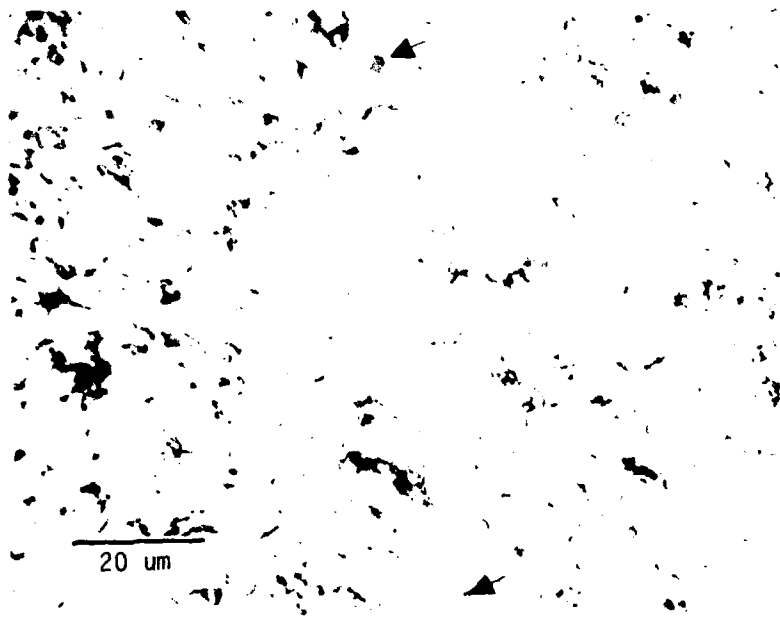


Figure D-8. Additional Etching of 23 mins. at 443°F (228°C), Mixed Acids. Note Hexagonal Etch Pits. Nomarski Interference Contrast, Spec. HW-4-128.

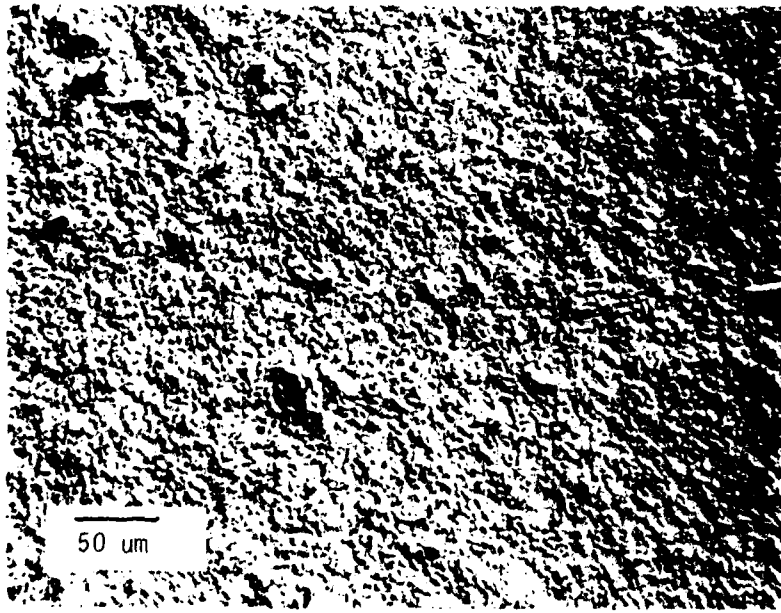


Figure D-9. After Additional Etch of 1/2 Hr. at Max. of 605°F (318°C), Mixed Acids.
Nomarski Interference Contrast. Spec. No. HW-4-128

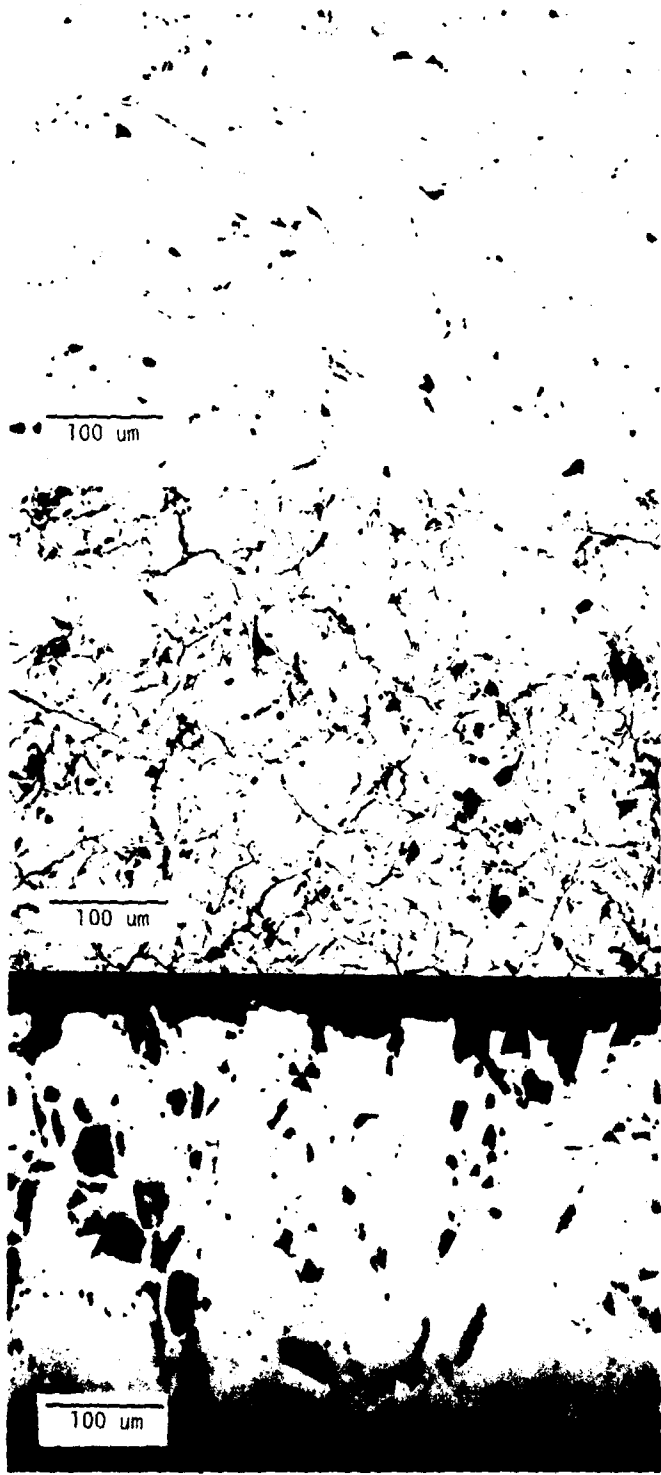


Figure D-10. Etched for 1 Hr. in "Hot" Mixed Acids. Top, Last Deposit Surface, Polished Area; Mid, Last Deposit Surface, Incomplete Polish; Bottom, Edge View. Bright Field. Spec. No. HW-4-129



Figure D-11. Additional Etch of 1-1/2 Hrs. at 201°F (94°C), Mixed Acids.
Top, Last Deposit Surface; Bottom, Edge View. Nomarski Interference
Contrast. Spec. No. HW-4-129

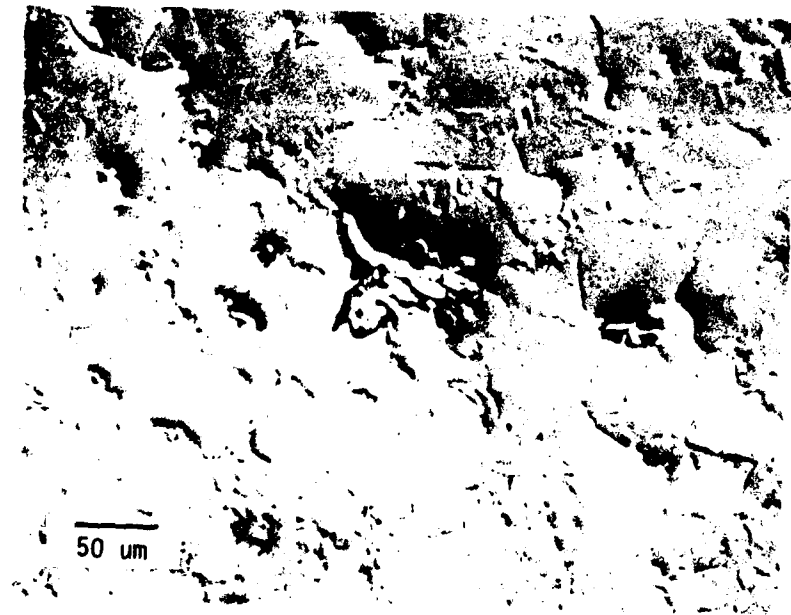
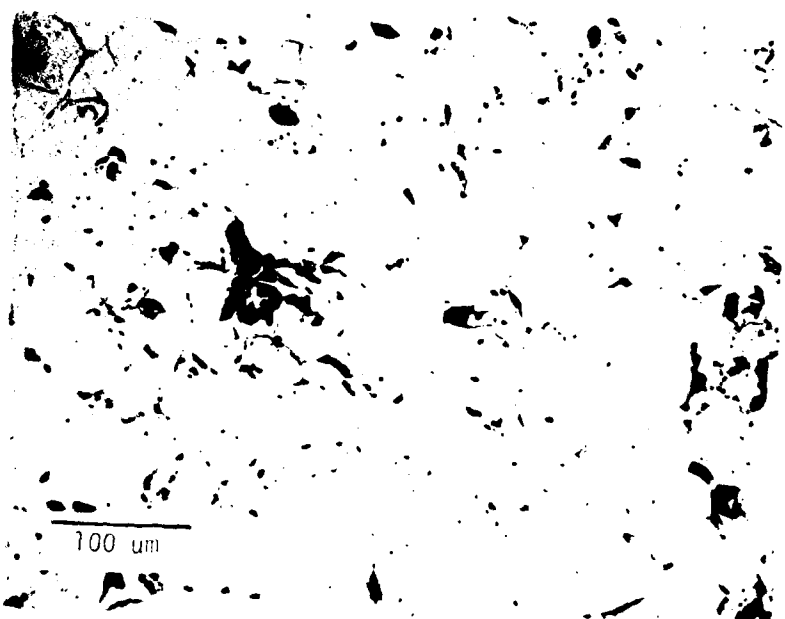


Figure D-12a. Additional Etch of 3 Hrs., Mixed Acids. Last Deposit Surface; Top, 200X Bright Field; Bottom, Nomarski Interference Contrast. Spec. No. H.v-4-129

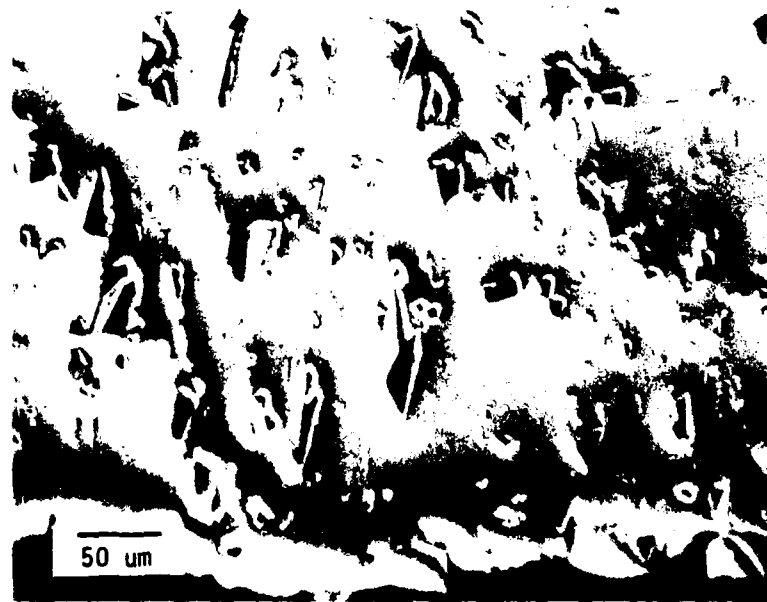
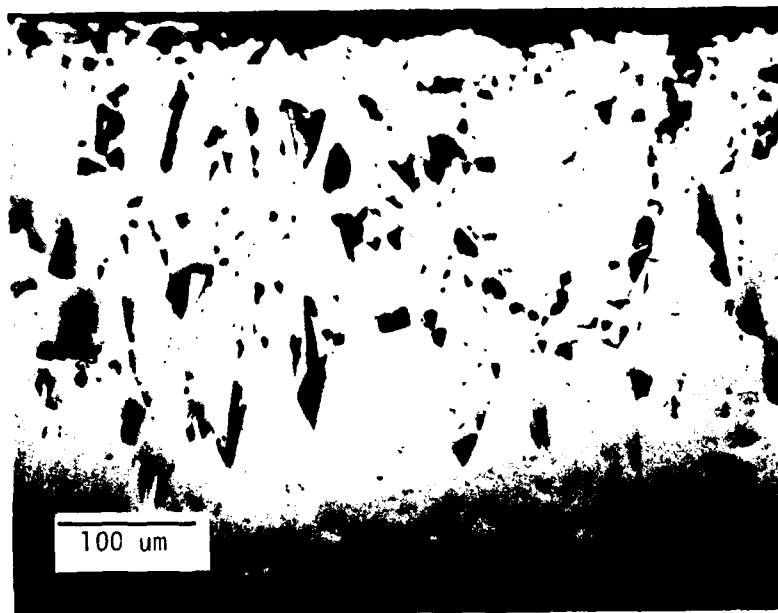


Figure D-12b. Edge View; Top, Bright Field; Bottom Nomarski Interference Contrast.
Spec. No. HW-4-129

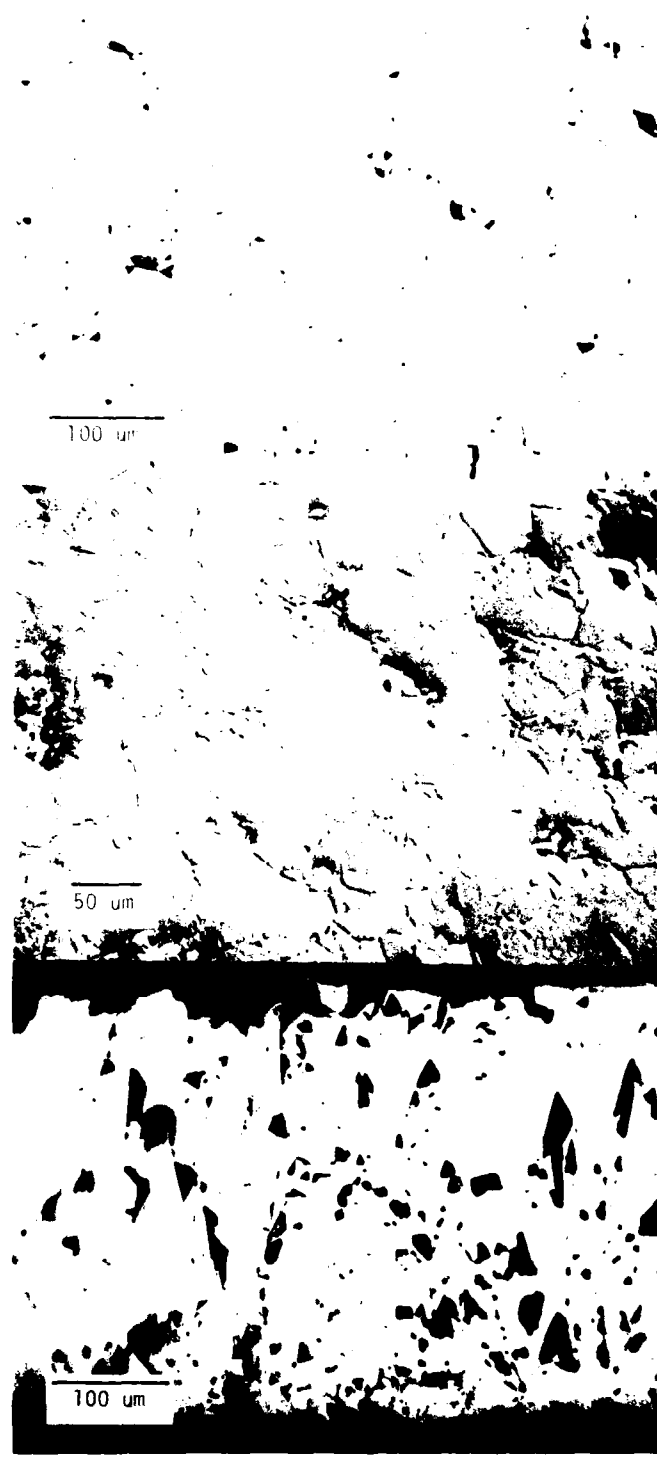
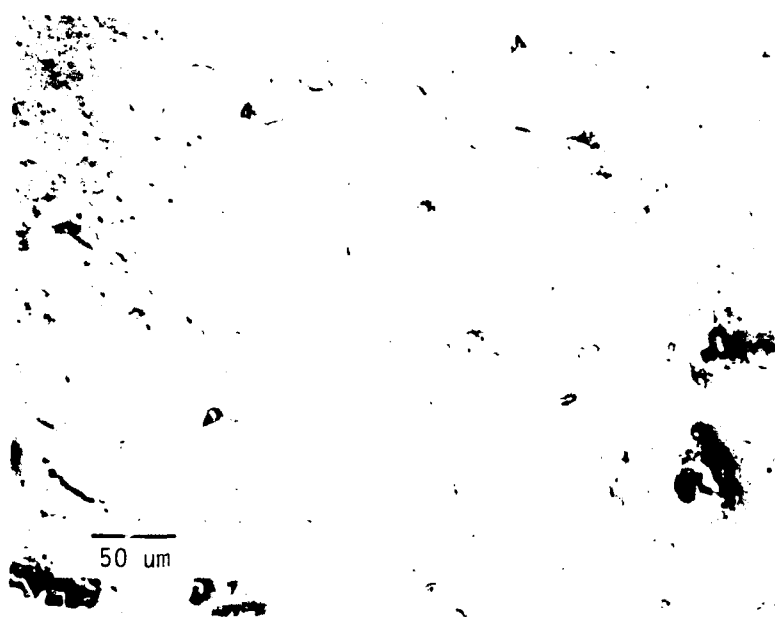
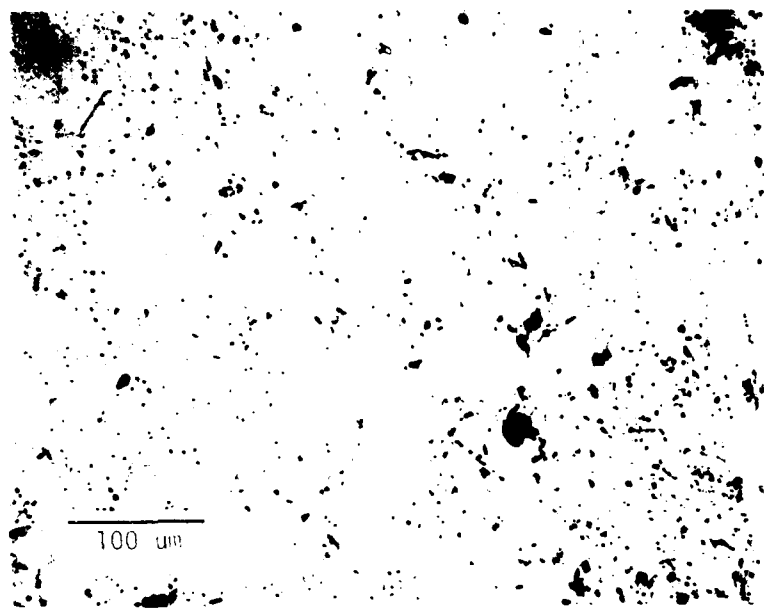


Figure D-13a. Additional Etch of 4 Hrs., Mixed Acids. Top, Last Deposit, Bright Field; Mid, Last Deposit, Nomarski Interference Contrast; Bottom, Edge View, Bright Field. Spec. No. HW-4-129

Figure D-13b. Photomontage of Edge View, Nomarski Interference Contrast. Spec No. HW-4-129





Additional Etch of 4 Hrs., Mixed Acids. Last Deposit; Top, Bright Field;
Bottom, Nomarski Interference Contrast. Spec. No. HW-4-129

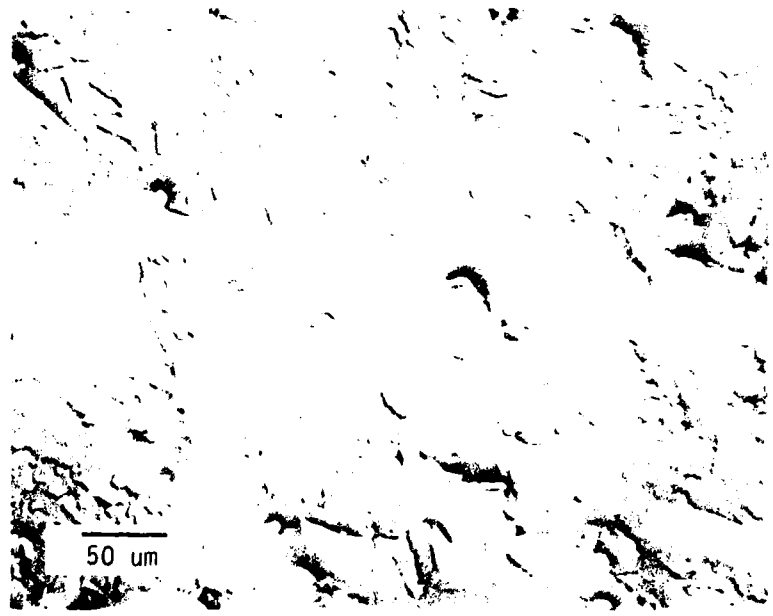


Figure D-15. Etched for 1/2 Hrs. at Maximum of 585°F (307°C), Mixed Acids.
Nomarski Interference Contrast. Spec. No. HW-4-129

BASIC DISTRIBUTION LIST

Technical and Summary Reports

<u>Organization</u>	<u>No. of Copies</u>	<u>Organization</u>	<u>No. of Copies</u>
Defense Documentation Center Cameron Station Alexandria, Virginia 22314	(12)	Naval Construction Battalion Civil Engineering Laboratory Port Hueneme, California 93043 Attn: Materials Division	(1)
Office of Naval Research Department of the Navy Arlington, Virginia 22217 Attn: Code 471 Code 102 Code 470	(3) (1) (1)	Naval Electronics Laboratory Center San Diego, California 92152 Attn: Electron Materials Sciences Division	(1)
Commanding Officer Office of Naval Research Branch Office 495 Summer Street Boston, Massachusetts 02210	(1)	Naval Missile Center Materials Consultant Code 3312-1 Point Mugu, California 93041	(1)
Commanding Officer Office of Naval Research Branch Office 536 South Clark Street Chicago, Illinois 60605	(1)	Commanding Officer Naval Surface Weapons Center White Oak Laboratory Silver Spring, Maryland 20910 Attn: Library	(1)
Office of Naval Research San Francisco Area Office 760 Market Street, Room 447 San Francisco, California 94102 Attn: Dr. P.A. Miller	(1)	David W. Taylor Naval Ship R&D Center Materials Department Annapolis, Maryland 21402	(1)
Naval Research Laboratory Washington, D.C. 20390 Attn: Code 6000 Code 6100 Code 6300 Code 6400 Code 2627	(1) (1) (1) (1) (1)	Naval Undersea Center San Diego, California 92132 Attn: Library Naval Underwater System Center Newport, Rhode Island 02840 Attn: Library	(1) (1)
Naval Air Development Center Code 302 Warminster, Pennsylvania 18974 Attn: Mr. F.S. Williams	(1)	Naval Weapons Center China Lake, California 93555 Attn: Library Naval Postgraduate School Monterey, California 93940 Attn: Mechanical Engineering Dept.	(1) (1)
Naval Air Propulsion Test Center Trenton, New Jersey 08628 Attn: Library	(1)	Naval Air Systems Command Washington, D.C. 20360 Attn: Code 52031 Code 52032 Code 320	(1) (1) (1)

BASIC DISTRIBUTION LIST (Cont'd)

<u>Organization</u>	<u>No. of Copies</u>	<u>Organization</u>	<u>No. of Copies</u>
Naval Sea System Command Washington, D.C. 20362 Attn: M. Kinna, Code 035	(1)	NASA Headquarters Washington, D.C. 20546 Attn: Code RRM	(1)
Naval Facilities Engineering Command Alexandria, Virginia 22331 Attn: Code 03	(1)	NASA Lewis Research Center 21000 Brookpark Road Cleveland, Ohio 44135 Attn: Library	
Scientific Advisor Commandant of the Marine Corps Washington, D.C. 20380 Attn: Code AX	(1)	National Bureau of Standards Washington, D.C. 20234 Attn: Metallurgy Division Inorganic Materials Division	(1) (1)
Naval Ship Engineering Center Department of the Navy CTR BG #2 3700 East-West Highway Prince Georges Plaza Hyattsville, Maryland 20782 Attn: Engineering Materials and Services Office, Code 6101	(1)	Defense Metals and Ceramics Information Center Battelle Memorial Institute 505 King Avenue Columbus, Ohio 43201	(1)
Army Research Office Box CM, Duke Station Durham, North Carolina 27706 Attn: Metallurgy & Ceramics Div.	(1)	Director Ordnance Research Laboratory P.O. Box 30 State College, Pennsylvania 16801	(1)
Army Materials and Mechanics Research Center Watertown, Massachusetts 02172 Attn: Res. Programs Office (AMXMR-P)	(1)	Director Applied Physics Laboratory University of Washington 1013 Northeast Fortieth Street Seattle, Washington 98105	(1)
Air Force Office of Scientific Research Bldg. 410 Bolling Air Force Base Washington, D.C. 20332 Attn: Chemical Science Directorate (1) Electronics and Solid State Sciences Directorate	(1)	Metals and Ceramics Division Oak Ridge National Laboratory P.O. Box X Oak Ridge, Tennessee 37380	(1)
Air Force Materials Lab (LA) Wright-Patterson AFB Dayton, Ohio 45433	(1)	Los Alamos Scientific Laboratory P.O. Box 1663 Los Alamos, New Mexico 87544 Attn: Report Librarian	(1)
		Argonne National Laboratory Metallurgy Division P.O. Box 229 Lemont, Illinois 60439	(1)

BASIC DISTRIBUTION LIST (Cont'd)

<u>Organization</u>	<u>No. of</u> <u>Copies</u>	<u>Organization</u>	<u>No. of</u> <u>Copies</u>
Brookhaven National Laboratory Technical Information Division Upton, Long Island New York 11973 Attn: Research Library	(1)	Library Building 50 Room 134 Lawrence Radiation Laboratory Berkeley, California	(1)

SUPPLEMENTARY DISTRIBUTION LIST

Technical and Summary Reports

<u>Organization</u>	<u>No. of Copies</u>	<u>Organization</u>	<u>No. of Copies</u>
Dr. W.F. Adler Effects Technology Inc. 5383 Hollister Avenue P.O. Box 30400 Santa Barbara, CA 92105	(1)	Professor A.H. Heuer Case Western Reserve University University Circle Cleveland, OH 44106	(1)
Dr. G. Bansal Battelle 505 King Avenue Columbus, OH 43201	(1)	Dr. R. Hoagland Battelle 505 King Avenue Columbus, OH 43201	(1)
Dr. R. Bratton Westinghouse Research Lab. Pittsburgh, PA 15235	(1)	Dr. R. Jaffee Electric Power Research Institute Palo Alto, CA	(1)
Dr. A.G. Evans Rockwell International P.O. Box 1085 1049 Camino Dos Rios Thousand Oaks, CA 91360	(1)	Dr. P. Jorgensen Stanford Research Institute Poulter Laboratory Menlo Park, CA 94025	(1)
Mr. E. Fisher Ford Motor Co. Dearborn, MI	(1)	Dr. R.N. Katz Army Materials and Mechanics Research Center Watertown, MA 02171	(1)
Dr. P. Gielisse University of Rhode Island Kingston, RI 02881	(1)	Dr. H. Kirchner Ceramic Finishing Company P.O. Box 498 State College, PA 16801	(1)
Dr. M.E. Gulden International Harvester Company Solar Division 2200 Pacific Highway San Diego, CA 92138	(1)	Dr. B. Koepke Honeywell, Inc. Corporate Research Center 500 Washington Avenue, South Hopkins, MN 55343	(1)
Dr. D.P.H. Hasselman Montana Energy and MHD Research and Development Institute P.O. Box 3809 Butte, Montana 59701	(1)	Mr. Frank Koubek Naval Surface Weapons Center White Oak Laboratory Silver Spring, MD 20910	(1)
Mr. G. Hayes Naval Weapons Center China Lake, CA 93555	(1)	E. Krafft Carborundum Co. Niagara Falls, NY	(1)

SUPPLEMENTARY DISTRIBUTION LIST (Cont'd)

<u>Organization</u>	<u>No. of Copies</u>	<u>Organization</u>	<u>No. of Copies</u>
Dr. F.F. Lange Rockwell International P.O. Box 1085 1049 Camino Dos Rios Thousand Oaks, CA 91360	(1)	Dr. J. Ritter University of Massachusetts Department of Mechanical Engineering Amherst, MA 01002	(1)
Dr. J. Lankford Southwest Research Institute 8500 Culebra Road San Antonio, TX 78284	(1)	Professor R. Roy Pennsylvania State University Materials Research Laboratory University Park, PA 16802	(1)
Library Norton Company Industrial Ceramics Division Worcester, MA 01606	(1)	Dr. R. Ruh AFML Wright-Patterson AFB Dayton, OH 45433	(1)
State University of New York College of Ceramics at Alfred University Attn: Library Alfred, NY 14802	(1)	Mr. J. Schuldies AiResearch Phoenix, AZ	(1)
Dr. L. Hench University of Florida Ceramics Division Gainesville, FL 32601	(1)	Professor G. Sines University of California, Los Angeles Los Angeles, CA 90024	(1)
Dr. N. MacMillan Materials Research Laboratory Pennsylvania State University College Park, PA 16802	(1)	Dr. N. Tallan AFML Wright-Patterson AFB Dayton, OH 45433	(1)
Mr. F. Markarian Naval Weapons Center China Lake, CA 93555	(1)	Dr. T. Vasilos AVCO Corporation Research and Advanced Development Division 201 Lowell Street Wilmington, MA 01887	(1)
Dr. Perry A. Miles Raytheon Company Research Division 28 Seyon Street Waltham, MA 02154	(1)	Mr. J.D. Walton Engineering Experiment Station Georgia Institute of Technology Atlanta, GA 30332	(1)
Mr. R. Rice Naval Research Laboratory Code 6360 Washington, D.C. 20375	(1)	Dr. S.M. Widerhorn Inorganic Materials Division National Bureau of Standards Washington, DC 20234	(1)

SUPPLEMENTARY DISTRIBUTION LIST (Cont'd)

<u>Organization</u>	<u>No. of Copies</u>	<u>Organization</u>	<u>No. of Copies</u>
Dr. S.A. Bortz IITRI 10 W. 35th Street Chicago, IL 60616	(1)	Major W. Simmons Air Force Office of Scientific Research Building 410 Bolling Air Force Base Washington, DC 20332	(1)
Mr. G. Schmitt Air Force Materials Laboratory Wright-Patterson AFB Dayton, OH 45433	(1)	Dr. P. Becher Naval Research Laboratory Code 6362 Washington, DC 20375	(1)
Dr. D.A. Shockey Stanford Research Institute Poulter Laboratory Menlo Park, CA 94025	(1)	Mr. L.B. Weckesser Applied Physics Laboratory Johns Hopkins Road Laurel, MD 20810	(1)
Dr. W.G.D. Frederick Air Force Materials Laboratory Wright-Patterson AFB Dayton, OH 45433	(1)	Mr. D. Richardson AiResearch Manufacturing Company 4023 36th Street P.O. Box 5217 Phoenix, AZ 85010	(1)
Dr. P. Land Air Force Materials Laboratory Wright-Patterson AFB Dayton, OH 45433	(1)	Dr. H.E. Bennett Naval Weapons Center Code 3818 China Lake, CA 93555	(1)
Mr. K. Letson Redstone Arsenal Huntsville, AL 35809	(1)	Mr. G. Denman Air Force Materials Laboratory Code LPJ Wright-Patterson AFB Dayton, OH 45433	(1)
Dr. S. Freiman Naval Research Laboratory Code 6363 Washington, DC 20375	(1)	Dr. D. Godfrey Admiralty Materials Laboratory Polle, Dorset BH16 6JU UNITED KINGDOM	(1)
Director Materials Sciences Defense Advanced Research Projects Agency 1400 Wilson Boulevard Arlington, VA 22209	(1)	Dr. N. Corney Ministry of Defense The Adelphi John Adam Street London WC2N 6BB UNITED KINGDOM	(1)
Dr. James Pappis Raytheon Company Research Division 28 Seyon Street Waltham, MA 02154	(1)		

SUPPLEMENTARY DISTRIBUTION LIST (Cont'd)

<u>Organization</u>	No. of <u>Copies</u>	<u>Organization</u>	No. of <u>Copies</u>
Dr. L.M. Gillin Aeronautical Research Laboratory P.O. Box 4331 Fisherman's Bend Melbourne, VIC 3001 AUSTRALIA	(1)		
T. Paquette 5390 Cherokee Avenue Alexandria, VA 22314	(1)		